SEARCH FOR SUPERSYMMETRY IN EVENTS WITH A SINGLE LEPTON, JETS, AND MISSING TRANSVERSE MOMENTUM USING A NEURAL NETWORK

A Dissertation

Presented to the Faculty of the Graduate School

of Cornell University

in Partial Fulfillment of the Requirements for the Degree of

Doctor of Philosophy

by

Avishek Chatterjee

January 2013

SEARCH FOR SUPERSYMMETRY IN EVENTS WITH A SINGLE LEPTON, JETS, AND MISSING TRANSVERSE MOMENTUM USING A NEURAL NETWORK

Avishek Chatterjee, Ph.D.

Cornell University 2013

A search for supersymmetry in proton-proton collisions at $\sqrt{s} = 7$ TeV is presented, focusing on events with a single isolated lepton, energetic jets, and large missing transverse momentum. The analyzed data corresponds to a total integrated luminosity of 4.98 fb^{-1} recorded by the CMS experiment. The search uses an artificial neural network to suppress Standard Model backgrounds, and estimates residual backgrounds using a fully data-driven method. The analysis is performed in both the muon and electron channels, and the combined result is interpreted in terms of limits on the CMSSM parameter space, as well as a simplified model.

BIOGRAPHICAL SKETCH

Avishek Chatterjee was born on May 1, 1984 in Calcutta, India. He graduated as valedictorian from Don Bosco School (Park Circus) in 2002. Having decided to broaden his horizons by obtaining higher education abroad, Avishek moved to Middletown, CT to attend Wesleyan University for undergraduate education. A keen interest in the sciences led him to pursue a triple major in Physics, Astronomy, and Mathematics. He graduated in 2006, successfully completing all his majors, with honors in Physics, and the highest graduating GPA for a student majoring in Natural Sciences & Mathematics. Owing to a strong desire to pursue cutting-edge Physics research, graduate school was a natural transition. Avishek moved to Cornell University right after Wesleyan, drawn by Cornell's vaunted reputation in high energy physics.

While the first year of graduate school was consumed by doing coursework and with teaching responsibilities, the second year saw Avishek join the Cornell CMS group and immerse himself into particle physics research. CMS is one of two main experiments at the Large Hadron Collider, located at CERN (the world's largest particle physics laboratory) on the French-Swiss border. Avishek spent the summer of 2007 at CERN helping assemble of one of the key components of the CMS detector. His first research project was to develop a special software-based electron trigger, which served as a backup for the primary electron trigger. Avishek relocated to CERN in August 2008, making it easier to collaborate with colleagues from other institutions, attend key meetings in person, and take detector shifts. The bulk of Avishek's graduate research involved the search for supersymmetry, one of the proposed theories for physics beyond the Standard Model of particle physics.

In January 2012, Avishek returned to Cornell to work on his thesis, and start the job search. After finishing his Ph.D., Avishek will be staying at Cornell to do a post-doctoral research in accelerator physics as a part of the CESR-TA collaboration.

To my parents: without you, I would not be here.

ACKNOWLEDGEMENTS

No man is an island, certainly not someone who works in a collaborative environment like high energy physics. If I do not mention someone important, it is due to a lapse in my memory, rather than my lack of appreciation for their help.

I would like to begin by thanking my advisor, Ritchie Patterson, with whom I have enjoyed a productive, cordial, and enjoyable working relationship for over five years. My aptitude as a researcher, and as a writer of scientific documentation, has improved steadily over the years owing to her constant support and attention. I would like to thank my colleagues at Cornell: the graduate students (Darren, Don, Jennifer, Aleko, Ben, Nic, Stephen, Yao), post-docs and research associates (Lorenzo, Josh, Luke, Emmanuele, Werner), and faculty (Jim, Peter, Julia, Anders, Lawrence). The collegial atmosphere made it easy for me to ask for help without fear of feeling foolish.

This research would not have been possible without the LHC: I have great admiration for the people responsible for its design and construction. CMS is a rather young experiment, and yet the data collected by it is well-understood and modeled: my regards to the numerous subsytem experts whose tireless efforts have made this possible. The software and computing resources employed in CMS are complex and powerful: I thank the people who keep these resources functional, and provide the necessary documentation.

I would like to thank Robert Schöfbeck for helping me access and use his ntuples for data and MC samples; Paul Geffert, whose guidance with software tools was invaluable while setting exclusion limits; Niki Saolidou, for explaining some of the intricacies associated with using an artificial neural network; Ben Hooberman, for his insight into how to handle signal contamination; the sub-group within RA4 responsible for trigger and efficiency studies, and for reviewing and updating the physics object definitions as needed; and Darren Puigh, for providing ideas about how to structure this thesis.

I am grateful to the committee that reviewed the analysis on which this thesis is based: Jorgen D'Hondt, Slava Krutelyov, Michael Hildreth, Michael Schmitt, and Liliana Teodorescu. Their thorough scrutiny and detailed feedback ensured the scientific rigor of the results presented here. I am thankful to the convenors of the CMS SUSY group: David Stuart, Eva Halkiadakis, Filip Moortgat, Didar Dobur, and Ben Hooberman. Their help was invaluable in pushing this analysis through the long and arduous CMS approval process. I do not know how they are able to stay on top of the large number of SUSY analyses that CMS is involved in.

A happy worker is a productive worker, so I would like to thank all those who enriched my social life, both at CERN and in Ithaca. Finally, I would like to thank the National Science Foundation for providing the funding that allowed me to be hired as a graduate research assistant, and not have to undertake any further teaching responsibilities, which would have undoubtedly hindered my research.

TABLE OF CONTENTS

LIST OF TABLES

LIST OF FIGURES

CHAPTER 1

INTRODUCTION

There are many questions that have always been a part of human consciousness. Arguably, the most fundamental queries, at least from a physicist's point of view, relate to the nature and origin of the universe. There are two main modern scientific approaches to attempting to answer these questions: through astrophysics, which is primarily observational, and through particle physics, which relies heavily on high energy experiments. Due to the finite speed of light, seeing distant astronomical objects means that you are looking back in time: the more distant an object, the more distant past you are probing. However, the universe was opaque for the first 380,000 years of its existence. Prior to this, it was too hot for atoms to have a chance to form, and space was a plasma of electrons, photons, and baryons. When the universe expanded and cooled to around 3000 K, atoms formed, and photons were free to travel through space. These photons are the cosmic microwave background radiation that we see today.

To know what happened at earlier times, experiments are needed, and this is where particle physics comes in: by exploring higher energies, we are looking further back into the history of the universe. Based on Einstein's principle of mass-energy equivalence, the more energy that we have available, the more massive particles we can create. Nature provides us with high energy particles in the form of cosmic rays, but for more reliable studies, a controlled environment is needed, and in particle physics, this is accomplished by building particle accelerators. The idea is to accelerate particles to the highest possible energies that are technologically achievable at any point in time, collide them in narrow beams, and study what emerges from the collision.

It is instructive to look at the history of particle physics [1] to trace how this field has deepened our understanding of the universe, and get a sense of the questions that remain

unanswered. The discovery of the electron from cathode rays in 1897 by J.J. Thompson can be thought of as the birth of particle physics. He correctly surmised that the electron was an essential part of the atom. However, the Bohr model of the atom (1914), i.e. a tiny, positively charged, massive nucleus with orbiting electrons, did not emerge till Rutherford's scattering experiment (1909). Rutherford coined the term proton to refer to the hydrogen nucleus. The existence of neutral particles in the nucleus was postulated after the discovery that the mass of a nucleus was typically larger than its charge would suggest. This was confirmed by the discovery of the neutron by Chadwick in 1932, culminating the classical era of particle physics.

The idea of light being quantized was put forth by Planck in 1900 to explain the blackbody spectrum. Einstein (1905), to explain the photoelectric effect, postulated that this quantization was a feature of the electromagnetic field. There was strong resistance to Einstein's idea, motivated by the desire to avoid a corpuscular theory of light (proposed by Newton, and repudiated by the 19th century wave theory of light). Millikan's study of the photoelectric effect strongly favored Einstein's theory, and Compton scattering experiments (1923) left no room for doubt. The term *photon* was coined by Gilbert Lewis in 1926. Classically, we say that non-contact forces are mediated by a field, whereas the modern formulation is that the force arises from the exchange of particles which are quanta of the field. So when describing what holds an atom together, Coulomb's law is an excellent approximation, but the accurate description is related to the exchange of photons between the electrons and the protons in the nucleus.

Classical particle physics does not explain what keeps the nucleus together. The idea of the *strong force*, a force stronger than electromagnetism, but only valid at short (~ 1 fm) distances, was put forth to explain this, and Yukawa (1934) was the first to propose a significant theory for it. The short range of the force suggested that the mediator would

be rather heavy (intermediate to the electron and proton masses), and it was thus called a *meson* ("middle-weight"). In the same vein, electrons are *leptons* ("light-weight"), and protons and neutrons are *baryons* ("heavy-weight"). Oppenheimer drew the connection between these mesons and cosmic ray particles observed in 1937. However, more detailed studies of cosmic ray particles showed they had the wrong lifetime, were too light, resulted in inconsistent mass measurements, and interacted very weakly with nuclei. The puzzle was solved by Powell and his collaborators in 1947, when they realized that cosmic ray particles are of two types: pions (which mostly disintegrate in the upper atmosphere) and muons (which are more likely to make it to the earth's surface), and only the pion was a real meson.

The Dirac equation (relativistic quantum mechanics) requires that for every particle, there must be a corresponding antiparticle, with the same mass but the opposite electric charge. The positron (antielectron) was discovered by Anderson (1930). The antiproton and antineutron were discovered at the Berkeley Bevatron in 1955 and 1956, respectively. The Bevatron accelerated protons into a fixed target, and was named for its ability to impart energies of billions of eV. The photon is its own antiparticle. However, the matter-antimatter symmetry suggested by relativistic quantum mechanics is not observed in the universe, since the observable universe is made of ordinary matter, leading to one of the greatest unanswered questions of particle physics.

The idea of the neutrino originated from nuclear beta decay: the energy of the outgoing electron was not fixed by the masses of the parent and daughter nuclei, and this suggested the existence of a new neutral particle (postulated by Pauli, and named neutrino by Fermi). Pion and muon decays strengthened this idea. Discovering neutrinos was very challenging, since they were neutral, and barely interacted with matter: it was achieved in the mid-1950s by Cowan and Reines through an inverse beta decay

reaction. The idea of different types of neutrinos (i.e. electron neutrinos and muon neutrinos) came about when people observed lepton family number conservation. This two neutrino hypothesis was experimentally verified at Brookhaven (1962).

In 1947, Rochester and Butler published cloud chamber photographs of cosmic rays striking a lead plate and creating a new particle that decayed into two pions. This made it clear that pions were not the only mesons. This new meson was called a kaon, and soon the meson family included other new particles (η, ϕ, ω, ρ, etc). This was followed by the discovery of a new baryon (1950) called Λ. This raised the question about why the proton was stable, and the concept of baryon number conservation had to be introduced, which made it impossible for the proton to decay, since it was the lightest baryon. Many more baryons were soon discovered (Σ, Ψ, Δ, etc). Since these new mesons and baryons were unexpected, they were called *strange* particles. When the first modern accelerator began operating in 1952 (Brookhaven Cosmotron), strange particles could be made (i.e. one no longer had to rely on cosmic rays), and their numbers swelled.

One other "strange" thing about strange particles is that they are produced on a timescale of 10^{-23} s, whereas they decay on a timescale of 10^{-10} s. This suggested that the mechanisms for production and decay were different (we now know that the strong force is involved in production, and the weak force in decay). Pais suggested that strange particles must be produced in pairs, and Gell-Mann and Nishijima (1953) found a successful way to implement this. They introduced the concept of *strangeness*, a property that was conserved during production, but not during decay. The multitude of strongly interacting particles (hadrons) was split into two big families (mesons and baryons), and each member had a unique charge, strangeness and mass. But there was no underlying theory that tied everything together. Gell-Mann tried to rectify this by postulating the *The Eightfold Way*, which arranged hadrons into weird geometric patterns. Not only was

this able to provide organizational structure, but it also correctly predicted the existence of the Ω^- baryon.

An understanding of the Eightfold Way came in the form of the quark model (1964), which said that hadrons were composed of three fundamental quarks: up, down, and strange. While this model was very successful at explaining experimental observations, it did not explain why individual quarks had not been observed, even though it should be easy to do so. The interior of the proton was explored through deep inelastic scattering experiments at Stanford Linear Accelerator Center (SLAC, late 1960s) and CERN (early 1970s), and the results were reminiscent of Rutherford's scattering experiment: the proton contained three charged lumps. This was strong support for the quark model, but inconclusive. Moreover, the quark model seemed to violate the Pauli exclusion principle, and the idea of quarks having a color charge had to be introduced to address this. While this seems like a trick, it was a powerful idea and explained quark confinement by postulating that all observed particles must be colorless (this also explains why you cannot have hadrons with two or four quarks).

Between 1964 and 1974, particle physics was a barren field, and the quark theory languished. The salvation of the quark model came in the form of the J/ψ meson, which was three times as heavy as the proton, and lived about 1000 times longer than its weight would suggest. There were many proposed explanations, but the winner was that the J/ψ was composed of a new quark, called the charm. This suggested the existence of new mesons and baryons that contained the charm quark, and it was important to create one with bare charm to confirm this hypothesis: this was done in 1975. The tau lepton was also discovered in 1975, and had its own neutrino. This meant that there were six leptons, but only four quarks. However, two years later, the discovery of the Υ meson pointed the way to the fifth quark (bottom). The first bare bottom mesons were found

in 1983. The sixth quark was extremely difficult to find, since it turned out to be very massive. This was accomplished by the Tevatron collider (the first collider to be able to accelerate particles to TeV scale energies) in 1995. There are no mesons or baryons containing the top quark, since it is too short-lived to form bound states.

The electroweak theory of Glashow, Weinberg, and Salam tied together the electromagnetic and weak forces, and introduced intermediate vector bosons (W and Z) which were the force carriers. In 1983, both of these were discovered at CERN (UA1 and UA2 experiments). Unlike the strange particles, the intermediate vector bosons were predicted and long anticipated, so their discovery was a relief, rather than a shock.

Gluons, which mediate the strong force, carry color charge and should not exist as isolated particles. However, there is strong indirect evidence for them from deep inelastic scattering experiments. Results show that about half of the proton's momentum belongs to neutral constituents (presumably the gluon), and the structure of jets from high energy scattering can be attributed to the disintegration of quarks and gluons in flight.

The observations at particle colliders over the past several decades have been described by the modern theory of particle physics, called the Standard Model. The Standard Model, which is the composite of quantum chromodynamics (theory of strong interactions) and the electroweak theory, describes the fundamental constituents of matter, and their interactions with each other. It has withstood intense experimental scrutiny, but due to several shortcomings, it is now thought of as a low energy limit of a more fundamental theory. There are many possibilities for such a theory, such as Supersymmetry, Extra Dimensions, and Hidden Valleys. As we build more energetic colliders, we are able to rule out many theoretical possibilities on our path to understanding the nature of new physics. For particle physics, this is an age of exploration, and no one knows what

form new physics will take.

To explore these exciting possibilities, the colliders needed are very expensive, and pose significant technological challenges. While the Tevatron (started in 1983) was a step in this direction, the successor to the Tevatron, called the Superconducting Supercollider (SSC) was shut down due to funding issues. Experiments like BaBar (SLAC) and Belle (KEK) measured CP violation (by studying the decay rates of B mesons and their antiparticles) with high precision. This put great constraints on what forms new physics can take, since the observed CP violations were consistent with the Standard Model predictions. However, what was needed was the ability to create new fundamental particles predicted by theories beyond the Standard Model (BSM). Though the Tevatron was an impressive feat of engineering, it did not expand the physics reach enough to see glimpses of these particles. It was not until the advent of the Large Hadron Collider (LHC), commissioned in 2008, that particle physics got the boost it needed.

The primary motivation of the LHC is to understand the nature of electroweak symmetry breaking, for which the Higgs mechanism is the favored theory. The discovery of a new boson that is consistent with the Standard Model Higgs is the greatest achievement of the LHC to date. Studying the Higgs mechanism also helps test the validity of the Standard Model at the TeV scale. Alternatives to the Standard Model invoke new forces, symmetries and constituents, some of which are expected to appear at the TeV scale. Hence this energy frontier is an exciting one, and makes a compelling case for the existence of the LHC. A wide range of physics is potentially possible with the sevenfold increase in energy and a hundred-fold increase in integrated luminosity over the Tevatron.

In this dissertation, we present a search for BSM physics in the context of the theory of Supersymmetry. Physics processes other than Supersymmetry might be responsible

for any possible new physics signal observed by us, but the interpretation presented here is restricted to Supersymmetry. Chapter 2 provides a review of the Standard Model, explains why it is not a sufficient description of nature, and gives an overview of Supersymmetry. Chapter 3 describes the LHC, the machine that produces the proton-proton collisions that form of the basis of this analysis, and the Compact Muon Solenoid, the detector that records those collisions. Chapter 4 describes how the measurements made by the detector are used to reconstruct final state particles that are used in this search. Chapter 5 describes the data we use for our search, the Standard Model processes that form our background, and the tools used to simulate them. Chapter 6 details the search procedure, chapter 7 presents the results of the search, and we conclude in chapter 8.

CHAPTER 2

THE STANDARD MODEL AND BEYOND

This chapter begins with a discussion of the Standard Model (SM) of particle physics, a theory that describes electromagnetic, weak, and strong interactions of the known subatomic particles. We present a brief theoretical overview, followed by a summary of its successes in explaining the bulk of the results of experimental particle physics, and then looking at the ways in which it falls short as a complete theory. Then, we present the theory of supersymmetry (SUSY), one of the several postulated theories that might lie behind the SM, the search for which is the basis of this analysis. We look at the Minimal Supersymmetric Standard Model (MSSM), one of the best studied BSM theories, and finally the constrained MSSM (CMSSM), a formulation of MSSM with only 5 free parameters that we use in interpreting our search results.

2.1 The Standard Model

The SM incorporates the fundamental forces except gravity in a way that is able to describe the majority of particle interactions. The experimentally confirmed elementary particles that constitute the SM can be seen in Fig. 2.1. These fall into two categories: particles that constitute matter (quarks and leptons), and particles that serve as force carriers (gauge bosons). Additionally, the SM includes the Higgs boson, which plays a unique role by explaining why the other elementary particles, except the photon and gluon, are massive. It is consistent with the new boson discovered by the LHC [2, 3]. Figure 2.2 summarizes the particles interactions that are described by the SM. The discussion presented here can be found in greater detail elsewhere [4, 5].

In the SM, there are 12 elementary matter particles. They have spin = 1/2, and are

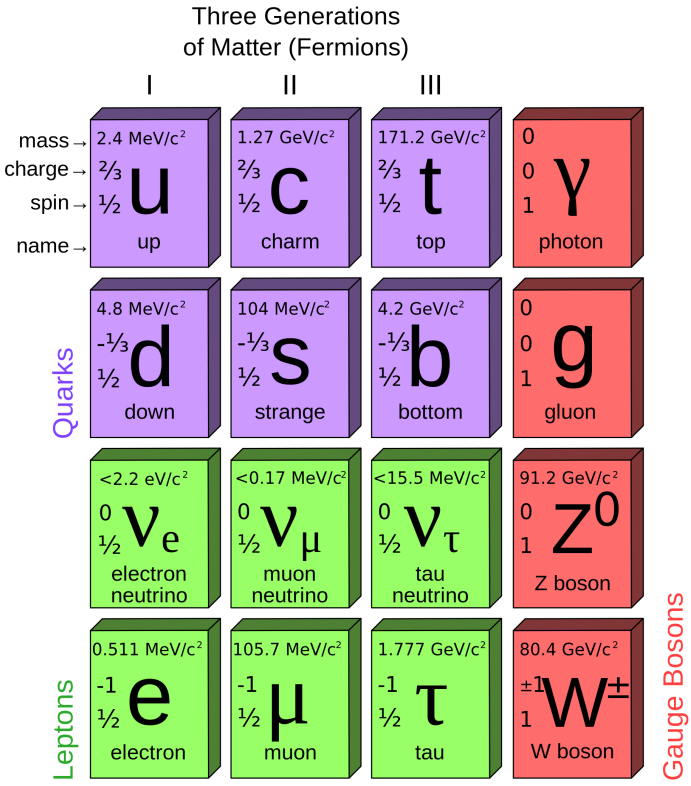

Figure 2.1: Experimentally confirmed elementary particles of the SM [6].

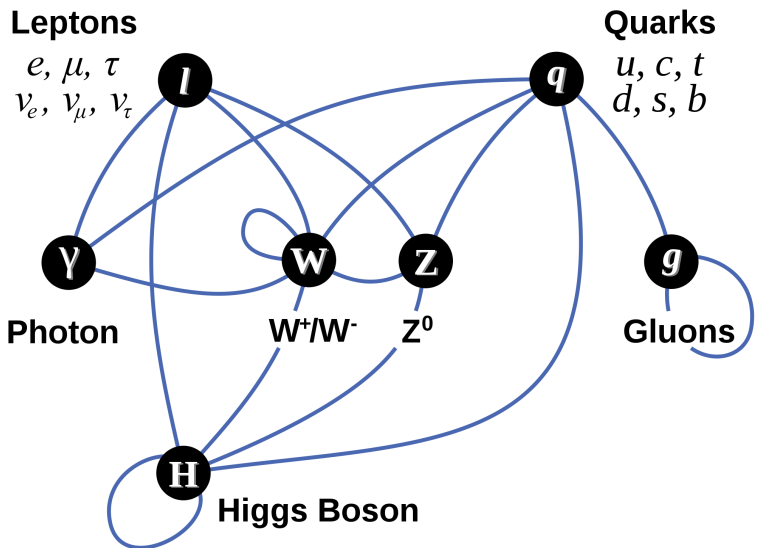

Figure 2.2: Summary of interactions between particles described by the SM [7].

called fermions, since they obey Fermi-Dirac statistics. Each of these particles has an antiparticle. These particles come in two different categories: quarks and leptons. The distinction is based on how they interact (or equivalently, by what charges they carry). There are six quarks: up, down, charm, strange, top, and bottom. These are denoted as u, d, c, s, t and b, respectively. There are six leptons: electron, electron neutrino, muon, muon neutrino, tau, and tau neutrino. These are denoted as $e, \nu_e, \mu, \nu_\mu, \tau$ and ν_τ, respectively. The charged leptons are e, μ and τ. Neutrinos do not have electric charge, and only interact via the weak force. There is one neutrino associated with each charged lepton.

Pairs from both quarks and leptons are grouped together to form a generation, with paired particles exhibiting similar physical behavior. Although we do not know why there are exactly three generations, we do know that the number of quark and lepton generations must be the same to cancel anomalies in the SM. Each member of a generation has greater mass than the corresponding particles of lower generations. The first generation charged particles do not decay, hence all ordinary (baryonic) matter is made of such particles. For example, electrons are stable, and the value of their electric charge is the fundamental unit of electric charge. Muons and taus are essentially heavy electrons, and decay via electroweak interactions.

The major difference between leptons and quarks is that quarks can interact via the strong force while leptons cannot. This is because quarks carry color charge (red, green, blue), whereas leptons do not. Although quarks are colored, we do not observe free colored objects. Quarks form bound states called hadrons that are color neutral. The bound states can be made of quark-antiquark pairs ($q_i\bar{q}_j$) or three quarks ($q_iq_jq_k$). The former are bosons called mesons, while the latter are fermions called baryons. Most hadrons are unstable and decay very quickly. One notable exception is the proton, comprised of

two up quarks and one down quark, which has a mean life larger than 10^{31} years.

In the SM, physical forces are due to the production and exchange of gauge bosons, which are spin-1 particles. The carrier of the electromagnetic interaction is the photon (γ), which is massless. Similar to gravity, electromagnetism is a long-range interaction. Photons are well-described by the theory of quantum electrodynamics (QED). The carriers of the weak interaction are the $W^{\pm}$ and Z bosons, which are both massive ($\sim$ 100 GeV). Therefore, it is a short range interaction. We also observe that the $W^{\pm}$ bosons only interact with left-chiral fermions. For this reason, the weak interaction violates parity symmetry maximally, and it also violates CP symmetry (the product of charge conjugation and parity). For the strong interaction, the carrier is the gluon (g). Although the gluon is massless, it carries color charge. There are eight gluons, labeled by a combination of color and anticolor charge. Since the gluon is colored, the strong interaction is confining, and thus a short-range interaction. Since gluons have an effective color charge, they can also self-interact. Gluons and their interactions are described by the theory of quantum chromodynamics (QCD).

Finally, the SM includes the Higgs boson. It is a massive spin-0 scalar, and explains why the other elementary particles, except the photon and gluon, are massive. The SM requires all the carriers of the electroweak force to have zero mass, in order to allow the unification of the electromagnetic and weak forces into the electroweak force. However, unlike the photon, the W and Z bosons are massive. The electroweak symmetry of boson masses is thus broken (this is referred to as EWSB). One way to induce EWSB is to add an extra Higgs field to the SM, the particle excitation of which is the Higgs boson.

2.1.1 Formulation of the Standard Model

The SM is a quantum field theory (QFT) in 4-D Minkowski space. Each SM particle is described in terms of a dynamical field ($\phi(x)$) that pervades space-time. Dynamics are described via a Lagrangian density ($\mathcal{L}$), usually just referred to as the Lagrangian, the space-time integral of which gives the action ($\mathcal{S}$). Requiring that $\delta\mathcal{S} = 0$ while each field ϕ is varied yields the equations of motion:

$$\partial_\mu \left(\frac{\partial \mathcal{L}}{\partial(\partial_\mu \phi)} \right) = \frac{\partial \mathcal{L}}{\partial \phi}. \tag{2.1}$$

The construction of the SM Lagrangian starts by postulating a set of symmetries of the system, and then by writing down the most general renormalizable Lagrangian[1] from its particle (field) content that observes these symmetries. Since the SM is a relativistic QFT, a global Poincaré symmetry is postulated, which includes symmetry under translation, rotation and boost. By Noether's theorem, each symmetry is associated with a conservation law, and the Poincaré symmetry leads to conservation of energy, momentum, and angular momentum. The defining feature of the SM is the local internal symmetry, referred to as the gauge group:

$$SU(3)_C \otimes SU(2)_L \otimes U(1)_Y \tag{2.2}$$

where C denotes color (the charge of the strong interaction), L refers to left-handed fields (to indicate the parity-violating nature of the weak interaction), and Y denotes hypercharge. The gauge group determines the SM forces. For example, the $SU(3)_C$ group corresponds to the strong force. The conserved quantities that come from the gauge group are color charge, weak isospin, electric charge, and weak hypercharge.

SM particles have different representations under the gauge group. There are three

[1] meaning coefficients of the interaction terms in the Lagrangian cannot have dimension of mass to a negative power

generations (or flavors) of fermions, and each generation consists of five representations:

$$L_L^i(1,2)_{-1/2}, \quad E_R^i(1,1)_{-1}, \quad Q_L^i(3,2)_{1/6}, \quad U_R^i(3,1)_{2/3}, \quad D_R^i(3,1)_{-1/3} \tag{2.3}$$

where the first and second numbers in parentheses indicates the $SU(3)_C$ and $SU(2)_L$ representation of the field, respectively. The first subscript indicates whether it is a left- or right-handed fermion, and the second index is the $U(1)_Y$ hypercharge. The i superscript is the flavor index indicating the generation, with $i = 1, 2, 3$.

There is one vector field for each generator of the SM gauge group. The $SU(3)_C$ group has eight generators (Gell-Mann matrices), and thus eight vector fields, the gluon fields (G_μ). The $SU(2)_L$ group has three generators (Pauli matrices), and thus three vector fields, the isospin gauge fields (W_μ^1, W_μ^2, and W_μ^3). The $U(1)_Y$ group has only one generator, and hence one vector field, the hypercharge gauge field (B_μ). The SM also contains a scalar field, $\phi(1,2)_{1/2}$ responsible for SSB of the electroweak interaction

$$SU(2)_L \otimes U(1)_Y \xrightarrow{SSB} U(1)_{\mathrm{EM}} \tag{2.4}$$

into the electromagnetic interaction. The Higgs boson is the particle excitation of this hypothetical field.

The SM Lagrangian consists of two parts: one that deals with the strong interaction ($\mathcal{L}_{\mathrm{QCD}}$), and one that deals with the electroweak interaction ($\mathcal{L}_{\mathrm{EWK}}$). The QCD Lagrangian is given by:

$$\mathcal{L}_{\mathrm{QCD}} = i\bar{\psi}_i\gamma^\mu\partial_\mu\psi_i - g_s G_\mu^a \bar{\psi}_i \gamma^\mu T_{ij}^a \psi_j - \frac{1}{4} G_{\mu\nu}^a G_a^{\mu\nu}. \tag{2.5}$$

where ψ_i are the quark fields, γ^μ are the Dirac matrices, g_s is the gauge coupling of the $SU(3)_C$ group, T_{ij}^a are the Gell-Mann matrices, and $G_{\mu\nu}^a$ is defined as:

$$G_{\mu\nu}^a = \partial_\mu G_\nu^a - \partial_\nu G_\mu^a - g_s f^{abc} G_\mu^b G_\nu^c \tag{2.6}$$

where f^{abc} are the structure constants of $SU(3)_C$.

QCD has two special properties: (i) confinement, which means that the force between quarks does not diminish as they are separated, verified experimentally by the fact that free quarks do not exist, and (ii) asymptotic freedom, which means that in very high-energy reactions, quarks and gluons interact very weakly. QCD calculations are extremely complicated, and approximations have to be used. There are two common ways this is done: (i) perturbative QCD, an approach based on asymptotic freedom, which allows perturbation theory to be used accurately in experiments performed at very high energies, and (ii) lattice QCD, the best established non-perturbative approach, which uses a discrete set of space-time points (called the lattice) to reduce the analytically unsolvable path integrals of the continuum theory to a very difficult numerical computation which is then carried out on supercomputers.

Before looking at the electroweak Lagrangian, it is useful to define the covariant derivative:

$$D_\mu = \partial_\mu - igW_\mu^a \tau_a - ig' B_\mu Y \tag{2.7}$$

where the constants g and g' are the gauge couplings of the $SU(2)_L$ and $U(1)_Y$ groups, respectively; $\tau_a = \frac{\sigma_a}{2}$, where σ_a are the Pauli matrices; Y is the generator of $U(1)_Y$, i.e. any complex number with absolute value of 1. The electroweak Lagrangian prior to SSB is given by:

$$\mathcal{L}_{\text{EWK}} = \mathcal{L}_{\text{Gauge}} + \mathcal{L}_{\text{Fermion}} + \mathcal{L}_{\text{Higgs}} + \mathcal{L}_{\text{Yukawa}}. \tag{2.8}$$

The first term, $\mathcal{L}_{\text{Gauge}}$, describes the interactions between the gauge bosons:

$$\mathcal{L}_{\text{Gauge}} = -\frac{1}{4} W_{\mu\nu}^a W_a^{\mu\nu} - \frac{1}{4} B_{\mu\nu} B^{\mu\nu} \tag{2.9}$$

where the field strength tensors are given by

$$W_{\mu\nu}^a = \partial_\mu W_\nu^a - \partial_\nu W_\mu^a + g\epsilon^{abc} W_\mu^b W_\nu^c \quad , \quad B_{\mu\nu} = \partial_\mu B_\nu - \partial_\nu B_\mu. \tag{2.10}$$

The second term in eq. 2.8 is the kinetic term for fermions:

$$\mathcal{L}_{\text{Fermion}} = \sum_k i\bar{\psi}_k \gamma^\mu D_\mu \psi_k \tag{2.11}$$

where the sum runs over the 5 fermion fields given in eq. 2.3. The third term in eq. 2.8 describes the Higgs field:

$$\mathcal{L}_{\text{Higgs}} = \left|D_\mu \phi\right|^2 - \lambda\left(|\phi|^2 - \frac{\upsilon^2}{2}\right)^2 \tag{2.12}$$

where λ is the Higgs self-coupling strength, and $\upsilon^2 > 0$. Finally, the fourth term in eq. 2.8 gives the Yukawa interaction between the Higgs field and the fermion fields:

$$\mathcal{L}_{\text{Yukawa}} = -y^e_{ij}\bar{L}^i_L E^j_R \phi - y^d_{ij}\bar{Q}^i_L D^j_R \phi - \epsilon_{\text{ab}} y^u_{ij}\bar{Q}^{i\text{a}}_L U^j_R \phi^{\dagger\text{b}} + h.c. \tag{2.13}$$

where the constants y_{ij} are the strength of coupling between the Higgs and fermion fields. The Yukawa terms generate the fermion masses after the Higgs acquires a vacuum expectation value (VEV, denoted by υ) through SSB. The electroweak Lagrangian after SSB is given by:

$$\mathcal{L}_{\text{EWK}} = \mathcal{L}_K + \mathcal{L}_N + \mathcal{L}_C + \mathcal{L}_H + \mathcal{L}_{HV} + \mathcal{L}_{WWV} + \mathcal{L}_{WWVV} + \mathcal{L}_Y. \tag{2.14}$$

$\mathcal{L}_K$ is the kinetic term, and consists of all the quadratic terms of the Lagrangian, which include the dynamic terms (the partial derivatives) and the mass terms (which only appear after SSB). $\mathcal{L}_H$ contains the Higgs three-point and four-point self interaction terms; $\mathcal{L}_{HV}$ contains the Higgs interactions with gauge vector bosons; $\mathcal{L}_{WWV}, \mathcal{L}_{WWVV}$ contain the gauge three-point and four point self interactions, respectively; $\mathcal{L}_Y$ contains the Yukawa interactions between the fermions and the Higgs field. Of greatest relevance to this analysis are $\mathcal{L}_N$ and $\mathcal{L}_C$, which contain the neutral and charged current interactions between fermions and gauge bosons. In order to understand them, we need to switch from the basis that has W^a and B as the vector fields to a basis that uses mass eigenstate vector fields. The relevant definitions are:

$$W^\pm_\mu = \frac{1}{\sqrt{2}}\left(W^1_\mu \mp iW^2_\mu\right), Z_\mu = \frac{1}{\sqrt{g^2+g'^2}}\left(gW^3_\mu - g'B_\mu\right), A_\mu = \frac{1}{\sqrt{g^2+g'^2}}\left(g'W^3_\mu + gB_\mu\right) \tag{2.15}$$

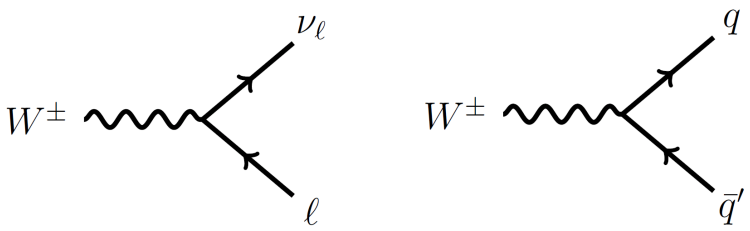

Figure 2.3: Feynman diagrams of the interaction between the W boson and fermions. Left: $W \to \ell\nu$. Right: $W \to q\bar{q}'$.

Using this new basis, and the fact that the Higgs has a VEV, eq. 2.12 can be written as:

$$\mathcal{L}_{\text{Higgs}} = \left(m_W^2 W_\mu^- W^{+\mu} + \frac{m_Z^2}{2} Z_\mu Z^\mu\right)\left(1 + \frac{h}{\upsilon}\right)^2 + \frac{1}{2}\left(\partial_\mu h\right)^2 - \frac{m_h^2}{2}h^2 - \frac{\xi}{3!}h^3 - \frac{\eta}{4!}h^4 \quad (2.16)$$

where

$$m_W^2 = \frac{1}{4}g^2\upsilon^2, m_Z^2 = \frac{1}{4}\left(g^2 + g'^2\right)\upsilon^2, m_h^2 = 2\lambda\upsilon^2, \xi = 6\lambda\upsilon = \frac{3m_h^2}{\upsilon}, \eta = 6\lambda = \frac{3m_h^2}{\upsilon^2}, \quad (2.17)$$

and h is the SM Higgs field. There is no term that looks like $m_A^2 A_\mu A^\mu$, indicating that the A_μ field remains massless ($m_A^2 = 0$). We identify the A field as the electromagnetic field with its massless photon. The gauge bosons $W^\pm$ and Z, which can be associated with the remaining three vector fields, do gain mass from SSB. The charged current interaction, which involves $W^\pm$, can be expressed as:

$$\mathcal{L}_C = \frac{g}{2\sqrt{2}}\bar{\nu}^i \gamma^\mu \left(1 - \gamma^5\right) W_\mu^+ e^i + V^{ij}\frac{g}{2\sqrt{2}}\bar{u}^i \gamma^\mu \left(1 - \gamma^5\right) W_\mu^+ d^j + h.c. \quad (2.18)$$

where V^{ij} is the CKM matrix. Figure 2.3 shows the Feynman diagrams for interactions between $W^\pm$ and the fermions. The neutral current interaction, which involves the neutral gauge bosons, can be expressed as:

$$\mathcal{L}_N = eJ_\mu^{em}A^\mu + \frac{g}{\cos\theta_W}(J_\mu^3 - \sin^2\theta_W J_\mu^{em})Z^\mu \quad (2.19)$$

where e is the electron charge, θ_W is the Weinberg angle ($\cos\theta_W = m_W/m_Z$), and the electromagnetic current J_μ^{em} and the neutral weak current J_μ^3 are given by:

$$J_\mu^{em} = \sum_f q_f \overline{f}\gamma_\mu f \quad , \quad J_\mu^3 = \sum_f I_f^3 \overline{f}\gamma_\mu \frac{1 - \gamma^5}{2} f \quad (2.20)$$

where q_f is the fermion's electric charge, and I_f^3 is its weak isospin.

The SM has four global $U(1)$ symmetries that are accidental, meaning they not an input to the theory, but an output. The consequence of this is the conservation of baryon number, electron number, muon number, and tau number. The last three are together referred to as lepton family number conservation. Conservation of baryon number implies that the number of quarks minus the number of antiquarks is a constant, and no experimental violation of this has been observed. The conservation of lepton family number can be understood analogously. The discovery that neutrinos are not massless (via neutrinos oscillating from one flavor to another) in contradiction to the SM prediction indicates that the conservation of lepton family number is violated.

The SM has 19 free parameters. The parameters are: Yukawa couplings that give the quarks and leptons mass (6 + 3 = 9 parameters), the CKM mixing angles and CP-violating phase (3 + 1 = 4 parameters), the coupling constants of the gauge sector (3 parameters), the constants of the Higgs sector (2 parameters), and a parameter related to the vacuum structure of the strong interaction (1 parameter). These parameters are inputs to the SM theory, and have been determined experimentally.

2.1.2 Triumphs of the Standard Model

The hallmark of a successful theory is its predictive power: the SM correctly predicted the existence of the W and Z bosons, the gluon, the top and charm quarks. The new boson recently discovered by the LHC is consistent with the Higgs boson predicted by the SM. The foremost experiment to test the SM by making precision electroweak measurements was the Large Electron-Positron Collider (LEP). Numerous measurements of decay widths and branching fractions made at the Z boson pole confirm the predic-

tions of the SM. The LEP Electroweak Working Group (LEP EWWG) combines the measurements of the four LEP experiments (ALEPH, DELPHI, L3 and OPAL) on electroweak observables, such as cross sections, masses and various couplings of the heavy electroweak gauge bosons, properly taking into account the common systematic uncertainties. These combinations are compared with theory predictions. The conclusion is that the SM is able to describe nearly all the LEP measurements successfully, and there is no compelling need for introducing new physics. Exploiting theory relationships, the experimental results are used to predict the masses of heavy fundamental particles, such as the top quark and the W boson, which are then compared to the direct measurements. This checks the correctness of the prediction, and thus of the theory, in this area. The LEP EWWG also uses all measurements of the SM simultaneously to overconstrain the SM. This way, one can compare each measured observable to the best-fit prediction. This is demonstrated in Fig. 2.4. Agreement is often at the 0.1% level, and sometimes even better.

2.1.3 Limitations of the Standard Model

Despite the great success of the SM in explaining a wide array of experimental results, we know that it cannot be the ultimate description of the universe. Firstly, it only describes three of the four known forces, and gravity remains unaccounted for; the SM is thus not a theory of everything. The SM can be considered to be ad-hoc and inelegant, since the values of its 19 numerical constants are mostly unrelated and arbitrary. There is no explanation as to why there should be three generations of particles.

The most well-known theoretical objection to the SM is the hierarchy problem, which can be stated as: why is the weak force so much stronger than gravity? The

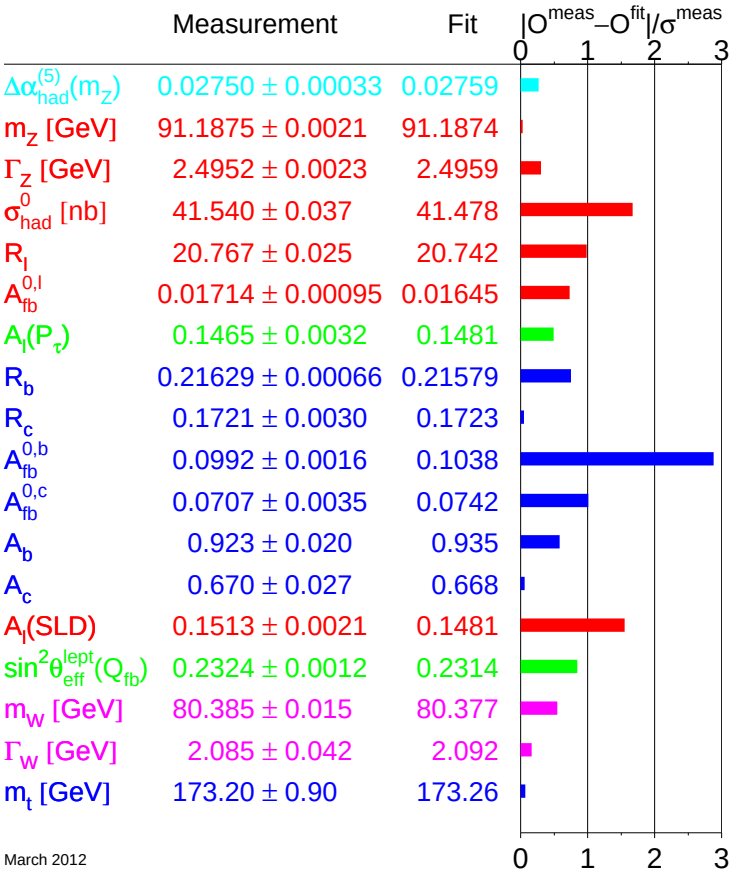

Figure 2.4: Comparison of the values of SM parameters, as obtained from direct measurements, and from an overconstrained fit [8].

weak force depends on Fermi's constant ($G_F = 1/(\sqrt{2}v^2) \sim 10^{-5}$ GeV^{-2}), and gravity depends on Newton's constant ($\sim 10^{-38}$ GeV^{-2}). Quantum corrections to Fermi's constant calculated using the SM would make it closer to Newton's constant, and the only way around this is if there is a delicate cancellation between the bare value of Fermi's constant and the quantum corrections to it, referred to as fine-tuning, an unpleasant feature of any theory. Another way to think about the hierarchy problem is via the Higgs

mass (m_H). The Higgs mass receives large quantum corrections that are related to the scale up to which the SM holds. The two common scales at which the SM is expected to break down are the Planck scale and the grand unification theory (GUT) scale. The Planck scale (10^{19} GeV) is the scale at which the quantum effects of gravity are expected to be large. The GUT scale is the scale at which the electromagnetic, weak, and strong forces can be described as a unified force. This depends on the nature of the GUT, but it is typically about 10^{16} GeV. In the absence of new physics between one of these scales and the electroweak scale (100 GeV), the corrections to the Higgs mass are many orders of magnitude larger than its actual mass. In order to keep the Higgs mass at the electroweak scale, the bare mass of the Higgs has to be fine-tuned.

Additionally, there are several experimental observations which the SM cannot account for. From several neutrino experiments, we know that neutrinos can oscillate from one flavor to another. This can only be explained if neutrinos have non-zero mass, inconsistent with the current SM formulation. From cosmological measurements, we know that ordinary baryonic matter can only account for about 4% of the energy density of the universe, the rest coming from dark matter (about 23%) and dark energy (about 73%). The existence of dark matter is inferred solely through its gravitational interactions with other matter. It is incapable of electromagnetic interactions, and therefore not observable through telescopes (hence *dark*). There is no particle in the SM that is a viable dark matter candidate. Dark energy is a hypothetical form of energy that permeates all space, and accelerates the expansion of the universe, and beyond the scope of the SM. The SM is unable to explain the matter-antimatter asymmetry of the current universe: if there were equal amounts of matter and antimatter after the Big Bang, then why is the observable universe mostly made of the matter i.e. where did the antimatter go? The SM is also unable to account for the strong CP problem, which can be stated as: why does QCD not violate the CP symmetry? In electroweak theory, gauge fields couple to

chiral currents constructed from fermionic fields, whereas gluons couple to vector currents. Experiments do not indicate any CP violation in the QCD sector, the strongest constraint coming from the dipole moment of the neutron. There are natural terms in the QCD Lagrangian that are able to break the CP symmetry, and the only way to avoid that is through fine-tuning.

The scattering amplitude of longitudinally polarized W bosons at tree level grows as s, where s is the center of mass energy squared. This growth continues until the mass of the Higgs is reached, and thereafter it stays constant at a value proportional to m_H^2. Thus, for unitarity to not be violated, there must be an upper bound on m_H^2, which implies that the Higgs should appear below the TeV scale. The discovery of the Higgs at 125 GeV eliminates this problem.

Some examples of new physics that we may see at the LHC include supersymmetry, extra dimensions, hidden valley theories, or new gauge bosons. These new physics models address one or more shortcomings of the SM, and often predict the existence of particles beyond those postulated in the SM.

2.2 Supersymmetry

SUSY is a symmetry that relates elementary particles with a certain spin to other particles that differ by half a unit of spin, these new particles being referred to as superpartners. In a theory with unbroken supersymmetry, for every boson (fermion) there exists a corresponding fermion (boson) with the same mass and internal quantum numbers. Since the superpartners of SM particles have not been observed, SUSY, if it exists, must be a broken symmetry. This would allow the superpartners to be heavier than the corresponding SM particles. While there is no direct evidence for the existence of SUSY,

it has great theoretical appeal if it exists around the TeV scale, since it can overcome several of the shortcomings of the SM: it can solve the hierarchy problem, it can unite three of the four fundamental forces at high energies, it can provide a viable dark matter candidate, and a natural mechanism for EWSB. The discussion in this section is an abridged version of what is presented elsewhere [9].

2.2.1 SUSY algebra and supermultiplets

A SUSY transformation acting on a fermionic state gives a bosonic state, and vice versa; hence, a generating operator of such a transformation must be a fermionic operator with spin 1/2, and SUSY is a spacetime symmetry. For an interacting QFT with chiral fermions, generators Q and $Q^\dagger$ of such a symmetry must satisfy the commutation and anti-commutation relations:

$$\{Q, Q^\dagger\} = P^\mu \quad , \quad \{Q, Q\} = \{Q^\dagger, Q^\dagger\} = 0 \quad , \quad [P^\mu, Q] = [P^\mu, Q^\dagger] = 0 \tag{2.21}$$

where $P^\mu = (H, \vec{P})$ is the spacetime momentum operator, H is the Hamiltonian, and $\vec{P}$ is the three-momentum operator. The commutation rules for these generators define the SUSY algebra. Irreducible representations of the algebra are called supermultiplets, with each element of the supermultiplet corresponding to a single-particle state. A supermultiplet contains superpartner fermion and boson states (which have identical gauge interactions, necessary for the cancellations in Δm_H^2 that solve the hierarchy problem), with identical numbers of fermionic and bosonic degrees of freedom. Next we construct the different possible supermultiplets.

The simplest supermultiplet contains a left-handed Weyl fermion ψ (complex two-component object) which has $n_F = 4$ off-shell degrees of freedom, and 2 on-shell degrees of freedom (going on-shell eliminates half of the propagating degrees of freedom

for ψ, because the Lagrangian is linear in time derivatives). Since the Weyl fermion is an intrinsically complex object, the superpartner should be a complex scalar field ϕ, with $n_B = 2$ degrees of freedom corresponding to the real and imaginary components of the field. For the n_B to match n_F, both on-shell and off, we introduce a non-propagating complex scalar *auxiliary field* F which has 2 off-shell degrees of freedom and 0 on-shell degrees of freedom (F does not have a kinetic term). The dimensions of F are $[\text{mass}]^2$, unlike an ordinary scalar field, which has dimensions of [mass]. This combination is called a *chiral* supermultiplet.

Next, we consider a massless spin-1 vector boson A^a_μ which has $n_B = 2$ on-shell degrees of freedom (corresponding to the two possible helicity states) and $n_B = 3$ off-shell degrees of freedom (the inhomogeneous gauge transformation equation reduces n_B from 4 to 3). The index a here runs over the adjoint representation of the gauge group ($a = 1, \ldots, 8$ for $SU(3)_C$ color gluons and gluinos; $a = 1, 2, 3$ for $SU(2)_L$ weak isospin; $a = 1$ for $U(1)_Y$ weak hypercharge). The superpartner is taken to be a Weyl fermion gaugino λ^a which has $n_F = 4$ off-shell degrees of freedom, and $n_F = 2$ on-shell degrees of freedom. To make the number of fermionic and bosonic degrees of freedom match, we must introduce a real bosonic auxiliary field D^a with one off-shell degree of freedom and 0 on-shell degrees of freedom. Like the chiral auxiliary fields F_i, the gauge auxiliary field D^a has dimensions of $[\text{mass}]^2$ and no kinetic term, so it can be eliminated on-shell using its algebraic equation of motion. This combination is called a *gauge* supermultiplet.

For the MSSM, which is the only SUSY model we are interested in, all other representations of the SUSY algebra are reducible to combinations of chiral and gauge supermultiplets. The supermultiplets of the MSSM can be seen in Table 2.1, and will be discussed in Sec. 2.2.2.1.

Table 2.1: Supermultiplets of the MSSM.

Names		spin	spin	$SU(3)_C, SU(2)_L, U(1)_Y$
Chiral supermultiplets		0	1/2	
squarks, quarks	Q	$(\tilde{u}_L\ \tilde{d}_L)$	$(u_L\ d_L)$	$(\mathbf{3}, \mathbf{2}, \frac{1}{6})$
$\times$ 3 families	$\bar{u}$	$\tilde{u}_R^*$	$u_R^\dagger$	$(\bar{\mathbf{3}}, \mathbf{1}, -\frac{2}{3})$
	$\bar{d}$	$\tilde{d}_R^*$	$d_R^\dagger$	$(\bar{\mathbf{3}}, \mathbf{1}, \frac{1}{3})$
sleptons, leptons	L	$(\tilde{\nu}\ \tilde{e}_L)$	$(\nu\ e_L)$	$(\mathbf{1}, \mathbf{2}, -\frac{1}{2})$
$\times$ 3 families	$\bar{e}$	$\tilde{e}_R^*$	$e_R^\dagger$	$(\mathbf{1}, \mathbf{1}, 1)$
Higgs, higgsinos	H_u	$(H_u^+\ H_u^0)$	$(\tilde{H}_u^+\ \tilde{H}_u^0)$	$(\mathbf{1}, \mathbf{2}, +\frac{1}{2})$
	H_d	$(H_d^+\ H_d^0)$	$(\tilde{H}_d^+\ \tilde{H}_d^0)$	$(\mathbf{1}, \mathbf{2}, -\frac{1}{2})$
Gauge supermultiplets		1/2	1	
gluino, gluon		$\tilde{g}$	g	$(\mathbf{8}, \mathbf{1}, 0)$
winos, W bosons		$\tilde{W}^\pm, \tilde{W}^0$	$W^\pm, W^0$	$(\mathbf{1}, \mathbf{3}, 0)$
bino, B boson		$\tilde{B}^0$	B^0	$(\mathbf{1}, \mathbf{1}, 0)$

2.2.2 The Minimal Supersymmetric Standard Model

It is possible to have more than one type of SUSY transformation. The more supersymmetry a theory has, the more constrained the field content and interactions are. Typically, the number of copies of SUSY is a power of 2, i.e. $N = 1, 2, 4$, or 8, where N is the number of copies of SUSY. In 4-D, a spinor has four degrees of freedom; the number of SUSY generators is therefore four. Having eight copies of SUSY implies having 32 SUSY generators, which is the maximum possible number. Theories with more than 32 SUSY generators automatically have massless fields with spin greater than 2, and it is not known how to make such fields interact. While it is mathematically interesting to have $N > 1$ (known as extended SUSY), such models do not have any phenomenological prospects, since extended SUSY in 4-D field theories cannot allow for chiral fermions or parity violation as observed in the SM. Extended SUSY in higher-dimensional field theories may be a valid description of nature if the extra dimensions are compactified. MSSM is the minimal extension to the SM that realizes $N = 1$ SUSY.

2.2.2.1 Particle content

In a supersymmetric extension of the SM, each of the known fundamental particles is in either a chiral or gauge supermultiplet, and must have a superpartner with spin differing by 1/2. Only chiral supermultiplets can contain fermions whose left-handed parts transform differently under the gauge group than their right-handed parts. All SM fermions have this property, so they must be members of chiral supermultiplets. The names for the spin-0 partners of the quarks and leptons are constructed by prepending an "s", for scalar. So, generically they are called squarks and sleptons, or sometimes sfermions. The left-handed and right-handed pieces of the quarks and leptons are separate two-component Weyl fermions with different gauge transformation properties in the SM, so each must have its own complex scalar partner. The symbols for the squarks and sleptons are the same as for the corresponding fermion, but with a tilde ($\sim$) used to denote the superpartner of a SM particle. The gauge interactions of each of these squark and slepton fields are the same as for the corresponding SM fermions.

There are two Higgs chiral supermultiplets rather than just one. There are two important reasons for this: (i) If there was only one Higgs chiral supermultiplet, the electroweak gauge symmetry would suffer a gauge anomaly. A fermionic partner of a Higgs chiral supermultiplet must be a weak isodoublet with weak hypercharge $Y = 1/2$ or $Y = -1/2$. In either case alone, such a fermion will spoil the anomaly cancellation that happens in the SM, but if both hypercharges are present, the anomaly disappears. (ii) Due to the structure of supersymmetric theories, only a $Y = 1/2$ Higgs chiral supermultiplet can have the Yukawa couplings necessary to give masses to up-type quarks, and only a $Y = -1/2$ Higgs can have the Yukawa couplings necessary to give masses to charge down-type quarks and charged leptons.

We will call the $SU(2)_L$-doublet complex scalar fields with $Y = 1/2$ and $Y = -1/2$

by the names H_u and H_d, respectively. The weak isospin components of H_u with $T_3 = (1/2, -1/2)$ have electric charges 1, 0 respectively (denoted H_u^+, H_u^0). Similarly, H_d has $T_3 = (1/2, -1/2)$ components denoted as H_d^0, H_d^-. The neutral scalar that corresponds to the SM Higgs is a linear combination of H_u^0 and H_d^0. The generic nomenclature for a spin-1/2 superpartner is to append "-ino" to the name of the SM particle, so the fermionic partners of the Higgs scalars are called higgsinos. They are denoted by $\tilde{H}_u$, $\tilde{H}_d$.

The vector bosons of the SM must reside in gauge supermultiplets. Their fermionic superpartners are generically referred to as gauginos. The gluon's spin-1/2 color-octet supersymmetric partner is the gluino ($\tilde{g}$). The electroweak gauge symmetry is associated with spin-1 gauge bosons W^+, W^0, W^- and B^0, with spin-1/2 superpartners $\tilde{W}^+$, $\tilde{W}^0$, $\tilde{W}^-$ and $\tilde{B}^0$, called winos and bino. After EWSB, the W^0, B^0 gauge eigenstates mix to give mass eigenstates Z^0 and γ. The corresponding gaugino mixtures of $\tilde{W}^0$ and $\tilde{B}^0$ are called zino ($\tilde{Z}^0$) and photino ($\tilde{\gamma}$).

The higgsinos and electroweak gauginos mix with each other because of EWSB. The neutral higgsinos and the neutral gauginos combine to form four mass eigenstates called neutralinos. The charged higgsinos and winos mix to form two mass eigenstates with charge ± 1 called charginos. We denote the neutralino and chargino mass eigenstates by $\tilde{\chi}_i^0$ (i = 1, 2, 3, 4) and $\tilde{\chi}_i^\pm$ (i = 1, 2). The convention is to enumerate the mass eigenstates in order of increasing mass.

2.2.2.2 The superpotential and supersymmetric interactions

The most general non-gauge interactions for chiral supermultiplets are determined by a single function of the complex scalar fields, the superpotential W. The interactions and masses of all particles are determined just by their gauge transformation properties and

by the superpotential. The superpotential for the MSSM is given by:

$$W_{\text{MSSM}} = \bar{u}\mathbf{y_u}QH_u - \bar{d}\mathbf{y_d}QH_d - \bar{e}\mathbf{y_e}LH_d + \mu H_u H_d \tag{2.22}$$

where H_u, H_d, Q, L, $\bar{u}$, $\bar{d}$, $\bar{e}$ are the chiral superfields corresponding to the chiral supermultiplets in Table 2.1. The dimensionless Yukawa coupling parameters $\mathbf{y_u}$, $\mathbf{y_d}$ and $\mathbf{y_e}$ are 3×3 matrices. The μ term in eq. 2.22 is the supersymmetric version of the Higgs boson mass in the SM.

The Yukawa matrices determine the masses and CKM mixing angles of the SM fermions, after the neutral scalar components of H_u and H_d get VEVs. Since the top quark, bottom quark and tau lepton are the heaviest fermions in the SM, one can make an approximation that only the (3,3) matrix element of the Yukawa matrices are non-zero (denoted as y_t, y_b and y_τ). The superpotential can then be reduced to:

$$W_{\text{MSSM}} \approx y_t(\bar{t}tH_u^0 - \bar{t}bH_u^+) - y_b(\bar{b}tH_d^- - \bar{b}bH_d^0) - y_\tau(\bar{\tau}\nu_\tau H_d^- - \bar{\tau}\tau H_d^0) + \mu(H_u^+ H_d^- - H_u^0 H_d^0) \tag{2.23}$$

In SUSY, Yukawa interactions y^{ijk} must be completely symmetric under interchange of i, j, k. Hence, $\mathbf{y_u}$, $\mathbf{y_d}$ and $\mathbf{y_e}$ imply not only Higgs-quark-quark and Higgs-lepton-lepton couplings as in the SM, but also squark-Higgsino-quark and slepton-Higgsino-lepton interactions. An example of this that involves the top quark is shown in Fig. 2.5. For each of the three interactions, there is another with H_u^0 replaced by H_u^+ and t_L replaced by $-b_L$ (with tildes where appropriate), corresponding to the second part of the first term in eq. 2.23. All of these interactions are required by SUSY to have the same strength y_t. These couplings can be modified by the introduction of soft SUSY-breaking only through small radiative corrections, so this equality of interaction strengths still holds under softly broken SUSY.

Scalar quartic interactions with strength proportional to y_t^2 also exist, and examples can be seen in Fig. 2.6. There are five more such interactions, which can be obtained

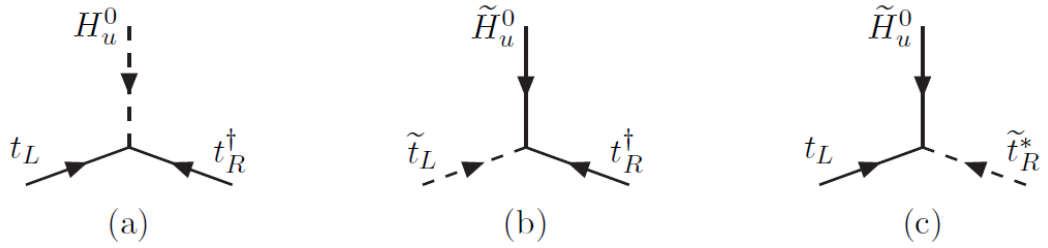

Figure 2.5: The top-quark Yukawa coupling (a) and its *supersymmetrizations* (b), (c), all of strength y_t.

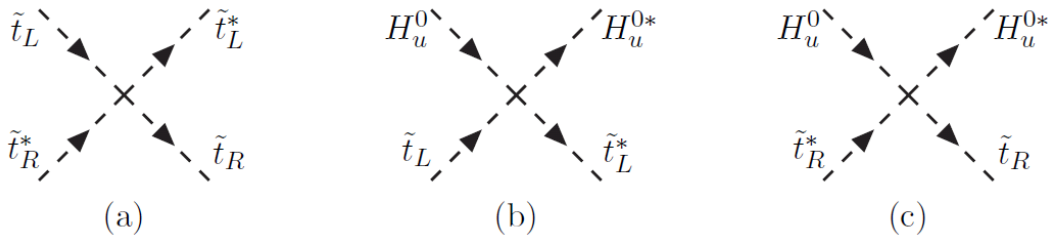

Figure 2.6: Examples of scalar quartic interactions with strength proportional to y_t^2.

by replacing $\tilde{t}_L$ by $\tilde{b}_L$ and/or H_u^0 by H_u^+ in each vertex. This illustrates the economy of SUSY, where many interactions are described by a single parameter. In general, all scalar quartic couplings [(squark)^4, (slepton)^4, (squark)^2(slepton)^2, (squark)^2(Higgs)^2 and (slepton)^2(Higgs)^2] can be obtained from elements of $\mathbf{y_u}$, $\mathbf{y_d}$ and $\mathbf{y_e}$.

However, the dimensionless interactions are not the most phenomenologically important, since the Yukawa couplings are very small (except for those of the third generation). Instead, production and decay processes for sparticles are typically dominated by the supersymmetric interactions of gauge-coupling strength. The couplings of the SM gauge bosons to the MSSM particles are determined completely by the gauge invariance of the kinetic terms in the Lagrangian. The gauginos couple to (squark, quark) and (slepton, lepton) and (Higgs, higgsino) pairs. These types of interactions can be seen in Fig. 2.7. For each of these diagrams, there is another with all arrows reversed. Note that the winos only couple to the left-handed squarks and sleptons, and the (lepton, slepton) and (Higgs, higgsino) pairs of course do not couple to the gluino.

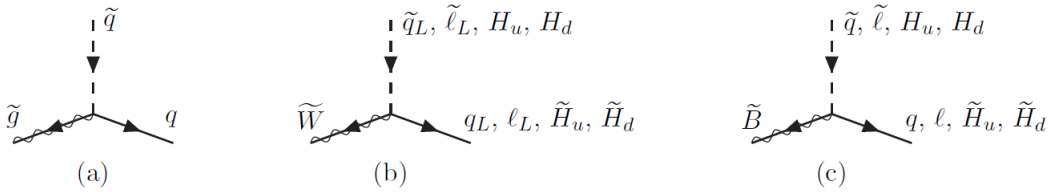

Figure 2.7: Couplings of the gluino (a), wino (b), and bino (c) to MSSM (scalar, fermion) pairs.

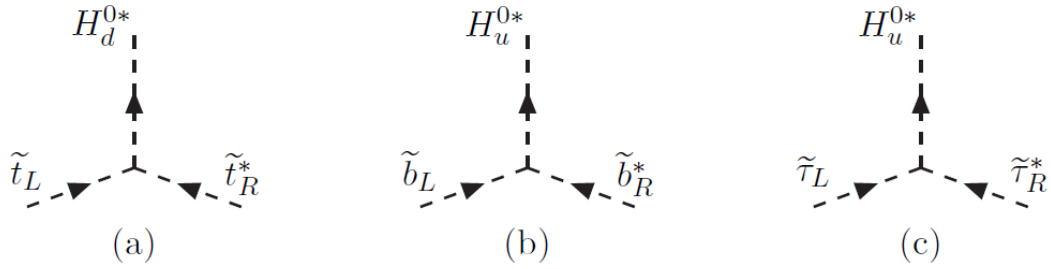

Figure 2.8: Examples of (scalar)^3 couplings.

The μ-term and the Yukawa couplings in the superpotential combine to yield (scalar)^3 couplings. Figure 2.8 shows some of these couplings, proportional to $\mu^* y_t$, $\mu^* y_b$ and $\mu^* y_\tau$ respectively. These play an important role in determining the mixing of top squarks, bottom squarks, and tau sleptons.

2.2.2.3 R-parity

There exist renormalizable terms not included in the supersymmetric Lagrangian which violate baryon and lepton number conservation. This type of interaction has not been experimentally observed; hence a new symmetry, called R-parity or matter parity, is introduced to eliminate terms in the renormalizable Lagrangian which would violate baryon and lepton number conservation. This is defined for each particle as:

$$P_R = (-1)^{3(B-L)+2s} \tag{2.24}$$

where s is its spin, B its baryon number, and L its lepton number. By construction, the SM particles are even under R-parity, while their superpartners, called sparticles, are odd (since their spins differ by 1/2). Conservation of R-parity implies that regular particles and sparticles cannot mix, and each interaction vertex in the supersymmetric theory must contain an even number of particles with $P_R = -1$. There are two phenomenologically crucial consequences to R-parity conservation:

- The lightest supersymmetric particle (LSP) is stable (there are no other $P_R = -1$ states it can decay to) and is a dark matter candidate.[2] Usually, the dark matter candidate of the MSSM is an admixture of the electroweak gauginos and Higgsinos, and is called a neutralino.
- Sparticles can only be pair-produced in collider experiments.

The MSSM is defined to conserve R-parity. This might seem arbitrary, but one way to motivate R-parity is with a $B - L$ continuous gauge symmetry which is spontaneously broken at a scale inaccessible to current experiments. It may also be possible to have gauged discrete symmetries that do not owe their exact conservation to an underlying continuous gauged symmetry, but rather to some other structure such as can occur in string theory.

2.2.2.4 Soft supersymmetry breaking in the MSSM

As already mentioned, since sparticles have not been observed, SUSY must be a broken symmetry. In the MSSM, SUSY-breaking is explicitly introduced by adding a new component ($\mathcal{L}_{\text{soft}}^{\text{MSSM}}$) to the Lagrangian. $\mathcal{L}_{\text{soft}}^{\text{MSSM}}$ only contains terms with positive mass

[2] In order to fit observations, it should have a mass of 100 GeV to 1 TeV, be neutral, and only interact through weak interactions and gravitational interactions.

dimension; this way, it does not cause ultraviolet divergences to appear in scalar masses (hence, the breaking is called soft). $\mathcal{L}_{\text{soft}}^{\text{MSSM}}$ introduces 105 new parameters (masses, phases and mixing angles) that were not present in the SM, and that cannot be rotated away by redefining the phases and flavor basis for the quark and lepton supermultiplets. Thus, in principle, SUSY-breaking (as opposed to SUSY itself) appears to introduce a tremendous arbitrariness in the Lagrangian.

There is strong experimental evidence that some powerful organizing principle must govern $\mathcal{L}_{\text{soft}}^{\text{MSSM}}$. This is because most of its new parameters imply flavor mixing or CP violating processes of the types that are severely constrained by experiment. The most intriguing way to evade these potentially dangerous flavor-changing and CP-violating effects in the MSSM is to assume (or explain) that SUSY-breaking is suitably *universal*. *Irrelevancy* is another possible scenario, which hypothesizes that the sparticles masses are extremely heavy, so that their contributions to flavor-changing and CP-violating diagrams are suppressed (this would make a SUSY search at the TeV scale fruitless). Other explanations include *alignment* (squark squared-mass matrices are arranged in flavor space to be aligned with the relevant Yukawa matrices in just the right way to avoid large flavor-changing effects), and having the MSSM be invariant under a new continuous $U(1)$ symmetry.

The soft-breaking universality relations can be presumed to be the result of some specific SUSY-breaking model, but there is no consensus among theorists as to the details of such a model. If SUSY is spontaneously broken in the vacuum state, then the vacuum must have positive energy. Thus, SUSY will be spontaneously broken if the expectation value any of the auxiliary fields F_i or D^a does not vanish in the vacuum state (non-zero VEV). This is called F-term and D-term SUSY-breaking, respectively. Spontaneous SUSY-breaking requires an extension of the MSSM, since the ultimate

SUSY-breaking order parameter cannot belong to any of the MSSM supermultiplets: a D-term VEV for $U(1)_Y$ does not lead to an acceptable spectrum, and there is no candidate gauge singlet whose F-term could develop a VEV. SUSY-breaking is thought to occur in a *hidden sector* of particles that have no (or tiny) direct couplings to the *visible sector* chiral supermultiplets of the MSSM. However, the two sectors do *communicate* to mediate SUSY-breaking from the hidden sector to the visible sector, resulting in the MSSM soft terms.

There are two main competing proposals for the nature of the mediating interactions. The first (and historically favored) is that they are associated with new physics, including gravity, that enters near the Planck scale. In this *gravity-mediated*, or Planck-scale-mediated supersymmetry breaking (PMSB) scenario, if SUSY is broken in the hidden sector by a VEV $\langle F \rangle$, then the soft terms in the visible sector should be roughly $m_{\text{soft}} \sim \langle F \rangle / M_{\text{P}}$. This implies that the scale associated with the origin of SUSY-breaking in the hidden sector should be $\sqrt{\langle F \rangle} \sim 10^{10}$ or 10^{11} GeV. A second idea is that the mediating interactions are the SM electroweak and QCD gauge interactions. In this gauge-mediated supersymmetry breaking (GMSB) scenario, the MSSM soft terms come from loop diagrams involving some messenger particles. The messengers are new chiral supermultiplets that couple to a SUSY-breaking VEV $\langle F \rangle$, and also have $SU(3)_C \otimes SU(2)_L \otimes U(1)_Y$ interactions, which provide the necessary connection to the MSSM. Then, using dimensional analysis:

$$m_{\text{soft}} \sim \frac{\alpha_a}{4\pi} \frac{\langle F \rangle}{M_{\text{mess}}} \tag{2.25}$$

where the $\alpha_a / 4\pi$ is a loop factor for Feynman diagrams involving gauge interactions, and M_{mess} is a characteristic scale of the masses of the messenger fields. If M_{mess} and $\langle F \rangle$ are roughly comparable, then the scale of SUSY-breaking can be as low as $\sqrt{\langle F \rangle} \sim 10^4$ GeV.

2.2.2.5 Sparticle decays

Assuming R-parity conservation, sparticles decay in cascades which always terminate in a LSP. Here we assume that the lightest neutralino $\tilde{\chi}_1^0$ is the LSP, which is the usual case in PMSB models. Another possibility is that the gravitino/goldstino $\tilde{G}$ is the LSP (in GMSB models), but we will not consider this here.

Neutralino and chargino: Each neutralino and chargino contains at least a small admixture of the electroweak gauginos, so they inherit couplings of weak interaction strength to (scalar, fermion) pairs. If sleptons or squarks are sufficiently light, a neutralino or chargino can decay into lepton+slepton or quark+squark. The lepton+slepton final states are favored, since sleptons are probably lighter than squarks. A neutralino or chargino may also decay into a lighter neutralino or chargino plus a Higgs scalar or an electroweak gauge boson, because they inherit the gaugino-higgsino-Higgs and gaugino-gaugino-vector boson couplings. The more kinematically favored two-body decays are:

$$\tilde{\chi}_i^0 \to Z\tilde{\chi}_j^0,\ W\tilde{\chi}_j^\pm,\ h^0\tilde{\chi}_j^0,\ l\tilde{l},\ \nu\tilde{\nu} \tag{2.26}$$

$$\tilde{\chi}_i^\pm \to W\tilde{\chi}_j^0,\ Z\tilde{\chi}_1^\pm,\ h^0\tilde{\chi}_1^\pm,\ l\tilde{\nu},\ \nu\tilde{l} \tag{2.27}$$

If two-body decays are kinematically forbidden, especially for $\tilde{\chi}_1^\pm$ and $\tilde{\chi}_2^0$, then we see three-body decays through off-shell gauge bosons, Higgs scalars, sleptons or squarks:

$$\tilde{\chi}_i^0 \to ff\tilde{\chi}_j^0, \quad \tilde{\chi}_i^0 \to ff'\tilde{\chi}_j^\pm, \quad \tilde{\chi}_i^\pm \to ff'\tilde{\chi}_j^0, \quad \tilde{\chi}_2^\pm \to ff\tilde{\chi}_1^\pm \tag{2.28}$$

where f and f' are distinct fermions of the same $SU(2)_L$ multiplet.

Slepton: Slepton-lepton-gaugino interactions are allowed, leading to the following two-body decays of weak interaction strength:

$$\tilde{l} \to l\tilde{\chi}_i^0, \quad \tilde{l} \to \nu\tilde{\chi}_i^\pm, \quad \tilde{\nu} \to \nu\tilde{\chi}_i^0, \quad \tilde{\nu} \to l\tilde{\chi}_i^\pm \tag{2.29}$$

Left-handed sleptons may prefer cascade decays over direct decays to the LSP if this is kinematically allowed, and if $\tilde{\chi}_1^{\pm}$ and $\tilde{\chi}_2^0$ are mostly wino. This is because slepton-lepton-wino interactions are proportional to the $SU(2)_L$ coupling g, whereas slepton-lepton-bino interactions are proportional to the $U(1)_Y$ coupling g', and $g \gg g'$.

Squark: The quark-squark-gluino coupling has QCD strength, so $\tilde{q} \to q\tilde{g}$ will dominate if kinematically allowed, otherwise the squark decays as follows: $\tilde{q} \to q\tilde{\chi}_i^0$ or $q'\tilde{\chi}_i^{\pm}$. The direct decay to the LSP is always kinematically favored, and for right-handed squarks it can dominate because $\tilde{\chi}_1^0$ is mostly bino. However, the left-handed squarks may strongly prefer cascade decays because the relevant squark-quark-wino couplings are much bigger than the squark-quark-bino couplings.

Gluino: Gluinos decay exclusively through squarks, which can be either on-shell or virtual. If two-body decays are allowed, $\tilde{g} \to t\tilde{t}_1$ and $\tilde{g} \to b\tilde{b}_1$ are likely to dominate since stops and sbottoms can be much lighter than the other squarks in many models. Otherwise the squarks will be off-shell, resulting in $\tilde{g} \to qq\tilde{\chi}_i^0$ and $\tilde{g} \to qq'\tilde{\chi}_i^{\pm}$. If a gluino decays to exactly one lepton (as opposed to zero or two leptons, which are the other possibilities), it will have either charge with equal probability (the gluino is a Majorana fermion), leading to the interesting possibility of same-sign dilepton signatures.

2.2.2.6 Signatures at a Hadron Collider

Hadron colliders with a center-of-mass energy ($\sqrt{s}$) at the TeV scale are well-suited for a SUSY search. The first such collider was the Tevatron, located in Batavia, IL. It was a $p\bar{p}$ collider with $\sqrt{s} = 1.96$ TeV. The current great collider is the LHC, which will be discussed in the next chapter; for now, we note that it is a pp collider with a center-of-mass energy $\sqrt{s} = 7$ TeV. At hadron colliders, sparticles must be pair-produced. This

can happen through interactions of electroweak strength:

$$q\bar{q} \to \tilde{\chi}_i^+ \tilde{\chi}_j^-,\ \tilde{\chi}_i^0 \tilde{\chi}_j^0, \quad u\bar{d} \to \tilde{\chi}_i^+ \tilde{\chi}_j^0 \tag{2.30}$$

$$q\bar{q} \to \tilde{l}_i^+ \tilde{l}_j^-,\ \tilde{\nu}_l \tilde{\nu}_l^*, \quad u\bar{d} \to \tilde{l}_L^+ \tilde{\nu}_l \tag{2.31}$$

or QCD strength:

$$gg \to \tilde{g}\tilde{g},\ \tilde{q}_i \tilde{q}_j^*, \quad gq \to \tilde{g}\tilde{q}_i, \quad q\bar{q} \to \tilde{g}\tilde{g},\ \tilde{q}_i \tilde{q}_j^*, \quad qq \to \tilde{q}_i \tilde{q}_j \tag{2.32}$$

One may crudely characterize the Tevatron as a quark-antiquark collider, and the LHC as a gluon-gluon and gluon-quark collider. If SUSY exists at the TeV scale, the LHC mainly produces gluinos and squarks, although associated production of a chargino or neutralino with a squark or gluino is also allowed (with a smaller cross-section); slepton pair production may also be observable.

Since the sparticles are pair-produced, and their decay chains always include at least one LSP, the final state will be characterized by a minimum of $2m_{\tilde{\chi}_1^0}$ of missing energy. At hadron colliders, the component of parton momenta parallel to the beam direction is unknown; thus, only the component of the missing energy that is manifest as momenta transverse to the colliding beams ($\not{E}_{\mathrm{T}}$) is detectable. In general, SUSY will present an experimental signature of the type n leptons, m jets, and $\not{E}_{\mathrm{T}}$, where n or m can be zero. There are important SM backgrounds to these signals, especially from processes involving production of W and Z bosons that decay to neutrinos, which provide the $\not{E}_{\mathrm{T}}$. Therefore it is important to identify specific signal region cuts for which the backgrounds can be reduced. In the LHC experiments, almost all possible final states are looked at by different analyses. Some modes may have a large SM background, but also a large signal efficiency, so discovery may be possible if the background is well-understood. Other modes may have almost negligible SM background, but may require some very specific assumptions about the SUSY model.

The classic SUSY signal at hadron colliders involves events with jets and $\not{E}_{\mathrm{T}}$, but no energetic isolated leptons. The latter requirement reduces backgrounds from SM processes with leptonic W decays (including $t\bar{t}$ decays). This mode has large backgrounds from QCD multijet events (where the jets are mismeasured), from events with leptonic W decays where the lepton is undetected, and from Z bosons decaying to neutrinos. However, clever techniques can be used to vastly suppress such backgrounds, and estimate what is left over. This mode can get important contributions from every type of sparticle pair production, except slepton pair production.

Another important possibility for the LHC is the single lepton plus jets plus $\not{E}_{\mathrm{T}}$ signal, which is the focus of this thesis. It has a potentially large SM background from production of $W \to l\nu$, either together with jets or from top decays, but like the previous mode, this can be suppressed through appropriate cuts. The single lepton plus jets signal can have an extremely large rate from various sparticle production modes, and may give a good discovery or confirmation signal at the LHC.

The same-charge dilepton signal has the advantage of relatively small backgrounds, since the largest SM sources for isolated lepton pairs can only yield opposite-charge dileptons. It can occur if the gluino decays with a significant branching fraction to hadrons plus a chargino, which can subsequently decay into a final state with a charged lepton, a neutrino, and a LSP.

The trilepton signal with three leptons, $\not{E}_{\mathrm{T}}$ and possible jets also has very small SM background. The likely origin of this signal at the LHC is if one of the pair-produced gluinos or squarks decays through a $\tilde{\chi}_1^{\pm}$ and the other through a $\tilde{\chi}_2^0$. This signature relies on the $\tilde{\chi}_2^0$ having a significant branching fraction for the three-body decay to leptons.

Final state leptons appearing in the signals listed above might be predominantly tau

(since many models predict the lightest stau being lighter than selectrons and smuons), and so a significant fraction could be realized as hadronic τ jets. If the lightest stop and sbottom are light enough, typical SUSY events may have high b-jet multiplicities.

2.2.3 SUSY parameter spaces of interest

The results of this analysis are expressed in terms of the constraints it places on SUSY parameters. The MSSM has too many free parameters to be suitable for this purpose. We use two frameworks to interpret our search results: the first is the CMSSM, which has far fewer free parameters than the MSSM because it makes assumptions about the nature of soft SUSY-breaking; the second is a specific topology by which SUSY particles can decay (colloquially referred to as a *simplified model*).

2.2.3.1 The Constrained Minimal Supersymmetric Standard Model

The CMSSM [10] incorporates a soft SUSY-breaking model influenced by minimal supergravity (mSUGRA). Supergravity is a field theory that combines the principles of SUSY and general relativity, making SUSY a local symmetry. It contains a spin-2 field quantized by the graviton, and a spin-3/2 field quantized by the gravitino. Local SUSY is spontaneously broken if the gravitino has a non-zero mass. The *minimal* in mSUGRA means it is an $N = 1$ realization of SUSY. CMSSM has the practical advantage that it requires only five input parameters to determine the low energy phenomenology from the GUT scale. These parameters are:

- m_0: The unified scalar (squarks, sleptons, H_u, H_d) mass. By unified, we refer to the fact that at the GUT scale, the scalar masses are identical to each other.

- $m_{1/2}$: The unified gaugino (gluino, wino, bino) mass. As before, unified refers to the identical gaugino masses at the GUT scale.
- A_0: The universal trilinear coupling (Higgs-sfermion-sfermion). Universal refers to the fact that all such couplings are identical at the GUT scale, regardless of the sfermion involved.
- $\tan\beta$: Defined as v_u/v_d, where v_u and v_d are the vacuum expectation values of H_u^0 and H_d^0, respectively.
- sign(μ): In CMSSM, the Higgs mixing parameter μ (defined in eq. 2.22) can be derived (up to a sign) from the other MSSM parameters by imposing the electroweak vacuum conditions for any given value of $\tan\beta$.

If the squarks and/or gluinos are kinematically accessible at the LHC, they are expected to have large production rates. Figure 2.9 shows the production cross sections of a squark (excluding stop) or a gluino. The nearly diagonal lines demarcate three regions:

- Region 1: Gluinos are heavier than any of the squarks. Typical decay chains are

$$\tilde{g} \to \tilde{q}\bar{q} \ , \ \tilde{q} \to q\chi, \tag{2.33}$$

  where χ can denote either a neutralino or a chargino, depending whether the quark that the squark is decaying to has identical charge or not.
- Region 2: Some squarks are heavier than gluinos, and others lighter, leading to complicated decay chains, like

$$\tilde{q}_L \to \tilde{g}q \ , \ \tilde{g} \to \tilde{b}\bar{b} \ , \ \tilde{b} \to b\chi. \tag{2.34}$$

- Region 3: Gluinos are lighter than any of the squarks. Expected decay chains are

$$\tilde{q} \to \tilde{g}q \ , \ \tilde{g} \to q\bar{q}\chi. \tag{2.35}$$

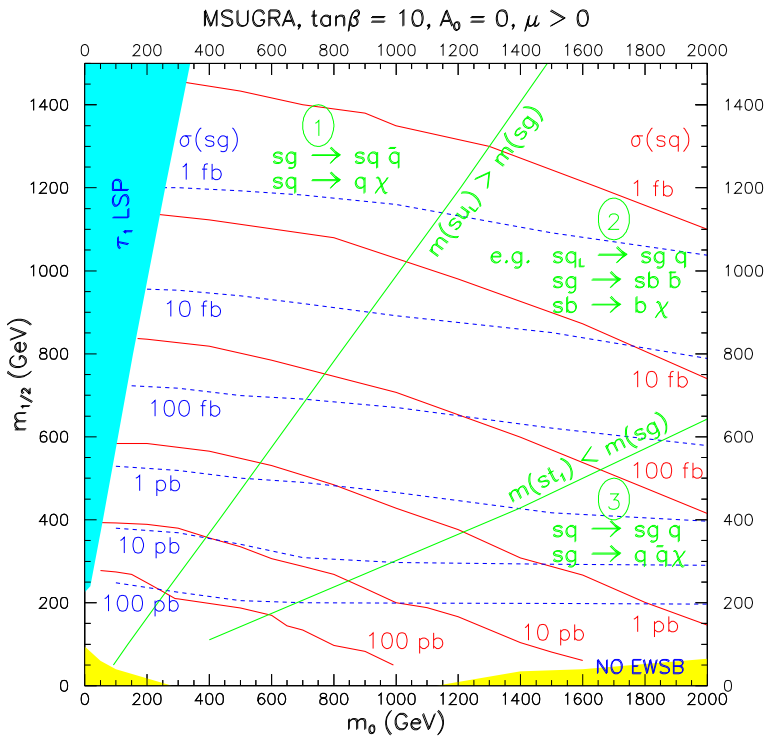

Figure 2.9: Regions of the $(m_0, m_{1/2})$ plane showing the production cross-sections and main squark and gluino decays.

In mSUGRA, the lightest two neutralinos are $\tilde{\chi}_1^0$ (dominantly bino-like), and $\tilde{\chi}_2^0$ (dominantly wino-like). The $\tilde{q}_R$ decays directly into $q\tilde{\chi}_1^0$ almost exclusively. But the $\tilde{q}_L$ usually has a non-negligible branching ratio to decay via the $\tilde{\chi}_2^0$ or $\tilde{\chi}_1^\pm$. The main decay modes of $\tilde{\chi}_2^0$, listed in the order of importance, are:

$$\tilde{\chi}_2^0 \to \tilde{l}l \ , \ \tilde{\nu}\nu \ , \ h^0\tilde{\chi}_1^0 \ , \ Z^0\tilde{\chi}_1^0 \ , \ l^+l^-\tilde{\chi}_1^0. \tag{2.36}$$

Less favorable modes can dominate when the more important processes are kinematically forbidden. The main decay modes of $\tilde{\chi}_1^\pm$ are:

$$\tilde{\chi}_1^\pm \to \tilde{l}\nu \ , \ \tilde{\nu}l \ , \ W^\pm\tilde{\chi}_1^0 \ , \ H^\pm\tilde{\chi}_1^0 \ , \ l^\pm\nu\tilde{\chi}_1^0. \tag{2.37}$$

In addition to scanning the CMSSM parameter space, we also consider specific benchmark points, referred to as *low-mass* (LM) and *high-mass* (HM). The LM points,

which are beyond the reach of the Tevatron, were chosen to evaluate the LHC's sensitivity to SUSY during early running. The HM points lie near the ultimate reach of the LHC. The LM points are listed in Table 2.2, and some LM and HM points are illustrated in Fig. 2.10. These points are not a *fair* statistical sampling of the allowed CMSSM parameter space, but span the range of theoretical possibilities, given our present knowledge. Using these points, it is possible to perform more detailed studies that are necessary to develop the analysis.

Table 2.2: CMSSM LM points (for all points, $\mu > 0$).

Benchmark	m_0	$m_{1/2}$	A_0	$\tan\beta$
LM0	200	160	-400	10
LM1	60	250	0	10
LM2	185	350	0	35
LM3	330	240	0	20
LM4	210	285	0	10
LM5	230	360	0	10
LM6	85	400	0	10
LM7	3000	230	0	10
LM8	500	300	-300	10
LM9	1450	175	0	50
LM10	3000	500	0	10
LM11	250	325	0	35
LM12	2545	247	-866	48
LM13	270	218	-553	40

2.2.3.2 T3w: A Simplified Model

Constrained SUSY models like CMSSM allow the large number of SUSY parameters to be reduced, and provide a way to assess and compare the expected sensitivity of different search strategies. However, even if SUSY proves to be the correct new fundamental theory, we should be open to the possibility that the specific mass patterns and signatures predicted by the constrained models may not be realized in nature. Therefore, in addition

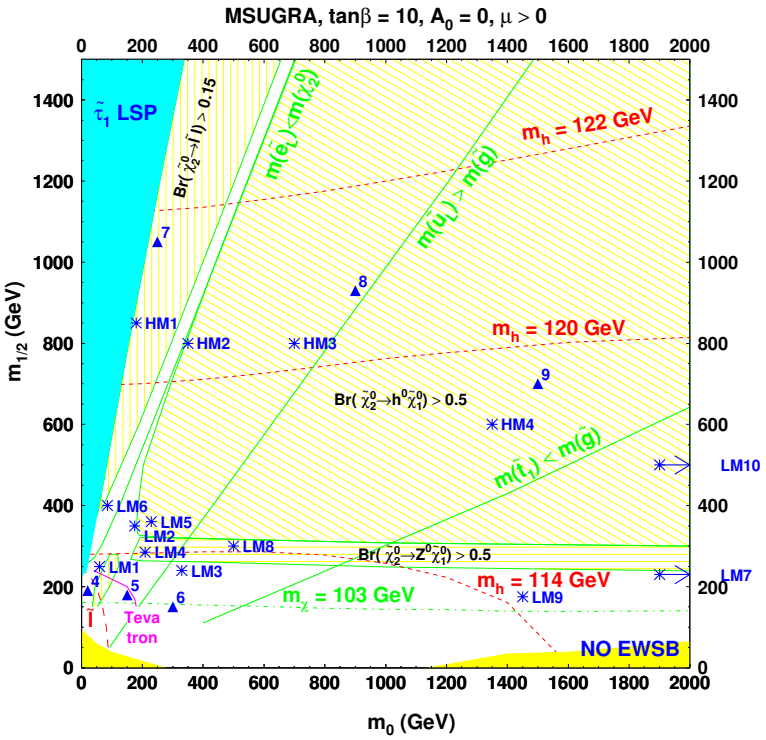

Figure 2.10: Position of benchmark points on the $(m_0, m_{1/2})$ plane.

to the traditional approach using constrained models, it is useful to pursue more flexible interpretations of search results.

In simplified models [11], a limited set of hypothetical particles and decay chains are introduced to produce a given topological signature. The amplitudes describing the production and decays of these particles are parametrized in terms of the particle masses and their branching ratios to daughter particles. Simplified models provide a benchmark for comparing search strategies which is more sensitive to the choice of kinematic selections and the final state topology than CMSSM. Furthermore, the presentation of signal acceptance and cross section upper limits as a function of the mass parameters of a simplified model can be used as a reference to place limits on different theoretical models.

The T3w simplified model is shown in Fig. 2.11. The production mode involves

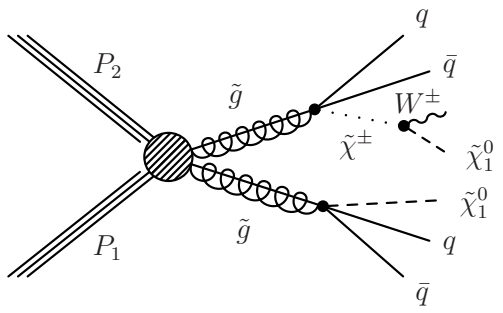

Figure 2.11: The T3w simplified model.

gluinos ($\tilde{g}$), which decay into massive neutralino LSPs ($\tilde{\chi}^0$). One gluino decays directly, and the other through a cascade involving a chargino ($\tilde{\chi}^{\pm}$) and subsequently a W boson (which must decay leptonically to result in our desired final state). To show cross section upper limits in the gluino-neutralino mass plane, the mass of the chargino needs to be fixed, and this is done through the x parameter, defined as:

$$x = \frac{\mathrm{m}_{\tilde{\chi}^{\pm}} - \mathrm{m}_{\tilde{g}}}{\mathrm{m}_{\tilde{\chi}^0} - \mathrm{m}_{\tilde{g}}}. \tag{2.38}$$

CHAPTER 3

EXPERIMENTAL APPARATUS

This search for supersymmetry uses data collected from proton-proton collisions obtained at CERN, the world's largest particle physics laboratory. The accelerator used to achieve these high-energy collisions is the Large Hadron Collider (LHC), and the experiment that detects the products of these collisions is the Compact Muon Solenoid (CMS). This chapter describes the CMS detector and data acquisition system. The discussion that is presented in this chapter can be found in greater detail elsewhere [12], and the figures used here are taken from the same source.

3.1 The Large Hadron Collider

The LHC is a particle accelerator that is 27 km in diameter, located at a mean depth of 100 m underground. It is built in the same tunnel as the Large Electron-Positron Collider (the previous accelerator at CERN), the rock layers above providing a natural shielding from incoming (cosmic) and outgoing radiation. It is designed to provide head-on collisions of two proton beams, each at 7 TeV, with an instantaneous luminosity of 10^{34} cm^{-2} s^{-1}. However, due to risks revealed in an accident that occurred on September 19, 2008, the peak energy cannot be reached till repairs have been performed during the long shutdown scheduled at the end of 2012 [13]. Hence, during the 2010 and 2011 runs, each proton beam was at 3.5 TeV.

The large center-of-mass energy and instantaneous luminosity place significant challenges on any detector associated with the LHC. The total proton-proton cross-section at $\sqrt{s} = 7$ TeV is roughly 70 mb. This implies inelastic collisions at $\sim 10^9$ Hz. The online event selection process (trigger) must reduce the rate dramatically to $\sim 10^2$ Hz for

storage and offline analysis. The time between bunch crossings is a mere 50 ns, placing severe demands on the read-out and trigger systems. During the 2011 run, an average of 7 inelastic collisions were superimposed on the event of interest, referred to as pile-up. Pile-up can cause the products of the interaction being studied to be confused with those from other interactions. This problem is compounded when the response time of a detector element is longer than the interval between bunch crossings. The effect of pile-up can be reduced by using high-granularity detectors with good time resolution, resulting in low occupancy. This requires a large number of detector channels, which must be well-synchronized. The LHC is a high radiation environment, requiring radiation-hard detectors and front-end electronics. Finally, in order to achieve the ambitious physics goals of the LHC, a detector must be able to reconstruct physics objects efficiently, with very good resolution and low probability of mis-identification. The CMS detector, described in depth in the next section, is designed to successfully address these challenges.

3.2 The Compact Muon Solenoid

The CMS detector is 21.6 m long, has a diameter of 14.6 m, and weighs 12.5 kt. Its layout can be seen in Fig. 3.1. A crucial component for the precise momentum measurement of high-energy charged particles is a magnet with a large bending power to deflect the charged particles from a straight line trajectory. This is achieved by a 13 m long, 6 m inner-diameter, 3.8 T superconducting solenoid which is at the heart of the CMS detector. The solenoid provides a bending power of 12 Tm before the muon bending angle is measured by the muon system (Sec. 3.2.4). The strong return field saturates the 1.5 m of iron that interleave the muon detectors. The bore of the magnet coil is large enough to accommodate within it the inner tracker (Sec. 3.2.1) and the calorimetry. The inner tracker consists of a silicon pixel detector and a silicon microstrip

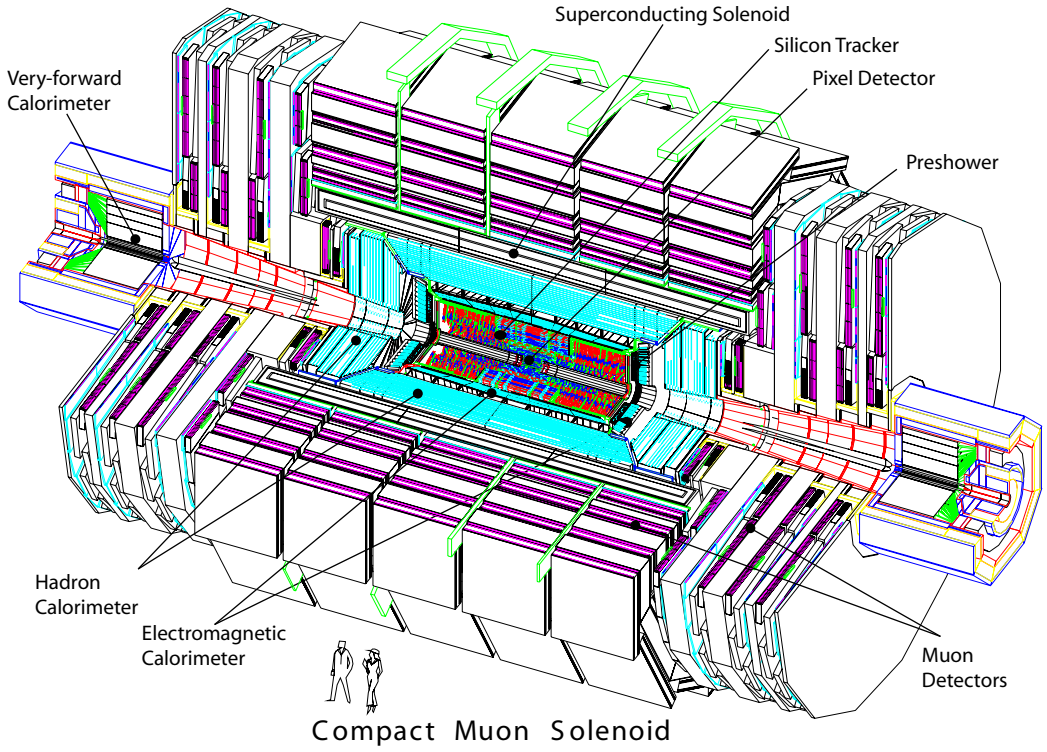

Figure 3.1: A perspective view of the CMS detector.

detector. The main calorimeters are the electromagnetic calorimeter (ECAL, Sec. 3.2.2) and the hadronic calorimeter (HCAL, Sec. 3.2.3). Additionally, CMS has the forward calorimeters, known as CASTOR and zero degree calorimeter (ZDC), but information from them is not used in this analysis.

The CMS coordinate system is centered at the nominal collision point inside the experiment, with the y axis pointing vertically upward, and the x axis pointing radially inward toward the center of the LHC. Thus, the z axis points along the beam direction. Coordinates in the detector are specified using the azimuth ϕ in the plane transverse to the beam direction and the pseudorapidity $\eta = -\ln[\tan(\theta/2)]$, where θ is the polar angle relative to the beam axis. The region of the detector with $|\eta| < 1.5$ is referred to as the *barrel*, while the *endcap* has $1.5 < |\eta| < 2.5$. Transverse energy is defined as $E_{\mathrm{T}} = \mathrm{E}\sin(\theta)$, and transverse momentum p_{T} is defined analogously.

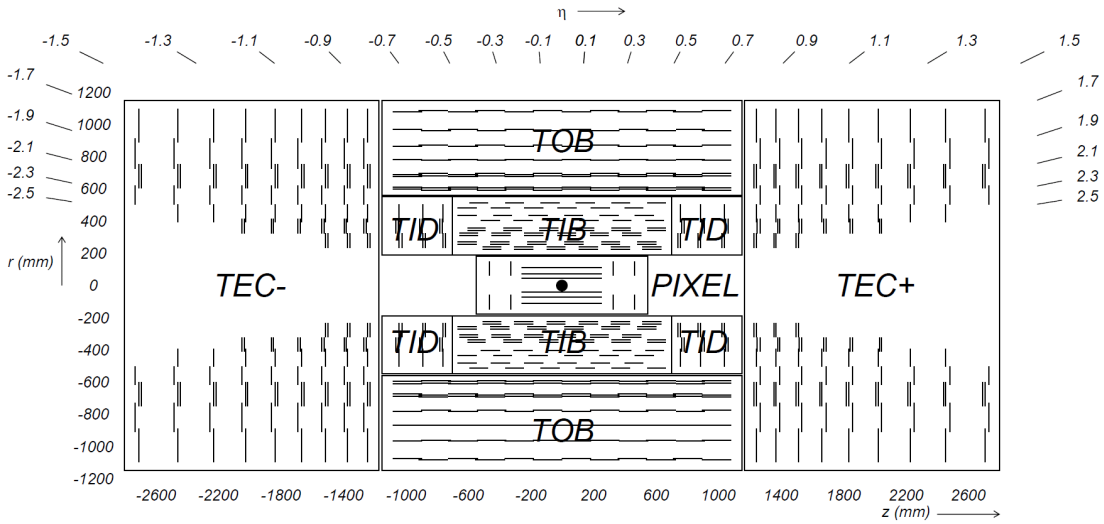

Figure 3.2: Schematic cross section through the CMS tracker.

3.2.1 Inner tracking system

The inner tracker is used to reconstruct the trajectories of charged particles. It surrounds the interaction point, has a length of 5.8 m and a diameter of 2.5 m. Combined with the ECAL, it is used to identify electrons, and combined with the muon system, it is used for muon identification. It can precisely measure secondary vertices and impact parameters of charged particles, used to identify heavy flavor decays that are characteristic of many interesting physics processes. It satisfies stringent requirements on granularity, speed and radiation hardness by use of silicon detector technology. High granularity and speed imply a high power density of the on-detector electronics, which requires efficient cooling. This is in direct conflict with the aim to keep material budget to a minimum in order to limit multiple scattering, Bremsstrahlung, photon conversion and nuclear interactions. A compromise had to be found in this respect. Consequently, the inner tracker has a fast enough response to be a part of the software-based High Level Trigger, but not fast enough to be a part of the hardware-based Level 1 trigger system (Sec. 3.2.5).

Figure 3.2 shows a schematic cross section through the CMS tracker. It is composed

of a pixel detector with three barrel layers (BPIX) at radii between 4.4 cm and 10.2 cm and a silicon strip tracker with 10 barrel detection layers (Tracker Inner Barrel, TIB, Tracker Outer Barrel, TOB) extending outwards to a radius of 1.1 m. Each system is completed by endcaps which consist of 2 disks in the pixel detector (FPIX) and 3 plus 9 disks in the strip tracker (Tracker Inner Disk, TID, and Tracker endcap, TEC) on each side of the barrel, extending the acceptance of the tracker up to $|\eta| < 2.5$. The pixel detector is designed to precisely measure the impact parameter of charged particles and the position of secondary vertices, and to achieve similar hit resolution in both $r\phi$ and z directions. It delivers three high precision points on each charged particle trajectory. It covers an area of about 1 m^2 and has 66 million pixels. The spatial resolution is about $15 - 20$ μm.

The radial region between 20 cm and 116 cm is occupied by the silicon strip tracker, which provides the necessary granularity required to deal with high track multiplicities. It has a total of 9.3 million strips and 198 m^2 of active silicon area. The TIB and TID extend to a radius of 55 cm, and are surrounded by the TOB. The TOB extends in z between ± 118 cm. Beyond this z range, the TEC covers the region 124 cm $< |z| <$ 282 cm and 22.5 cm $< |r| <$ 113.5 cm. Some layers of the strip tracker are single-layered, and some double-layered. Double-layered modules, which have a second micro-strip detector module mounted back-to-back with a stereo angle of 100 mrad, allow the z (r) coordinate of a hit to be measured in the barrel (endcap). In the TIB, the strip pitch is 80 μm on layers 1 and 2, and 120 μm on layers 3 and 4; it varies between 100 μm and 141 μm in the TID, and between 97 μm and 184 μm in the TEC. The TOB has strip pitches of 183 μm on the first 4 layers, and 122 μm on layers 5 and 6. The single point resolution of the strip tracker is several tens of microns. TIB and TID in conjunction deliver up to 4 $r\phi$ measurements on a trajectory, the TOB another 6 $r\phi$ measurements, and the TEC up to 9 ϕ measurements.

For single muons (charged particles for which the tracker performance is the best, since muons are minimum ionizing particles), high momentum tracks (100 GeV) have a p_T resolution of $1 - 2\%$ for $|\eta| < 1.6$; for $1.6 < |\eta| < 2.5$, the resolution is degraded due to the reduced lever arm. The impact parameter resolution reaches 10 μm for high p_T tracks, dominated by the resolution of the first pixel hit, while at lower momentum it is degraded by multiple scattering. The reconstruction efficiency for muon tracks is about 99% over most of the acceptance. At high η, the efficiency drops mainly due to the reduced coverage by the pixel forward disks. For pions, the efficiency is lower due to material interactions.

3.2.2 The electromagnetic calorimeter

The ECAL, illustrated in Fig. 3.3, is a hermetic homogeneous calorimeter made of radiation resistant lead tungstate ($PbWO_4$) crystals. When an electron or photon passes through the ECAL, the result is a cascade or shower of electromagnetic particles that contain the energy of the original particle. The shower continues till the cascade particles no longer have enough energy to produce pairs, and are absorbed into the material of the calorimeter. Pions occasionally interact with the ECAL, but the HCAL usually gets the bulk of their energy deposit. Muons deposit little energy ($\sim$ 0.5 GeV) in the ECAL.

The scintillation decay time of the $PbWO_4$ crystals is of the same order of magnitude as the LHC bunch crossing time: about 80% of the light is emitted in 25 ns. There are 61200 crystals mounted in the central barrel (EB), and 7324 crystals in each of the two endcaps (EE). The EB granularity is 360-fold in ϕ and 2×85-fold in η. The EE consists of identically shaped crystals grouped in mechanical units of 5×5 crystals

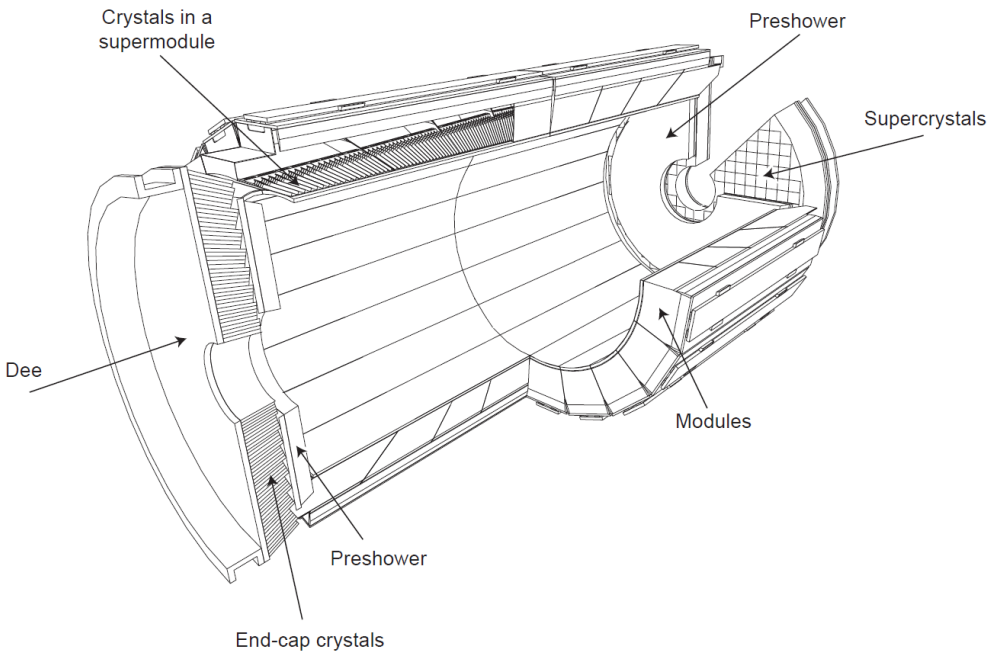

Figure 3.3: Layout of the CMS electromagnetic calorimeter showing the arrangement of crystal modules, supermodules and endcaps, with the preshower in front.

consisting of a carbon-fibre alveola structure. Each endcap is divided into 2 halves, or *Dees*. The nominal operating temperature of the ECAL is 18 °C. The cooling system, which employs flowing water, has to comply with this severe thermal constraint.

The photodetectors used are avalanche photodiodes (APDs) in the EB and vacuum phototriodes (VPTs) in the EE. The photodetectors need to be fast, radiation tolerant and be able to operate in the strong magnetic field. In addition, because of the small light yield of the crystals (about 4.5 photoelectrons per MeV at 18 °C), they should amplify and be insensitive to particles traversing them. The configuration of the magnetic field and the expected level of radiation led to different choices between EB and EE. The lower quantum efficiency and internal gain of VPTs compared to APDs is offset by their larger surface coverage on the back face of the crystals.

A preshower (ES) detector is located in front of the EE. Its main aim is to identify neutral pions in the endcaps within $1.653 < |\eta| < 2.6$. It also helps distinguish electrons from minimum ionizing particles, and improves the position determination of electrons and photons with its high granularity. It is a sampling calorimeter with two layers: lead radiators initiate electromagnetic showers from incoming photons and electrons, while silicon strip sensors placed after each radiator measure the deposited energy and the transverse shower profiles. A major design consideration is that all lead is covered by silicon sensors, taking into account the effects of shower spread, primary vertex spread etc. The lead planes are arranged in two Dees, one on each side of the beam pipe, with the same orientation as the crystal Dees. The total thickness of the ES is 20 cm.

One of the driving criteria in the ECAL design was the detection of the decay of the postulated Higgs boson to two photons. This capability is enhanced by the good energy resolution provided by a homogeneous crystal calorimeter. To achieve the most accurate energy measurements for electrons and photons, the ECAL needs to be well-calibrated. ECAL calibration is composed of a global component, giving the absolute energy scale, and a channel-to-channel relative component, referred to as intercalibration. The ultimate intercalibration precision is achieved with physics events like $W \to e\nu$, $\pi^0 \to \gamma\gamma$, and $\eta \to \gamma\gamma$. During intercalibration, ECAL response must remain stable to high precision. Changes in crystal transparency due to radiation damage are tracked and corrected using the laser monitoring system. The ECAL is able to accurately measure a wide range of energies, from 2 GeV up to a few TeV. The lower energy is important for the reconstruction of the Higgs boson decaying to b-jets; the upper energy is important for the discovery of new particle resonances. For energies $\sim$ 100 GeV, the energy resolution is better than 1%.

3.2.3 The hadron calorimeter

The HCAL, shown in Fig. 3.4, is crucial for the measurement of hadron jets and apparent missing transverse momentum (due to neutrinos or exotic particles that do not interact with the CMS detector). The HCAL is a hermetic sampling calorimeter, and uses alternating layers of absorber and scintillator. When hadrons pass sufficiently close to the absorber nuclei in the HCAL, there is a strong interaction between the hadrons and the protons and neutrons of the nearby nucleus. These interactions produce additional particles that share the energy of the original high-energy particle, each of which strongly interacts with nearby nuclei, resulting in a cascade of particles similar to an electromagnetic shower. This will continue until the particles all begin to slow down and get absorbed into the HCAL. The HCAL barrel (HB) and endcaps (HE) sit behind the inner tracker and ECAL as seen from the interaction point. The HB is radially restricted between the outer edge of the ECAL (R = 1.77 m) and the inner edge of the magnet coil (R = 2.95 m). This limits the total amount of material which can be put in to absorb the hadronic shower. Therefore, an outer hadron calorimeter (HO) is placed outside the solenoid complementing the barrel calorimeter. Beyond $|\eta| = 3$, the forward HCAL (HF) placed at 11.2 m from the interaction point extend the coverage to $|\eta| = 5.2$ using a Cherenkov-based, radiation-hard technology.

The HB is divided into two half-barrel sections, with coverage up to $|\eta| < 1.3$. It consists of 36 identical azimuthal wedges constructed out of flat brass absorber plates aligned parallel to the beam axis. The plastic tile scintillator, chosen for its long-term stability and moderate radiation hardness, is divided into 16 η sectors. The HCAL consists of about 70 000 tiles. Light from each tile is collected with a wavelength-shifting fiber. The HE has a coverage of $1.3 < |\eta| < 3$, a region containing about 34% of the particles produced in the final state. The high luminosity of the LHC requires HE to handle

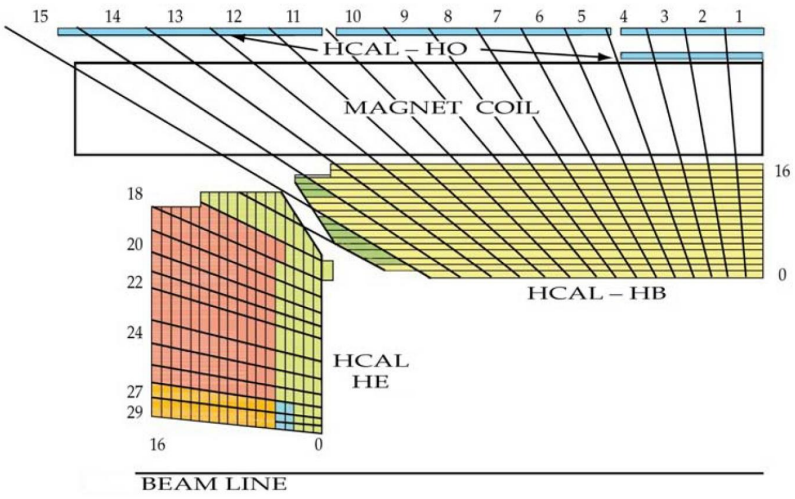

Figure 3.4: The HCAL tower segmentation in the *rz* plane for one-fourth of the HB, HO, and HE detectors. The shading represents the optical grouping of scintillator layers into different longitudinal readouts.

high (MHz) counting rates and have high radiation tolerance. Since the calorimeter is inserted into the ends of the solenoid, the absorber must be non-magnetic, have a maximum number of interaction lengths to contain hadronic showers, have good mechanical properties and be affordable: brass fulfils these criteria. The absorber design is driven by the need to minimize the cracks between HB and HE, and not single-particle energy resolution, since the resolution of jets in HE is limited by pile-up, magnetic field effects, and parton fragmentation.

The HO utilizes the solenoid coil as an additional absorber and is used to identify late starting showers and to measure the shower energy deposited after HB. The mean fraction of energy in HO increases from 0.38% for 10 GeV pions to 4.3% for 300 GeV pions. The HF experiences unprecedented particle fluxes: on average, it gets 760 GeV per proton-proton interaction, compared to only 100 GeV for the rest of the detector. Moreover, this energy is not uniformly distributed, but has a pronounced maximum at the highest values of $|\eta|$. The charged hadron rates are also extremely high. Steel

interleaved with quartz fibers (as the active medium) was chosen to survive under these harsh conditions. The HCAL energy resolution is about 30% for 10 GeV pions, and about 10% for 100 GeV pions.

3.2.4 Muon detectors

High p_T muons provide the cleanest signature for many of the SM processes studied at the LHC, as well as a signature for new discoveries. The muon detector system, shown in Fig. 3.5, must identify muons and trigger on them with large efficiency, even in the presence of multi-muon events, up to $|\eta| = 2.1$ and with no acceptance loss. It should be able to unambiguously assign a bunch crossing to each muon candidate, and correctly assign charge even for low p_T muons. For large p_T tracks ($p_T > 200$ GeV), the muon p_T determined by measuring the sagitta of the global muon track (obtained by combining the inner tracker information with the muon detector information) should be precise enough to substantially improve the precision of the p_T measured by the inner tracker alone.

Besides the constraints mentioned above, there are two main factors to consider when choosing the type of detector technology: first, the very large surface area to be covered, and second, the different radiation environments involved. For identifying and measuring muons, there are three types of gaseous detectors involved. In the barrel region ($|\eta| < 1.2$), where the neutron induced background is small, as is the muon rate and the residual magnetic field (< 0.4 T), drift tube (DT) chambers are a good choice. In the two endcaps, where all three of these quantities are high, cathode strip chambers (CSC) are utilized, and cover the region up to $|\eta| < 2.4$. In addition to this, resistive plate chambers (RPC) extend over the barrel as well as the endcap. RPCs have a fast

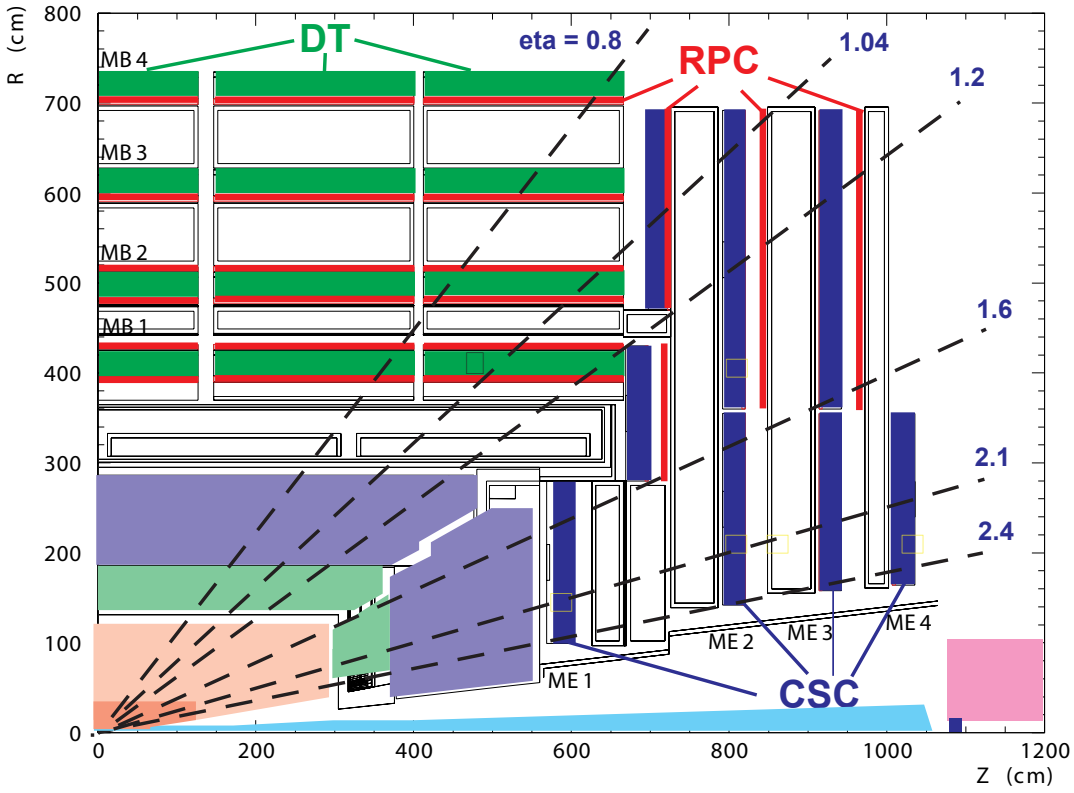

Figure 3.5: A 1/4 view of the CMS muon detectors.

response, with good time resolution, though their position resolution is coarser than the DTs or CSCs. Hence RPCs can unambiguously identify the correct bunch crossing. The DTs or CSCs and the RPCs provide two independent and complementary sources of information, and operate within the Level 1 trigger.

The magnet return yoke of the CMS detector is subdivided into 5 wheels and 2×3 endcap discs, and is instrumented with a system of muon chambers. In the Muon Barrel (MB) region, 4 stations of detectors are arranged in cylinders interleaved with the iron yoke. The segmentation along the beam direction follows the 5 wheels of the yoke (labeled YB–2 for the farthest wheel in $-z$, and YB+2 for the farthest in $+z$). In each of the endcaps, the CSCs and RPCs are arranged in 4 disks perpendicular to the beam (ME1 to ME4), and in concentric rings, 3 rings in the innermost station, and 2 in the

others. In total, the muon system contains of order 25 000 m^2 of active detection planes, and nearly 1 million electronic channels.

DT Chambers in the four different MB stations are staggered so that a high p_T muon produced near a sector boundary crosses at least 3 out of the 4 stations. Each station is designed to give a muon vector in space, with a precision better than 100 μm in position in the $r\phi$ plane, and approximately 1 mrad in ϕ. The muon endcap (ME) is arranged in 4 disks (ME1 - ME4), referred to as stations. Each station is subdivided into rings. Each ring is filled with CSCs, which are trapezoidal multiwire proportional chambers. Closely spaced wires make the CSC a fast detector (response time of $\sim$ 4.5 ns), which is why it is used in the Level 1 Trigger. However, it leads to a coarser position resolution than the DTs: the spatial resolution in the $r\phi$ plane provided by each chamber from the strips is typically about 200 μm, and the angular resolution in ϕ is of order 10 mrad. CSCs can operate in large and non-uniform magnetic field without significant deterioration in their performance. Each RPC detector consists of a double-gap bakelite chamber operating in avalanche mode to ensure good operation at high rates (up to 10 kHz/cm^{-2}). RPCs guarantee a precise bunch crossing assignment thanks to their fast response and good time resolution.

The muon detection system is capable of identifying single and multi-muon events with well determined p_T in the range of a few GeV to TeV. The reconstruction efficiency is greater than 96% if $p_T > 20$ GeV (the range that is relevant for this analysis) and around 80% for $p_T = 5$ GeV. The momentum resolution $\Delta p_T/p_T$ is $1 - 1.5\%$ when $p_T \sim 10$ GeV and $6 - 17\%$ when $p_T \sim 1$ TeV (the large range is due to η dependence). The momentum resolution of muon tracks up to $p_T = 200$ GeV reconstructed in the muon system alone is dominated by multiple scattering. Thus, at low momentum, the best momentum resolution for muons is obtained from the silicon tracker. At higher

momentum, the characteristics of the muon system allow the improvement of the muon momentum resolution by combining the muon track from the silicon detector, *tracker track*, with the muon track from the muon system, *stand-alone muon*, into a *global muon* track using track matching. A complementary approach to global muons consists of considering all silicon tracker tracks and identifying them as muons by looking for compatible signatures in the calorimeters and in the muon system. Muons identified with this method are called *tracker muons*.

3.2.5 Trigger and Data Acquisition System

As mentioned previously, a reduction by a factor of 10^7 needs to be achieved when going from the inelastic collision rate at the nominal LHC luminosity of 10^{34} cm^{-2} s^{-1} to the rate at which collision data can be stored. CMS does this by using two components: the Level 1 trigger (L1T) system, a fast hardware-based trigger, and the High Level Trigger (HLT) system, which is software-based. The reduction in data is accomplished by triggering on event features that are characteristic of rare and interesting physics processes.

The L1T uses only coarsely segmented data from calorimeter and muon detectors, while holding all the high-resolution data in pipeline memories in the front-end electronics. It forwards no more than 100 kHz of the stored events to the HLT. For an event to pass the L1T, it must meet certain threshold requirements on the p_{T} or E_{T} of individual physics objects, or on scalar or vector sums of the same quantities. The L1T is comprised of several subcomponents associated with the different subdetectors: the bunch crossing timing, the L1 muon systems (CSC, DT, RPC) which feed the Global Muon Trigger, and the L1 calorimetry (ECAL, HCAL, HF) which feed the Regional

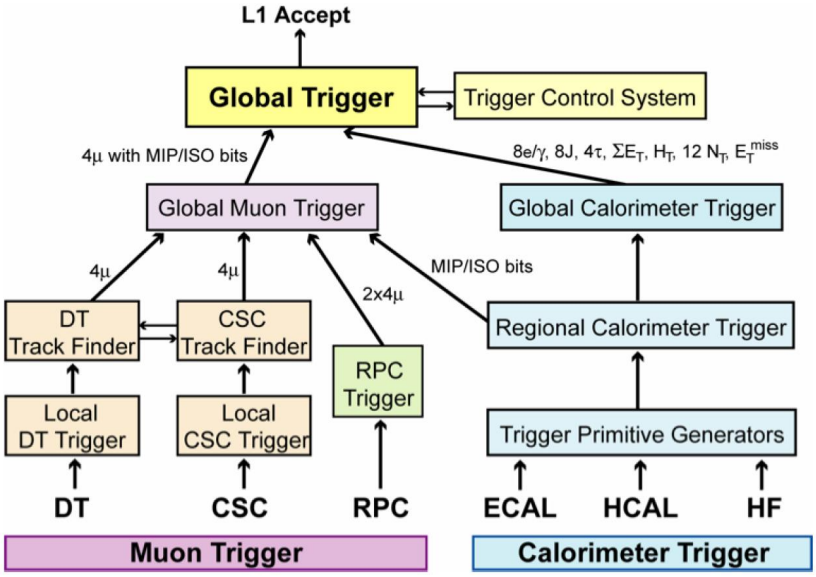

Figure 3.6: Level 1 trigger architecture.

Calorimeter Trigger and then the Global Calorimeter Trigger. All these inputs are passed to the Global Trigger (GT), as shown in Fig. 3.6. The GT has the ability to provide up to 128 trigger algorithms to select an event based on logical combinations of L1 objects, such as muons, jets, or calorimeter energy sums. In addition, there are 64 *technical triggers* that are used for detector diagnostics or monitoring. The L1T has a latency of 3.2 μs, after which the detector information from the event must either be dropped or sent to the front-end readout buffers. Events that are retained undergo signal processing, zero-suppression, data compression, and then sent to the HLT.

The HLT is capable of a greater rejection power than the L1T because it has additional time to calculate kinematic variables using complete read-out data from all detector subsystems necessary for a particular reconstruction. It relies upon about a thousand commercial processors to perform complex calculations similar to those made in the the analysis offline software (Chapter 4). Since there are timing constraints that the HLT has

to satisfy (average execution time for a trigger path should be 10 ms, with an upper limit of 40 ms), the reconstruction algorithms employed online are often simpler than what is used offline, and care has to be taken to ensure that this does not affect the physics analyses.

Events that are accepted by the HLT are sent to the Storage Manager, the last piece of the data-handling chain. The Storage Manager has two principal purposes. The first is to collect the events from the processor farm of HLT, and store the events in files for later transfer and processing. These data files are then assigned to different output streams, each stream being defined as a collection of several HLT trigger paths. The files are routed according to which HLT paths were triggered by a given event, and which streams those paths belong to. The grouping is usually determined based on offline usage (e.g., *physics* stream, *express* stream, *calibration* streams, etc.). The second function of the storage manager is to act as an event server for calibration and monitoring purposes.

CHAPTER 4

EVENT RECONSTRUCTION

When final state particles emerge from pp collisions, they produce signals in the CMS detector. These signals are then read out, and used to reconstruct the particles as *physics objects*, which are used to define the signature of interesting physics events. The physics objects relevant to this analysis are leptons (electrons and muons), jets, and apparent missing transverse momentum (arising from neutrinos and possible new physics particles that do not interact with the detector). Physics objects are reconstructed both online and offline: online objects are used for triggering, while for any physics analysis, it is the offline objects that are utilized. This chapter discusses this offline reconstruction. The procedure for electrons and muons is discussed in Sec. 4.1 and Sec. 4.2, respectively. Jet reconstruction is based on a CMS-specific algorithm known as Particle-Flow (PF); this is discussed in Sec. 4.3. Section 4.4 explains the reconstruction of missing transverse momentum.

4.1 Electrons

Electron reconstruction [14] begins with the clustering of ECAL energy deposits. In the absence of material interactions in the beampipe or tracker, approximately 94% of the incident energy of a single electron is contained in 3×3 crystals, and 97% in 5×5 crystals. Due to the strong magnetic field, and electrons undergoing Bremsstahlung, the energy deposited in the ECAL is spread in ϕ. This energy is clustered by building a group of clusters, a *supercluster* (SC), which is extended in ϕ. Figure 4.1(a) shows the material budget of the CMS detector. Figure 4.1(b) shows an illustration of an electron as it radiates photons when traveling through the tracker layers. CMS employs a *hybrid* algorithm in the EB, and an *island* algorithm in the EE; these are discussed in greater

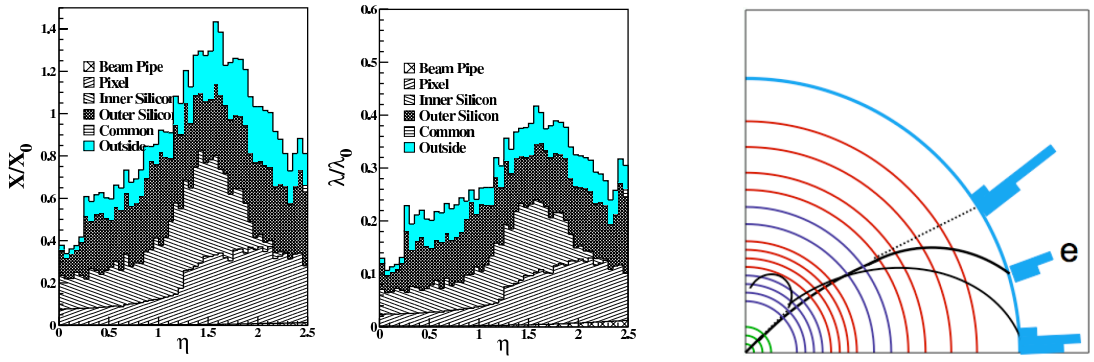

(a) (b)

Figure 4.1: Left: Material budget of the CMS detector as a function of η [12]. Right: Cartoon of an electron radiating photons when traveling through the tracker layers [12].

detail elsewhere [15].

Non-overlapping clusters are grouped into a SC. The procedure is seeded by searching for the most energetic cluster (seed cluster), and then by collecting other clusters in a fixed search area around the seed position. The clusters belonging to radiation from a single electron are aligned in η, but spread in ϕ. By collecting all the clusters in a narrow η window, whose size is dictated by the η resolution of the detector, it is possible to recover most of the radiated energy. The energy of the SC is corrected based on the number of crystals in the seed cluster, and to remove any residual η dependence. The position of the shower is obtained by calculating the energy-weighted mean position of the crystals in the SC. There are two issues with this approach: one is related to the definition of the position of a crystal, the other to the fact that a simple energy-weighted mean is biased towards the center of the crystal containing the largest energy deposit (seed crystal). How these issues are handled is discussed elsewhere [15].

To complete the process of electron reconstruction, the SC needs to be associated with a track in the inner tracker. Electron tracking begins with the formation of a *pixel seed*, which involves finding a pair of hits in the inner tracker consistent with the trajectory of electron: the assumption is that the curvature of the trajectory is given by the E_{T}

of the SC, and that the trajectory comes from the origin. The pixel seed itself is a vector located at the outer hit position, pointing in the direction of the electron's trajectory, and serves as the starting point for tracking. The standard seed-finding process is referred to as *pixel-matching*, since the hit pair is usually located in the pixel layers.

A major difficulty of electron reconstruction is that electrons can undergo Bremsstrahlung in the tracker material. The radiation affects both the energy and momentum measurement, and this effect depends on the material thickness. To account for Bremsstrahlung losses, CMS employs a Gaussian-Sum Filter (GSF) track fit. This fit uses the Bethe-Heitler model of electron energy loss, and approximates the energy loss distribution as a sum of Gaussian distributions. Different Gaussians model different degrees of hardness of the Bremsstrahlung in the layer under consideration. The GSF fit allows for good momentum resolution at the vertex while also providing a meaningful estimate of the momentum at the outermost part of the tracker.

The matching of the track and SC is based on their angular separation (ΔR):

$$\Delta R = \sqrt{(\eta_1 - \eta_2)^2 + (\phi_1 - \phi_2)^2}. \tag{4.1}$$

where (η_1, ϕ_1) and (η_2, ϕ_2) are the coordinates of any two positions (in this case, the track position at the ECAL, and the SC position). The energy of the electron is the error-weighted average of the corrected SC energy and the magnitude of the track momentum (since the mass of the electron is negligible when compared to GeV scale momenta). Figure 4.2(a) shows the improvement to the energy resolution of the electron by combining the track and SC information. Figure 4.2(b) shows the energy resolution of 120 GeV electrons before and after corrections.

We consider electrons over the range $|\eta| < 2.4$, excluding the overlap between the barrel and endcap ($1.44 < |\eta| < 1.57$). There are four types of electron candidates: prompt, non-prompt, conversion, and fake. Prompt electrons mainly come from the de-

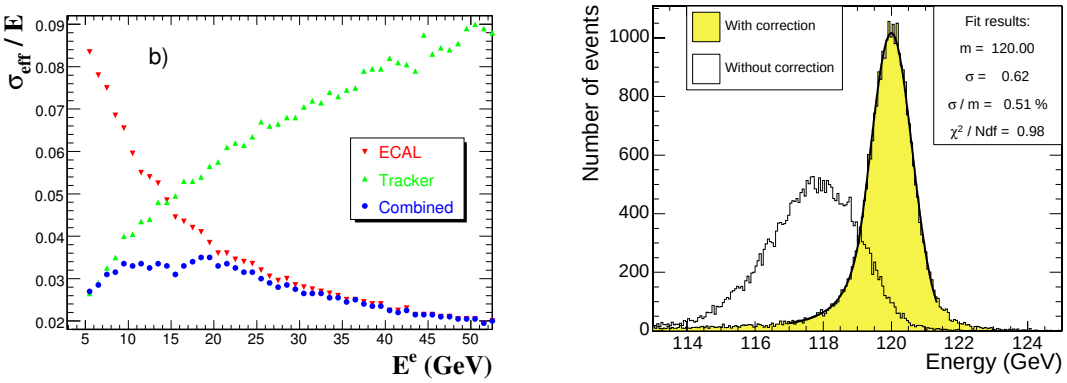

(a) (b)

Figure 4.2: Left: Energy resolution uncertainty for an electron when using the ECAL (red) and tracker (green) information individually, and when using the combined information (blue), as a function of electron energy [12]. Right: The energy resolution of 120 GeV electrons before (unshaded) and after (shaded) corrections [12].

cay of W and Z bosons, and are of great importance to us. Non-prompt electrons arise from *b* or *c* quark decaying to an electron. Although these electrons are usually not isolated within the quark jet, since there is a significant amount of nearby electromagnetic and/or hadronic activity, the kick from the quark decay might knock the electron out of the jet enough for it to appear isolated. Conversion electrons come from a photon producing an electron-positron pair in the tracker. Fake electrons are a result of reconstruction error: a coincidence of a jet depositing a large amount of energy in the ECAL and a nearby (matched) single, high-p_{T} track is misinterpreted as an electron. Non-prompt, conversion and fake electrons are a background source of electrons that need to be greatly reduced: this is accomplished by placing quality requirements (*cuts*) on the electron candidates. The variables that help distinguish prompt electrons from fake and non-prompt electrons are:

- $\Delta\eta_{\mathrm{in}}$ and $\Delta\phi_{\mathrm{in}}$: The difference in η and ϕ between the track position at the ECAL extrapolated from innermost track state, and the η and ϕ of the SC. A large difference would indicate a fake electron.

Table 4.1: List of cuts used to reduce fake and non-prompt electrons. Values listed are upper bounds.

Variable	EB	EE
$\lvert\Delta\eta_{\text{in}}\rvert$	0.004	0.007
$\lvert\Delta\phi_{\text{in}}\rvert$	0.06	0.03
H/E	0.04	0.15
$\sigma_{i\eta i\eta}$	0.01	0.03
$\lvert d_0\rvert$	0.02 cm	0.02 cm
$\lvert d_z\rvert$	1.0 cm	1.0 cm
$I^{\text{comb}}/p_{\text{T,lepton}}$	0.07	0.06

- H/E: The ratio of the hadronic energy in a cone of radius $\Delta R < 0.1$ around electron position in the calorimeter to the electromagnetic energy of the SC. This variable provides useful discrimination between electrons and jets, as electrons deposit little energy (if any) in the hadronic calorimeter, unlike most jets.

- $\sigma_{i\eta i\eta}$: A measure of the η spread of the electron's energy deposit in the 5×5 block centered on the ECAL seed crystal. A large spread in the energy deposition by the electron candidate indicates that the candidate was most likely a jet.

- Impact parameters: An impact parameter is the distance of closest approach of the electron trajectory to a certain point. The two impact parameters we use are d_0, measured in the transverse plane with respect to the beam spot, and d_z, measured along the beam direction with respect to the primary vertex.

- $I^{\text{comb}}/p_{\text{T,lepton}}$: Combined relative isolation. I^{comb} is the sum of the transverse energy E_{T} (as measured in the electromagnetic and hadron calorimeters) and the transverse momentum p_{T} (as measured in the silicon tracker) of all reconstructed objects within a cone of $\Delta R < 0.3$ around the electron direction, excluding the electron.

Table 4.1 lists the requirements on these quantities. Conversion electrons are rejected by requiring that:

- There are no hits that are expected but missing in the inner tracker.
- The distance between possible conversion tracks is at least 0.02 cm.
- $\Delta(\cot\theta)$ between possible conversion tracks at the conversion vertex is at least 0.02.

Additionally, the electron must satisfy $\Delta R > 0.3$ with respect to all jets with $p_{\mathrm{T}} > 40$ GeV and $|\eta| < 2.4$. This is used to distinguish jets from electrons.

4.2 Muons

Muon reconstruction [16] involves the inner tracker, combined with the muon system (DT, CSC, RPC). This was discussed in some detail in Chapter 3. Track reconstruction in the muon system makes use of the track hits and track segments (set of aligned hits) from the muon subdetectors. The algorithm starts from a locally-reconstructed muon track segment in one of the innermost detector stations; it is used as a seed for a Kalman filter which builds trajectories going radially outward. A χ^2 cut rejects hits unlikely to be associated with the track. The trajectory is propagated using a detailed map of the magnetic field and taking account of energy loss in the detector material (mainly the steel of the magnet return yoke), until the outermost detector layer of the muon system is reached. An outside-in Kalman filter is then applied, and the track parameters are defined at the innermost muon station. Finally, the track is extrapolated to the nominal interaction point and a vertex-constrained fit to the track parameters is performed. The muons used in this analysis are reconstructed by combining fitted trajectories in the silicon tracker and the muon chambers (*global* muons). Muons are reconstructed over the range $|\eta| < 2.4$, but we only use muons with $|\eta| < 2.1$ in this analysis.

Muon reconstruction is easier than electron reconstruction in many ways. Muons are minimum ionizing particles, so they are much less prone to ionizing or exciting atoms/ molecules in material that they encounter. They are also much less susceptible to Bremsstrahlung than electrons. This is because the total power radiated by a particle in this situation is proportional to γ^4 (γ is the Lorentz factor), and for the same energy, the more massive a particle, the smaller its Lorentz factor ($E = \gamma mc^2$). Because of the muon chambers, a high p_{T} muon track consists of about 30 hits, compared only 10 hits for a high p_{T} electron track, so muon tracks have better p_{T} resolution.

Like electrons, muons suffer from background in the form of non-prompt and fake muons. The nature of fake muons is different from that of fake electrons: they are hadronized quark jets that penetrate through the HCAL (the *punch-through* effect). The HCAL, and especially the HO, is designed to prevent this from happening: the total depth of the calorimeter system is a minimum of 11.8 interaction lengths, where one interaction length reduces the number of particles by $1/e$. However, not all jets can be stopped. For a fixed lepton efficiency, reducing muon backgrounds is easier than reducing electron backgrounds, since punch-through muons are rarer than fake electrons. A number of quality cuts are applied to reject fake and non-prompt muons. Muon candidates must have:

- a χ^2 per degree of freedom (of the global fit) less than 10, and at least one muon chamber hit used in the fit (*GlobalMuonPromptTight*);
- at least 11 hits in the inner tracker (with at least one hit in the pixel system) and 2 matched segments in the muon system;
- an uncertainty in the fitted inverse transverse momentum of $\sigma(p_{\mathrm{T}})/{p_{\mathrm{T}}}^2 < 0.001$ GeV^{-1};
- $I^{\mathrm{comb}}/p_{\mathrm{T,lepton}} < 0.1$.

In addition, the candidates must pass the same impact parameter cuts as electrons, and qualify as a tracker muon. Finally, like electrons, muons must satisfy $\Delta R > 0.3$ with respect to all jets with $p_{\mathrm{T}} > 40$ GeV and $|\eta| < 2.4$.

4.3 Jet reconstruction using the Particle-Flow algorithm

Jets [17, 18] used in this analysis are reconstructed based on the PF algorithm. We describe the PF algorithm in Sec. 4.3.1, and then state the requirements that a jet must satisfy in Sec. 4.3.2.

4.3.1 The Particle-Flow Algorithm

The PF technique reconstructs and identifies all stable particles in an event: muons, electrons, photons, and charged and neutral hadrons. This list of individual particles is then used to build jets, and to determine the missing transverse momentum. We focus our discussion on the reconstruction of charged hadrons, neutral hadrons and photons, which are the basic constituents of jets. The flow of the discussion, which can be found in greater detail elsewhere [19, 20], mirrors that of the PF algorithm. The reconstruction of the algorithm's *fundamental elements*, the charged-particle tracks and the calorimetric clusters, is described in Sec. 4.3.1.1. These elements are then topologically linked into *blocks*, as explained in Sec. 4.3.1.2. Section 4.3.1.3 explains how blocks are interpreted as stable particles.

4.3.1.1 Fundamental elements

Stable particles created during collisions usually carry low momenta; for example, in a 500 GeV jet, constituent particles have an average p_{T} of around 10 GeV, and for softer jets around 100 GeV (which are more typical in the decay of heavy exotic particles), the average p_{T} of constituents is a few GeV. As already mentioned, particle reconstruction and identification uses charged-particle tracks, calorimeter clusters, and muon tracks. Hence, these elements need to be delivered with a high efficiency and a low *fake rate*, even in high-density environments. For tracking, fake rate is the probability that hits in the tracker that do not pertain to a real particle (e.g. noise) are misreconstructed as a track. Similarly, for clustering, fake rate is the probability that deposits in the calorimeter not associated with a real particle are misreconstructed as a cluster. The tracking and clustering algorithms used to reconstruct the fundamental elements are briefly presented below.

Charged Particle Tracking: For charged hadrons with p_{T} up to a few hundred GeV, the tracker has a better momentum resolution than the calorimeter. It also provides a precise measurement of the charged-particle direction at the production vertex, before the magnetic field has deviated the particle. Since about two-thirds of the energy of a jet is carried by charged particles, the tracker is the crucial part of the PF event reconstruction. If a charged hadron is missed by the tracker, the only chance it has of being detected is by the calorimeter, which is undesirable for the reasons just mentioned; thus, the tracking efficiency needs to be almost 100%. On the other hand, the tracking fake rate has to be kept small because fake tracks, with randomly distributed momenta, could lead to potentially large fake missing transverse momentum.

An iterative-tracking strategy [21] is used to achieve high efficiency while maintaining a low fake rate. For each iteration, the following steps are applied:

- In the first iteration, the complete set of reconstructed hits is available for reconstructing tracks. In subsequent iterations, hits associated with a *highPurity* track and passing a χ^2 cut are removed.
- Seed finding is performed on the available hits. The seeding configuration (in terms of which tracker layers are used, and what requirements are placed on the hits that constitute the seed) is the main difference between iterative steps.
- Track reconstruction (building, filtering, fitting, smoothing) is performed using the available hits. Parameters can be tuned separately for each iteration to improve performance.
- The track collection is cleaned (i.e. quality criteria are applied to it), and the collection of tracks which pass the cleaning stage is stored.

After three iterations, tracks originating from within a thin cylinder around the beam axis have a reconstruction efficiency of 99.5% for isolated muons in the tracker acceptance, and larger than 90% for charged hadrons in jets. The fourth and fifth iterations relax the constraints on the origin vertex, which allows the reconstruction of secondary charged particles originating from photon conversions and nuclear interactions in the tracker material, and from the decay of long-lived particles. Charged particles with as few as three hits, a p_{T} as small as 150 MeV, and an origin vertex more than 50 cm away from the beam axis, are reconstructed with a fake rate of about 1%.

Calorimeter Clustering: There are four main uses for calorimeter clustering:

- measure the energy and direction of stable neutral particles such as photons and neutral hadrons;
- distinguish these neutral particles from the energy deposits from charged hadrons;
- reconstruct and identify electrons and all accompanying Bremsstrahlung photons;

- help the energy measurement of charged hadrons for which the track parameters were not determined accurately i.e. low-quality or high-p_{T} tracks.

The clustering algorithm has a high detection efficiency even for low-energy particles, and can separate close energy deposits. The clustering is performed separately in each sub-detector: EB, EE, HB, HE, ES layer 1, and ES layer 2. In the HF, no clustering is performed so far, so that each cell gives rise to one cluster. The algorithm consists of three steps:

- *cluster seeds* are identified as local calorimeter cell energy maxima above a certain threshold;
- *topological clusters* are grown from the cluster seeds by aggregating cells with at least one side in common with a cell already in the cluster, and with an energy in excess of two standard deviations of the electronics noise: 80 MeV in EB, up to 300 MeV in EE, and 800 MeV in the HCAL;
- a topological cluster gives rise to as many particle-flow clusters as cluster seeds. So if a topological cluster has two cluster seeds, it will result in two PF clusters. The energy and position of each PF cluster is determined using an iterative procedure. In the first iteration, the PF cluster position is simply that of the seeding cell. The energy of each cell in the topological cluster is shared between all PF clusters based on the cell-cluster distance. At the next iteration, the position of each PF cluster is recomputed as the mean position of the central cells in the PF Cluster, weighted by the logarithm of the cell energies. The energies of the PF clusters are determined again with these new positions. The procedure is repeated until PF cluster positions do not move by more than a small fraction of the position resolution.

4.3.1.2 Linking elements to form blocks

A given particle is likely to give rise to several fundamental elements in the various CMS sub-detectors: a charged-particle track, and/or several calorimeter clusters, and/or a muon track. To reconstruct this particle, the different elements must be linked together. The *distance* between any two elements, as defined by the link algorithm, quantifies the quality of the link between them. The linked blocks, which typically contain up to three elements, serve as simple inputs for particle reconstruction and identification.

To establish a link between a charged-particle track and an ECAL cluster, the track is extrapolated from its last measured hit in the tracker to the ECAL. The track is linked to any given cluster if the extrapolated position in the ECAL is within the cluster boundaries. The link distance is defined as the distance in the (η, ϕ) plane between the extrapolated track position and the cluster position. The same approach works for clusters in the ES and HCAL.

To collect the energy of Bremsstrahlung photons emitted by electrons, tangents to the tracks are extrapolated to the ECAL from the intersection points between the track and each of the tracker layers. A cluster is linked to the track as a potential Bremsstrahlung photon if the extrapolated tangent position is within the boundaries of the cluster.

A link between two calorimeter clusters i.e. either between an HCAL and an ECAL cluster, or between an ECAL and a ES cluster, is established when the cluster position in the more granular calorimeter (ES or ECAL) is within the cluster envelope in the less granular calorimeter (ECAL or HCAL). The link distance is defined in the same way as for a track and a calorimeter cluster.

Finally, a link between a charged-particle track in the tracker and a muon track in the muon system is established when a global fit between the two tracks returns an

acceptable χ^2, which defines the link distance. When several global muons can be fit with a given muon track and several tracker tracks, only the global muon that returns the smallest χ^2 is retained.

4.3.1.3 Reconstructing and identifying particles

Initially, blocks may contain contributions from multiple particles, and the final step is to tease these apart into the individual contributions. The idea to separate the individual particles, removing them from the block one by one until nothing is left and all clusters and tracks are accounted for. For each block, the final step of the algorithm, which reconstructs and identifies particles, proceeds as follows. First, a global muon becomes a *particle-flow muon* if its combined momentum is compatible with the tracker-only momentum within three standard deviations. The corresponding track is removed from the block. The energy deposited in the HCAL (ECAL), used at a later stage in the algorithm, is estimated to be 3 (0.5) GeV (measured using cosmic rays), with an uncertainty of ± 100%. Electron reconstruction and identification follows. Identification is performed using a number of tracking and calorimetric variables, similar to what was discussed in Sec. 4.1. Each identified electron gives rise to a *particle-flow electron*. The corresponding track and ECAL clusters (including all ECAL clusters identified as Bremsstrahlung photons) are removed from further processing of the block.

Tighter quality criteria are applied to the remaining tracks in the block: if the relative uncertainty in the measured p_{T} is larger than the relative calorimetric energy resolution expected for charged hadrons, the track is removed from the block. In jets, this requirement rejects 0.2% of the tracks. While about 90% of these are fake tracks, the energy of the remaining 10% (originating from real particles) is not lost, as it is measured independently by the calorimeters.

The remaining elements of the block may give rise to charged hadrons, neutral particles (photons or neutral hadrons), and more rarely to additional muons. Which of these particles gets identified is based on a comparison between the energy detected in the calorimeters (corrected for muons in the block) and the momentum of the linked track(s). A track can be connected to multiple ECAL and HCAL clusters, in which case only the link to the closest cluster is kept; it is also possible for several tracks to be linked to the same HCAL cluster, in which case the sum of their momenta is compared to the HCAL energy. In any case, particles are removed from the block as they are identified.

In rare cases, the total calorimetric energy is significantly smaller than the total track momentum. If the difference is larger than three standard deviations, a relaxed search for muons and fake tracks is performed. First, all global muons not already selected by the algorithm, and for which the momentum is known with at least 25% precision, are treated as PF muons and removed from the block. Then, tracks with large p_{T} uncertainty are removed from the block on the assumption that they are fake (no energy is subtracted from the calorimeters); this removal process stops when all tracks with a p_{T} uncertainty above 1 GeV have been eliminated, or when the removal of a track would make the total track momentum smaller than the calorimetric energy. Less than 0.03% of real tracks are dropped by this procedure.

Each of the remaining tracks in the block gives rise to a *particle-flow charged hadron*, the momentum and energy of which are taken directly from the track momentum, under the charged pion mass hypothesis. If the calorimetric energy is compatible with the track momentum within measurements uncertainties, the charged-hadron momenta are redefined by a fit of the measurements in the tracker and the calorimeters, which reduces to a weighted average if only one track is present. This combination is relevant at very high energies and/or large η, where the track parameters have poorer

resolutions.

On the other hand, it may well be the case that the energy of the closest ECAL and HCAL clusters linked to the track(s) is significantly larger than the total associated charged-particle momentum. If the relative energy excess is found to be larger than the expected calorimeter energy resolution (corrected for muons in the block), it gives rise to a *particle-flow photon*, and possibly to a *particle-flow neutral hadron*. Specifically, if the excess is larger than the total ECAL energy, a photon is created with this ECAL energy and a neutral-hadron is created with the remaining part of the excess. Otherwise, the excess gives rise only to a photon. The precedence given in the ECAL to photons over neutral hadrons is justified by the observation that, in jets, 25% of the jet energy is carried by photons, while neutral hadrons leave only 3% of the jet energy in the ECAL.

ECAL and HCAL clusters that are not linked to tracks give rise to PF photons and PF neutral hadrons, respectively.

4.3.2 Jets

The typical jet energy fractions carried by charged particles, photons, and neutral hadrons are 65%, 25%, and 10%, respectively. This means that 90% of the jet energy (the fraction from charged particles and photons) can be reconstructed with good precision by the PF algorithm, both in magnitude and direction; only the remaining 10% of the energy (the fraction from neutral hadrons) is affected by the poor HCAL resolution, and by calibration corrections of about 10 to 20% (a source of uncertainty that that ECAL does not suffer from). Consequently, jets made of reconstructed particles are much closer to jets made of generated particles than jets reconstructed using only calorimeter information, in energy, direction, and content.

Jet clustering is performed using the anti-k_T [22] clustering algorithm. Particles reconstructed with the PF algorithm (as explained in Sec. 4.3.1.3) that are above a certain energy threshold and within a ΔR cone of 0.5 are clustered into PF jets. All PF jets below 10 GeV are considered to represent unclustered energy. Applied jet energy corrections include: offset (L1FastJet [23] with active area calculation), relative (L2), and absolute (L3). The purpose of the offset term is to correct for pile-up; the relative corrections smooth out any η dependence, and the absolute corrections relate to the overall energy scale. Additionally, jets in data have residual corrections applied to them to account for data-simulation discrepancies, since the other corrections are based on simulation. Jet candidates are required to satisfy loose quality criteria that suppress noise and spurious energy deposits:

- at least two particles (at least one of them charged) in the jet;
- energy fraction of neutral hadrons < 0.99;
- both charged and neutral electromagnetic energy fractions < 0.99.

Jets must have $p_T > 40$ GeV and $|\eta| < 2.4$. We form $H_T = \sum p_T$, where the sum is taken over all jets passing the selection just described.

4.4 Missing Transverse Momentum

We define $\overrightarrow{\not{E}_T} = -\sum \vec{p}_T$, where the sum is over PF objects reconstructed offline, and $\not{E}_T = |\overrightarrow{\not{E}_T}|$. In CMS, the $\not{E}_T$ used by us is referred to as *uncorrected PFMET*. An alternative is to use *type-I corrected PFMET*, a propagation of the jet energy corrections to $\not{E}_T$. However, there are no existing studies showing that the use of type-I corrected PFMET provides any benefit, hence we use uncorrected PFMET.

4.5 Conclusion

In this chapter, we saw how the signals from the CMS detector can be used to reconstruct final state particles to be used for a physics analysis. As mentioned, the PF technique is used for reconstructing jets and $\not\!\!E_{\mathrm{T}}$. This is because it has been established that PF reconstruction performs better for these objects that purely calorimeter-based reconstruction. For leptons, there are no studies yet that show that PF electrons and PF muons have better performance for a SUSY search when compared to the conventional reconstruction approach described in Sec. 4.1 and Sec. 4.2, respectively. When (and if) this happens, PF event reconstruction will be used for all physics objects.

CHAPTER 5

DATA AND SIMULATION

This analysis uses pp collisions at $\sqrt{s} = 7$ TeV recorded by the CMS experiment in 2011. In Sec. 5.1, we discuss the physics processes that typically emerge from LHC collisions. In Sec. 5.2, we describe how we sift through the data to find events more likely to have the final state relevant to this analysis. In Sec. 5.3, we discuss the simulated physics processes used to model the data and develop our search strategy. The initial offline event selection (*preselection*), which is applied to both the data and the simulation, is discussed in Sec. 5.4.

5.1 Physics processes at the LHC

Figure 5.1 shows the production cross section at a hadron collider for several physics processes as a function of center-of-mass energy. The total cross section ($\sigma_{\text{tot}} \sim 100$ mb) is comprised of elastic (~ 30 mb) and inelastic (~ 70 mb) collisions. Elastic collisions are of no interest to particle physics. The vast majority of inelastic collisions results in QCD events (which include bottom quark pair production, σ_b, and the production of energetic jets, σ_{jet}), where the production process only involves the strong force, leading to a final state with jets. As mentioned in Chapter 3, for an instantaneous luminosity of 10^{34} cm^{-2} s^{-1}, the event rate at the LHC is $\sim 10^9$ Hz (with electroweak processes having a rate of $\sim 10^3$ Hz), whereas events can only be stored at $\sim 10^2$ Hz. So when we study stored events, we have to keep in mind that there are far more events that have been rejected for not having enough energetic jets and/or leptons to make them interesting. When presenting differential cross sections, the data has to be transformed to the underlying true distribution so as to account for selection effects (*unfolding*).

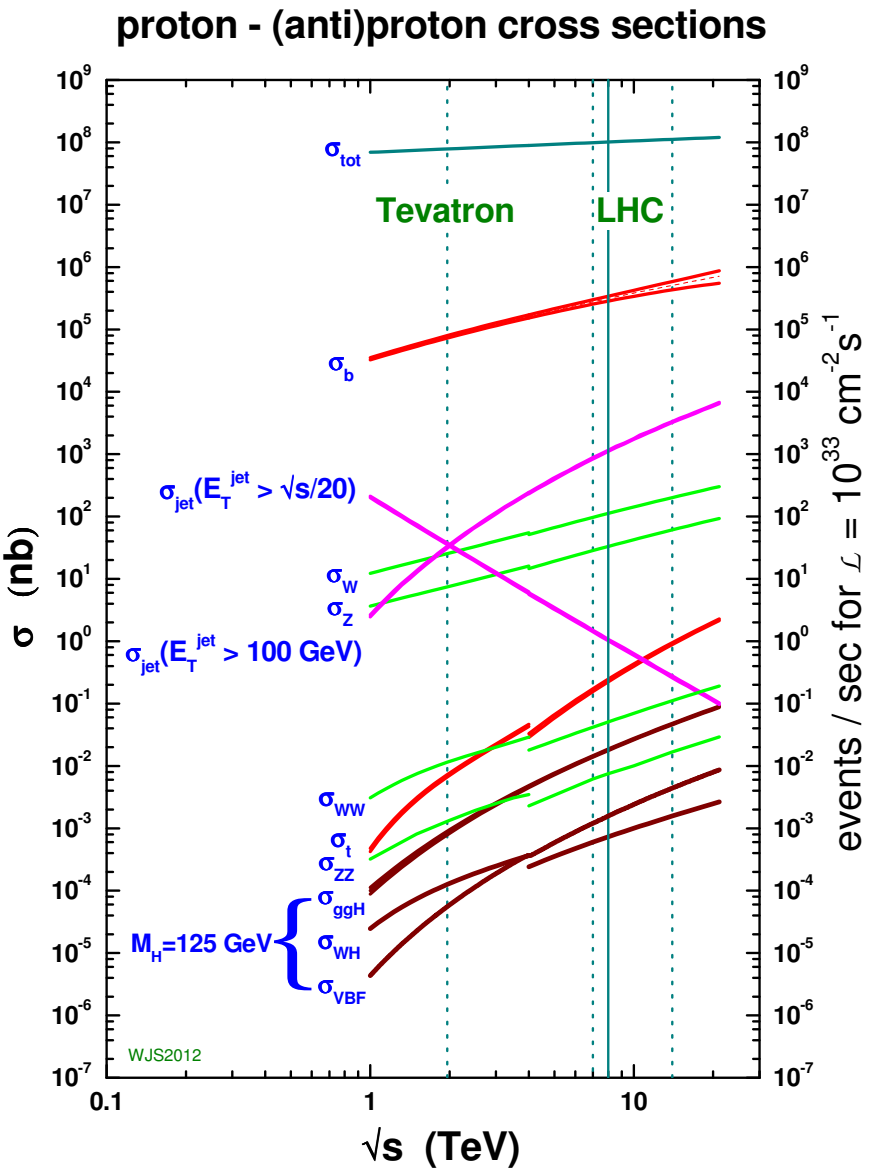

Figure 5.1: Production cross section of physics processes versus center-of-mass energy. The axis on the right shows the event rate [24].

5.1.1 QCD processes

In leading-order (LO) perturbative QCD, jet production in pp collisions occurs when two partons interact via the strong force to produce two final state particles. The elementary processes which contribute in this are: $qq \rightarrow qq$, $qg \rightarrow qg$, $gg \rightarrow gg$, and $gg \rightarrow qq$. Each of the final state particles will further lose energy by emitting other quarks and gluons in a parton shower. Finally, the products of the parton shower undergo hadronization to form hadron jets.

The events selected by minimum bias triggers[1] involve predominantly soft interactions, and contain mostly particles with low transverse momenta. The charged particle multiplicity n is obtained by counting all charged particles produced by the primary interaction and is a basic observable in hadron collisions. In order to understand the dynamics of hadron production, CMS performed an inclusive measurement of charged particle multiplicities, the results of which can be seen in Fig. 5.2.

The inclusive jet production cross section is very large, and is therefore one of the first measurements CMS was able to make. The differential cross section, as a function of jet p_{T}, can be seen in Fig. 5.3. Low p_{T} jets are recorded with a prescaled[2] minimum bias trigger, and the measurement is extended to high p_{T} using single-jet triggers.

The ratio of the inclusive 3-jet to 2-jet cross sections (R_{32}) provides information about the strong coupling constant α_S and its evolution as a function of the square of the momentum transferred in the collision. Production of events with three or more jets in the final state originate from gluon radiation and other higher order QCD processes. Fig. 5.4 shows R_{32} as a function of H_{T}.

[1] which select non-single diffractive inelastic collisions

[2] if a trigger has a prescale value of x, it means only 1 out of x triggered events are stored

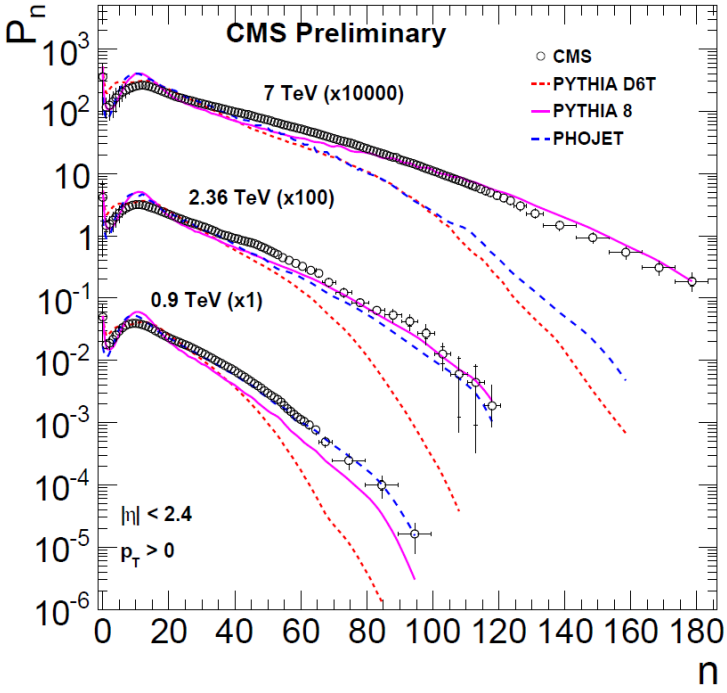

Figure 5.2: The charged particle multiplicity distributions compared between data and simulation [25].

5.1.2 Electroweak processes

The ability to produce leptons distinguishes electroweak processes from QCD. Among electroweak processes, W boson production has the largest cross section (σ_W), which is about six orders of magnitude smaller than σ_{tot}. The decay of the W boson has been shown previously (Fig. 2.3). Z boson decays are topologically very similar to W boson decays, though Z bosons have a production cross section (σ_Z) that is an order of magnitude smaller than σ_W. Both W and Z bosons are produced in association with jets. The study of associated jet production provides a stringent test of perturbative QCD calculations. Next-to-leading order (NLO) predictions are available for $V + n$ jets, with n up to four for the W and three for the Z, but are only known with a precision varying from 10% up to 30% due to theoretical uncertainties. The exclusive jet multiplicity for W+jets can be seen in Fig. 5.5; Fig. 5.6 shows the same for Z+jets.

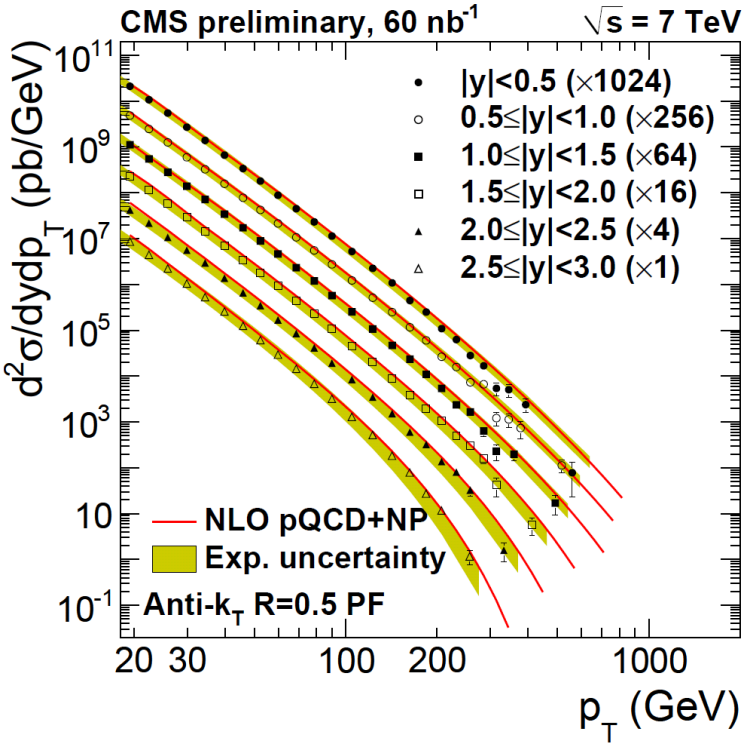

Figure 5.3: Comparison between the unfolded measured spectra and the theory predictions for particle-flow jets. For better visibility the spectra are multiplied by arbitrary factors, indicated in the legend [26].

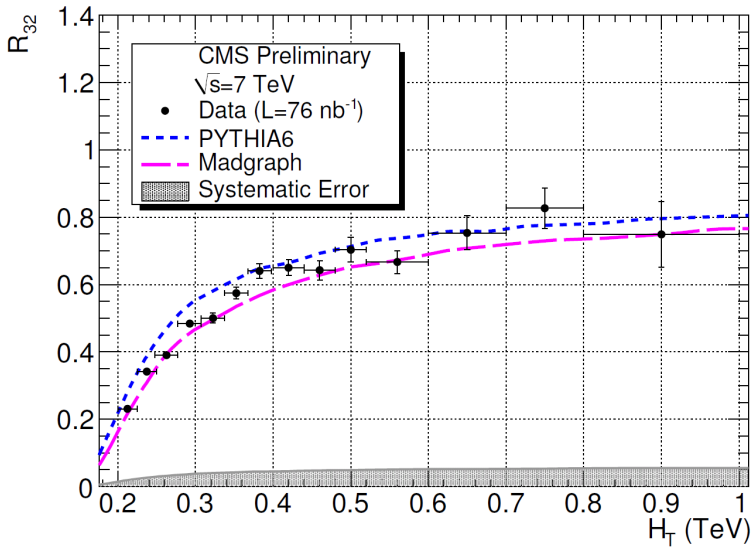

Figure 5.4: The ratio R_{32} at hadron level from data (solid circles) compared with PYTHIA (dashed line) and Madgraph (solid line). The shaded area indicates the size of the systematic error [27].

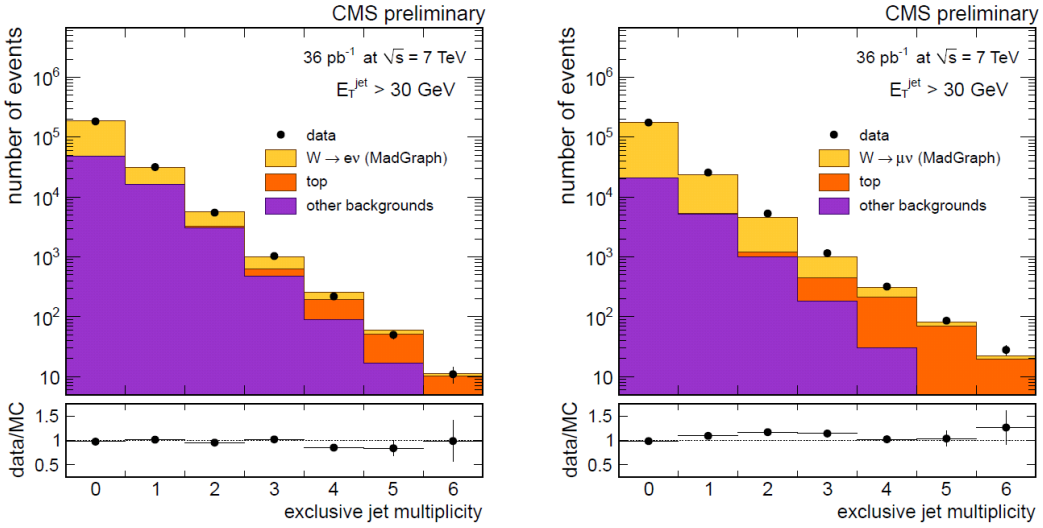

Figure 5.5: Exclusive number of reconstructed jets in W+jets events in the electron (left) and muon (right) channels [28].

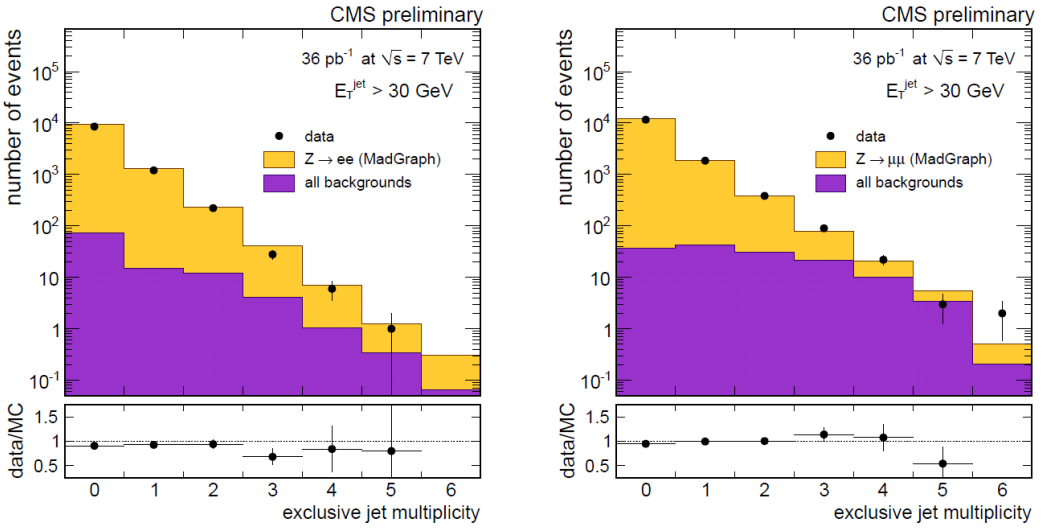

Figure 5.6: Exclusive number of reconstructed jets in Z+jets events in the electron (left) and muon (right) channels [28].

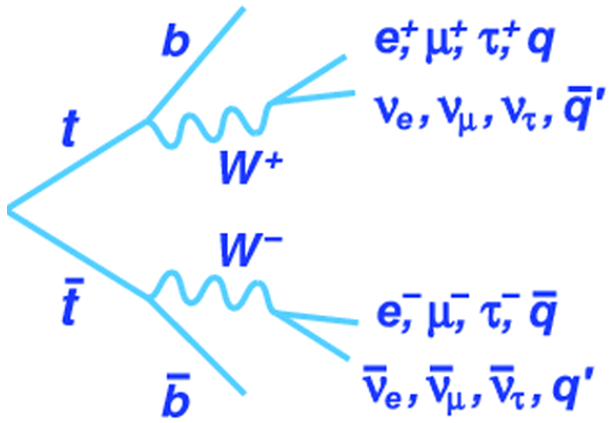

Figure 5.7: Feynman diagram of the decay of a top quark pair [29].

The cross section for top quark pair production (σ_t) is about three orders of magnitude smaller than σ_W, though when looking at final states with multiple jets, $t\bar{t}$ decays can be as important as W boson decays, as demonstrated by Fig. 5.5. The decay of $t\bar{t}$ is shown in Fig. 5.7. The decay can be hadronic (both W bosons decay hadronically), semi-leptonic (one of the W bosons decays leptonically), or dileptonic (both W bosons decay leptonically). Single top quark decays look like the top half of Fig. 5.7, though the single top quark production cross section is almost an order of magnitude smaller than σ_t.

5.2 Data

The data used for this analysis corresponds to an integrated luminosity of 4.98 fb^{-1}. The data-taking, which lasted from March to October, had a three week stop in July for machine development. Data taken prior to this is part of Run 2011A, whereas data taken after this is part of Run 2011B. During 2011, the instantaneous luminosity incrementally rose from 5×10^{32} to 5×10^{33} cm^{-2} s^{-1}. The HLT paths used to select the events of interest are discussed in Sec. 5.2.1, and the datasets that were processed are mentioned

in Sec. 5.2.2.

5.2.1 High Level Trigger Paths

HLT paths are *seeded* by L1T paths, meaning the algorithm for a certain HLT path is only deployed if the L1T path associated with it has *fired*. To fire a trigger path, an event must contain certain physics objects (e.g. two jets or one muon) above certain p_{T} thresholds. In general, a HLT path is seeded by a L1T path that requires the same physics objects. The p_{T} thresholds applied at the HLT are slightly higher than the p_{T} thresholds at the L1T, since the energy estimates at the L1T are coarser than the energy estimates at the HLT. This ensures that the HLT p_{T} requirement is fully efficient.

QCD events need to be drastically reduced is at the trigger level. As mentioned before, events can only be stored at $\sim$ 100 Hz (determined by the HLT), so if QCD is not controlled, then the signal events will simply be lost. This is done by requiring (i) multiple jets, or (ii) very high H_{T} (several hundred GeV), or (iii) substantial $\not{E}_{\mathrm{T}}$ (tens of GeV), or (iv) one or more isolated leptons, or (v) some restriction on a cleverly constructed variable, or (vi) some combination of the above. The exact strategy adopted depends on the signal and the final state. For example, if the signal typically has a very energetic leading jet, then requiring that all events have a jet with $E_{\mathrm{T}} > 100$ GeV can make a big dent in QCD, since the cross section of such events is only an order of magnitude larger than σ_W. In all cases, a balance has to be maintained between signal efficiency (the fraction of the signal surviving the selection) and signal purity (the ratio of signal events to total events). The final state signature for this analysis consists of a single isolated lepton (electron or muon), three or more energetic jets, and large $\not{E}_{\mathrm{T}}$.

During Run 2011A, the trigger was based on leptons and jets, with requirements

Table 5.1: List of HLT paths used for this analysis. Mu/Ele refer to the p_T of the lepton, HT refers to $H_T^{trigger}$, PFMHT refers to $\not{E}_T{}^{trigger}$, and v* indicates that many versions of the trigger were deployed.

Muon trigger paths
Mu8_HT200_v*
Mu15_HT200_v*
HT250_Mu15_PFMHT20_v*
HT250_Mu15_PFMHT40_v*
HT300_Mu15_PFMHT40_v*
Electron trigger paths
Ele10_CaloIdL_CaloIsoVL_TrkIdVL_TrkIsoVL_HT200_v*
Ele15_CaloIdT_CaloIsoVL_TrkIdT_TrkIsoVL_HT200_v*
Ele15_CaloIdT_CaloIsoVL_TrkIdT_TrkIsoVL_HT250_v*
Ele15_CaloIdT_CaloIsoVL_TrkIdT_TrkIsoVL_HT250_PFMHT25_v*
Ele15_CaloIdT_CaloIsoVL_TrkIdT_TrkIsoVL_HT250_PFMHT40_v*

applied to lepton p_T and the total transverse energy deposited in jets, $H_T^{trigger}$. With rising instantaneous luminosity (Run 2011B), to keep the trigger rate at the assigned level, a requirement was made on the missing transverse momentum, $\not{E}_T{}^{trigger}$, reconstructed using the PF algorithm. We define $\not{E}_T{}^{trigger} = |-\sum \vec{p_T}|$, where the sum is over PF objects reconstructed at the HLT. Table 5.1 lists all the triggers used in this analysis, showing the evolution of the thresholds applied. The final thresholds applied on these quantities were: lepton $p_T > 15$ GeV, $H_T^{trigger} > 300$ GeV (250 GeV for the electron trigger), and $\not{E}_T{}^{trigger} > 40$ GeV. For the electron triggers, in order to keep QCD contamination (and hence the trigger rates) at sustainable levels, quality requirements were made on the electron's calorimeter deposit parameters, calorimeter isolation, track parameters, and track isolation. Depending on the cuts used, these requirements can be classified as very loose (VL), loose (L), and tight (T).

Table 5.2: Certification files and primary datasets used for the muon and electron channels, together with the run ranges and integrated luminosities.

Datasets	Run Range	$\int \mathcal{L}\, dt$
Certification: `Cert_160404-163869_7TeV_May10ReReco_Collisions11 (v2)`		
`/MuHad/Run2011A-May10ReReco-v3` `/ElectronHad/Run2011A-May10ReReco-v1`	160329 – 163869	0.22 fb^{-1}
Certification: `Cert_160404-176309_7TeV_PromptReco_Collisions11`		
`/MuHad/Run2011A-PromptReco-v4` `/ElectronHad/Run2011A-PromptReco-v4`	165071 – 168437	0.93 fb^{-1}
Certification: `Cert_160404-172619_7TeV_ReReco5Aug_Collisions11 (v2)`		
`/MuHad/Run2011A-Aug5ReReco-v3` `/ElectronHad/Run2011A-Aug5ReReco-v1`	170053 – 172619	0.37 fb^{-1}
Certification: `Cert_160404-176309_7TeV_PromptReco_Collisions11`		
`/MuHad/Run2011A-PromptReco-v6` `/ElectronHad/Run2011A-PromptReco-v6`	172620 – 175770	0.66 fb^{-1}
Certification: `Cert_160404-180252_7TeV_PromptReco_Collisions11`		
`/MuHad/Run2011B-PromptReco-v1` `/ElectronHad/Run2011B-PromptReco-v1`	175832 – 180252	2.50 fb^{-1}

5.2.2 Datasets

Data certified as *golden* by the CMS Data Quality Monitoring certification team are used in analysis. Table 5.2 summarizes the certification files, dataset names and run ranges.

5.3 Simulation

The analysis makes use of samples of events taking place in a GEANT4-based simulation [30] of the CMS detector. QCD multijet events are produced using the PYTHIA 6.4.22 [31] event generator with the Z2 tune; $t\bar{t}$, W+jets, Z+jets samples are generated using MADGRAPH [32], and single top quark events are produced using POWHEG [33]. SUSY signal samples are generated using PYTHIA. The simulated samples are part of the CMS *Summer11* central production. Table 5.3 summarizes the simulated datasets used. The simulated samples are analyzed using the same reconstruction software as used for

the data.

5.3.1 Cross sections for simulated processes

For the background physics processes, the cross sections have been measured experimentally, and their difference from the theoretical values gives us an estimate of the related uncertainty. However, for SUSY processes, the experimental cross sections have yet to be determined, so it is important to get a measure of the uncertainty associated with the theoretical cross sections. To do this, we need to study the dependence of the cross sections on certain key inputs. This issue will be revisited in Chapter 7, but for now, it is important to introduce certain concepts that affect cross section calculations: (i) parton distribution functions (PDFs), (ii) factorization scale, and (iii) renormalization scale.

A proton is composed of two up quarks and one down quark (referred to as valence quarks). This model of three free non-interacting valence quarks cannot match observations from inelastic scattering. The valence quarks are embedded in a sea of virtual quark-antiquark pairs generated by the gluons which hold the quarks together in the proton. All of these particles (valence quarks, sea quarks and gluons) are partons. A PDF is defined as the probability density for finding a particle with a certain longitudinal momentum fraction x at momentum transfer Q^2. Fig. 5.8 shows the PDFs at Q = 2 GeV and Q = 100 GeV. In hadron collisions, the parton spectrum is not fixed, and is given by the PDF. The cross section for an initial state ending up in a certain final state depends on the PDF and the probability for these partons to scatter into the required final state, which is calculated from the Feynman diagrams.

PDFs cannot be obtained from lattice QCD calculations due to current computation

Table 5.3: Simulated event samples used in this analysis.

SM samples
/TTJets_TuneZ2_7TeV-madgraph-tauola/Summer11-PU_S4_START42_V11-v1
/WJetsToLNu_TuneZ2_7TeV-madgraph-tauola/Summer11-PU_S4_START42_V11-v1
/WJetsToLNu_300_HT_inf_TuneZ2_7TeV-madgraph-tauola/Summer11-PU_S4_START42_V11-v1
/DYJetsToLL_TuneZ2_M-50_7TeV-madgraph-tauola/Summer11-PU_S4_START42_V11-v1
/Tbar_TuneZ2_tW-channel-DR_7TeV-powheg-tauola/Summer11-PU_S4_START42_V11-v1
/Tbar_TuneZ2_s-channel_7TeV-powheg-tauola/Summer11-PU_S4_START42_V11-v1
/Tbar_TuneZ2_t-channel_7TeV-powheg-tauola/Summer11-PU_S4_START42_V11-v1
/T_TuneZ2_tW-channel-DR_7TeV-powheg-tauola/Summer11-PU_S4_START42_V11-v1
/T_TuneZ2_t-channel_7TeV-powheg-tauola/Summer11-PU_S4_START42_V11-v1
/T_TuneZ2_s-channel_7TeV-powheg-tauola/Summer11-PU_S4_START42_V11-v1
/QCD_Pt-*_TuneZ2_7TeV-pythia6/Summer11-PU_S3_START42_V11-v2
/QCD_Pt-*_MuPt5Enriched_TuneZ2_7TeV-pythia6/Summer11-PU_S*_START42_V11-v*
/QCD_Pt-*_EMEnriched_TuneZ2_7TeV-pythia6/Summer11-PU_S4_START42_V11-v1
/QCD_Pt-*_BCtoE_TuneZ2_7TeV-pythia6/Summer11-PU_S4_START42_V11-v1
SUSY samples
/LM*_SUSY_sftsht_7TeV-pythia6/Summer11-PU_S4_START42_V11-v1
/mSUGRA_m0-220to3000_m12-100to1000_tanb-10andA0-0_7TeV-Pythia6Z/Summer11-PU_START42_V11_FastSim-v2
/SMS-T3w_x-0p25to0p75_Mgluino-100to1200_mLSP-50to1150_7TeV-Pythia6Z/Summer11-PU_START42_V11_FastSim-v2

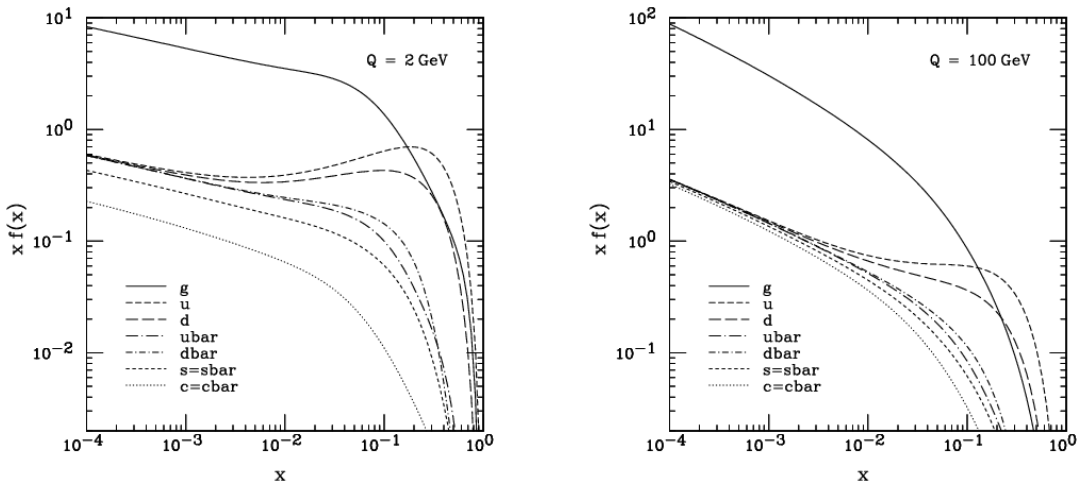

Figure 5.8: CTEQ6M PDFs at Q = 2 GeV (left) and Q = 100 GeV (right) [34].

limitations. They are extracted from a comprehensive global analysis of hard-scattering data from a variety of fixed-target and collider experiments in the framework of perturbative QCD. PDFs are available from various groups: the ones used by the LHC are from CTEQ [35] and MSTW [36]. The groups do not use the same input data. They differ mainly in the way the PDFs are parametrized, in the treatment of heavy quarks, in the value of α_S, as well in the way the experimental errors are treated and the theoretical errors are estimated.

In perturbative QCD calculations, some integrals are divergent. There are two types of divergences: infra-red or IR (low energy), and ultra-violet or UV (high energy). IR divergence happens due to massless particles, like the photon. Every process involving charged particles emits infinitely many coherent photons of infinite wavelength. UV divergence appears in calculations involving Feynman diagrams with closed loops of virtual particles in them. The momentum of the particles in the loop is not uniquely determined by the energies and momenta of incoming and outgoing particles. To find the amplitude for the loop process one must integrate over all possible combinations of energy and momentum that could travel around the loop.

Factorization and renormalization play similar roles at opposite ends of the energy range of perturbative QCD. In factorization, bare parton densities absorb all infrared physics and acquire a factorization scale dependence. In renormalization, the bare strong coupling absorbs all ultraviolet physics and acquires a renormalization scale dependence. These scale parameters are not intrinsic to QCD: they tell us how the factorization/renormalization was implemented.

The dependence of cross section on the renormalization and factorization scales is an artifact of perturbation theory. This is typically reduced as higher-order perturbative contributions are included. Assuming that there is no systematic shift in the cross section from order to order in perturbation theory, for example due to the appearance of new production channels, the range of cross sections covered by the scale dependence at a given loop order should include the true prediction of the cross section. The scale dependence gives us an estimate of the theory uncertainty of the QCD prediction. To estimate the scale uncertainty at the LHC, we vary simultaneously the factorization and renormalization scales within a range of 0.5 to 2 times the reference central scale, which equals the average of the two sparticle masses in the final state.

5.4 Preselection

The goal of preselection is to select an event sample with the broad characteristics of the signal: one isolated lepton, multiple energetic jets, and large $\not{E}_{\mathrm{T}}$. There are two steps to this: data cleaning (Sec. 5.4.1), and preliminary background suppression (Sec. 5.4.2).

5.4.1 Data cleaning

Cleaning refers to the application of *filters* that eliminate events with known detector or reconstruction problems and suppress machine-induced background, including:

- Beam-scraping (*FilterOutScraping*): At least 25% of tracks must pass a quality threshold.
- Problematic primary vertex: The presence of at least one reconstructed primary vertex with at least 4 degrees of freedom and a maximum transverse (longitudinal) distance to the origin of 2 cm (24 cm) is required.
- HCAL noise (*HBHENoiseFilter*): There is GeV – TeV scale noise in the HB and HE, which this filter eliminates. The noise has two main sources: the hybrid photodiodes (HPDs) used to convert the scintillator light into an electrical output, and the readout boxes (RBXs) which contain them.
- ECAL noise: EB and EE have single noisy crystals which are masked during reconstruction. All masked crystals make up only 1% of the total. However, if such masked crystals are located in certain key parts of the ECAL, a significant amount of energy may be lost in that region, leading to fake $\not\!\!E_{\mathrm{T}}$. The *ECALBEFilter* tags events where the boundary energy around a dead 5×5 cluster is above 10 GeV. The *ECALTPFilter* rejects events where the trigger primitive E_{T} at the masked cells exceeds the saturation energy.
- Tracking problems (*trackingFailureFilter*): Rejects misreconstructed events where significant calorimeter deposits contrast with a lack of reconstructed tracks. There are two types of such events: (i) events where the presence of too many tracking clusters makes the tracking algorithm give up on some of its iterations, and (ii) events where the hard collision did not happen in the nominal interaction

point. The filter requires that the Σp_{T} of the tracks belonging to the primary vertex is at least 10% of the H_{T} of all jets in the event.

5.4.2 Preliminary background suppression

While the trigger strongly suppresses QCD events, they need to be reduced further for the analysis, so that the signal significance can be enhanced. The strategy used is similar to what is used online, though the cuts used are tighter. Besides QCD events, electroweak events need to be suppressed as well. The main electroweak backgrounds are W+jets and $t\bar{t}$. The initial suppression consists of:

- The lepton is required to have $p_{\mathrm{T}} > 20$ GeV, which is efficient with respect to the online cut of 15 GeV. Most QCD events do not have a lepton in the final state, and when they do (arising from the leptonic decay of b or c quarks), such leptons are unlikely to be isolated; hence the requirement of a single isolated lepton suppresses QCD greatly.
- Events with additional leptons with $p_{\mathrm{T}} > 15$ GeV are vetoed in order to reduce the overlap between this search and the dilepton search, provide a clearer phenomenological interpretation, and suppress SM backgrounds that produce two or more isolated leptons (e.g. Z+jets, dileptonic $t\bar{t}$). The identification and isolation requirements on the additional leptons are less restrictive than those for the primary electron, and are 90 to 95% efficient over the accepted angular range, to reject dilepton events more effectively.
- Events must contain at least 3 jets. As already mentioned, most QCD events are dijet events, so this requirement eliminates a significant fraction of QCD events.

The W+jets and Z+jets background is significantly suppressed by this requirement as well.

- H_{T} is required to exceed 400 GeV, and $\not\!\!E_{\mathrm{T}}$ to exceed 100 GeV: this makes the event selection highly efficient with respect to the trigger requirements. The $\not\!\!E_{\mathrm{T}}$ requirement heavily suppresses QCD multijet and Z+jets backgrounds, since these events do not have real $\not\!\!E_{\mathrm{T}}$, though there is some fake $\not\!\!E_{\mathrm{T}}$ originating from the mis-measurement of jet momenta.

- Finally, we make a requirement on the transverse mass of the lepton and $\not\!\!E_{\mathrm{T}}$ system, denoted as M_{T} :

$$m_{\mathrm{T}} = \sqrt{(E_{\mathrm{T,lepton}} + \not\!\!E_{\mathrm{T}})^2 - |\overrightarrow{p}_{\mathrm{T,lepton}} + \overrightarrow{\not\!\!E}_{\mathrm{T}}|^2} \; . \tag{5.1}$$

  Backgrounds in which the e or μ and some of the $\not\!\!E_{\mathrm{T}}$ come from a τ decay tend to have small M_{T}. We suppress these events by requiring $M_{\mathrm{T}} > 50$ GeV.

At the end of this step, the SM backgrounds are reduced significantly while retaining high signal efficiency. The proceeding chapters detail how the backgrounds can be reduced even further and estimated using a data-driven technique so that we can find evidence for possible signal.

CHAPTER 6

SEARCHING FOR SUPERSYMMETRY

As previously mentioned, the search for SUSY described in this thesis focuses on events with a single isolated lepton (electron or muon), energetic jets, and large $\not{E}_{\mathrm{T}}$. In SUSY, the single isolated lepton arises from the weak decay of a SUSY particle. The large $\not{E}_{\mathrm{T}}$ comes from particles that do not interact with the detector, notably the LSPs. Multiple jets arise from the complex decay chains of heavy objects. The same signature can arise in SM events, most often from top quark pair events and W+jets events in which the lepton comes from a W boson decay and the $\not{E}_{\mathrm{T}}$ arises from one or more undetected neutrinos. The challenge is to separate the SUSY from the SM events. This search is distinct from other recent CMS searches using the same final state topology [37] in that it uses an artificial neural network (ANN) to suppress SM backgrounds. It is also distinct in its use of M_{T}. By suppressing the SM backgrounds efficiently, the analysis permits less stringent requirements on event features such as total event energy, making it sensitive to some regions of the SUSY parameter space that might otherwise be out of reach.

6.1 Background suppression with the artificial neural network

After preselection, the event sample, although enriched in possible SUSY signal, still has a significant amount of SM backgrounds remaining. A number of event features distinguish signal from backgrounds, and rather than selecting on each of these individually, we place a requirement on a single variable that combines several of them with an ANN. Simulated SM background and SUSY events are used to train the ANN to distinguish between SM and new physics. The ANN infrastructure has been implemented using TMVA [38], which is included as a standard package in ROOT. The network has

a single hidden layer with 40 nodes and a tanh activation function. During training, weights are determined that minimize the RMS deviation of background events from zero and signal events from unity. The ANN is trained using LM0 for the signal. We find that LM0 has sufficiently generic features that an ANN trained using it is also efficient for other LM points (see Appendix A.1). ANNs trained with LM6 and LM9 do not improve sensitivity for CMS LM points. The SM MC[1] provides the background sample. We use about 7.4×10^4 background events and 1.9×10^4 signal events, weighted appropriately based on the cross sections of the relevant processes, for ANN training and testing. The training and testing samples are of equal size, and independent of each other. About 55% of the events used for training and testing belong to the muon channel, and the remainder to the electron channel. This analysis was developed with a smaller dataset (1.1 fb^{-1}) using looser H_T and $\not\!\!E_\text{T}$ cuts, and the ANN uses the tuning found at that time. Retraining the ANN might improve the efficiency very slightly for LM0, but for expediency, we choose to stick with the original ANN.

6.1.1 ANN inputs and training

The ANN uses physical variables that distinguish SUSY from the SM. Since the signal we are searching for is not well-defined, we choose discriminating variables that are more generic. While ANNs are capable of handling correlations between input variables, which invites the use of a large number of them, we prefer to keep the list short and simple. The input variables are also selected to limit the correlation between the ANN output (z_ANN) and $\not\!\!E_\text{T}$ since this facilitates background estimation later. The exhaustive list of variables we considered can be found in Appendix A.2. The variables chosen are:

[1]MC is an abbreviation for Monte Carlo, the computational algorithm used to generate simulated samples.

1. n_{jets}: The number of jets with p_{T} above 40 GeV. SUSY signals typically have heavy particles decaying via complex cascades, and as such, are likely to produce more jets than SM background processes.

2. H_{T}: The scalar sum of the p_{T}'s of jets with $p_{\text{T}} > 40$ GeV. Not only is SUSY more likely to produce more jets, it is also more likely to produce higher p_{T} jets, since heavier particles are involved. As such, SUSY events tend to have a higher value of H_{T}.

3. $\Delta\phi$ between the two leading p_{T} jets ($\Delta\phi(\text{j}_1,\text{j}_2)$): In SM background processes, the two leading jets are slightly more likely to be produced back-to-back than in SUSY events.

4. M_{T}: The transverse mass of the lepton and $\not\!\!E_{\text{T}}$ system. In top quark events and W+jets events, the lepton and $\not\!\!E_{\text{T}}$ often arise from the decay of a W boson, and as a result, M_{T} peaks near the W boson mass. Some SM events have higher M_{T} as a consequence of additional neutrinos from τ or semileptonic decays. In SUSY, high M_{T} arises from $\not\!\!E_{\text{T}}$ due to undetected LSPs.

Figure 6.1 shows the distributions of these variables for SM simulation and LM0. The most powerful input variable is M_{T}; n_{jets} and H_{T} also have considerable discriminating power. The $\Delta\phi(\text{j}_1,\text{j}_2)$ variable is weaker, but still improves the sensitivity of the search. Lepton p_{T} also discriminates between the SM and LM0, but is not included in the ANN due to its strong correlation with $\not\!\!E_{\text{T}}$ in SM. Additional variables either do little to improve sensitivity or introduce a correlation between z_{ANN} and $\not\!\!E_{\text{T}}$. The input variables have similar distributions in the muon and electron channels. The ANN is trained on the electron and muon channels combined, and this ANN is then used for both the channels.

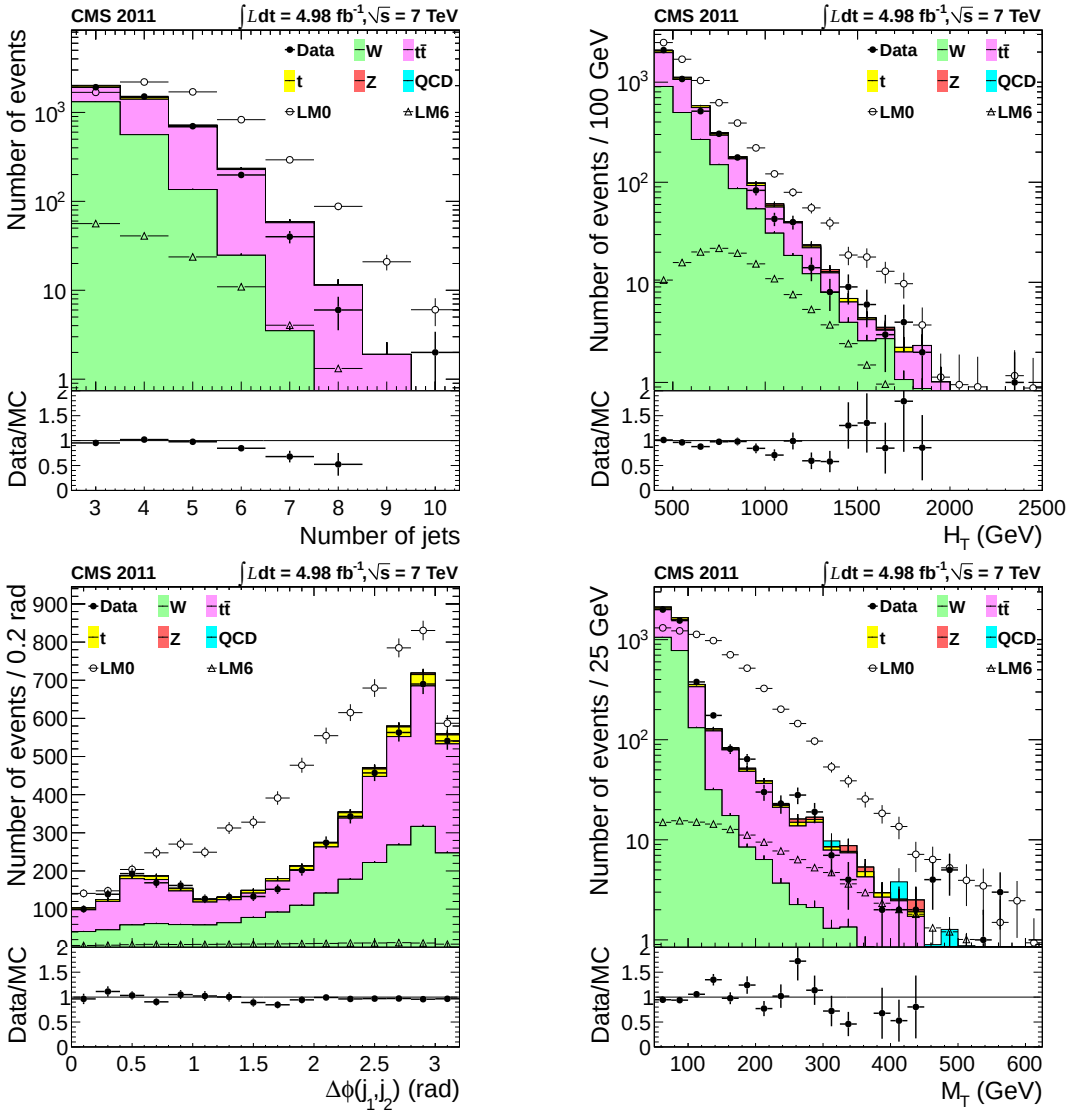

Figure 6.1: The distributions of n_{jets}, H_{T}, $\Delta\phi(\text{j}_1,\text{j}_2)$, and M_{T} for data (solid circles), simulated SM (stacked shaded histograms), LM0 (open circles) and LM6 (open triangles) events after preselection. The small plot beneath each distribution shows the ratio of data to simulated SM yields. The electron and muon channels are combined.

An ANN separates signal from background most efficiently if the MC on which it is trained reproduces the data. Figure 6.1 also compares distributions of the input variables between data and SM simulation for the electron and muon channels combined. There is reasonable agreement between the SM simulation and data. There is some discrepancy at high jet multiplicity. There is also some structure in the M_{T} distribution present in data that is not replicated by the simulation. A study was performed where the simulation was reweighted to match the M_{T} distribution in data, and tests showed that this did not affect the performance of our background estimation method.

6.1.2 ANN performance

Figure 6.2(a) compares z_{ANN} for data and SM simulation for all events surviving the preselection. Good agreement is observed. The SM is concentrated at small values of z_{ANN}, while the LM0 and LM6 SUSY samples, which are also shown, extend to high values of z_{ANN} where the SM is suppressed. Even though the ANN was trained using LM0, the separation between the SM and SUSY is as good for LM6 as for LM0, due to the larger M_{T} and H_{T} of LM6. Figure 6.2(b) compares z_{ANN} for the electron and muon channels in data; the distributions are very similar.

6.2 Signal region and yield

In order to search for SUSY, we define signal regions in the two-dimensional $\not\!\!E_{\mathrm{T}}$ and z_{ANN} plane. One region, referred to as the "low-$\not\!\!E_{\mathrm{T}}$" signal region, has $z_{\mathrm{ANN}} > 0.4$ and 350 GeV $< \not\!\!E_{\mathrm{T}} <$ 500 GeV, while the other, the "high-$\not\!\!E_{\mathrm{T}}$" signal region, has the same z_{ANN} range, but $\not\!\!E_{\mathrm{T}} >$ 500 GeV.

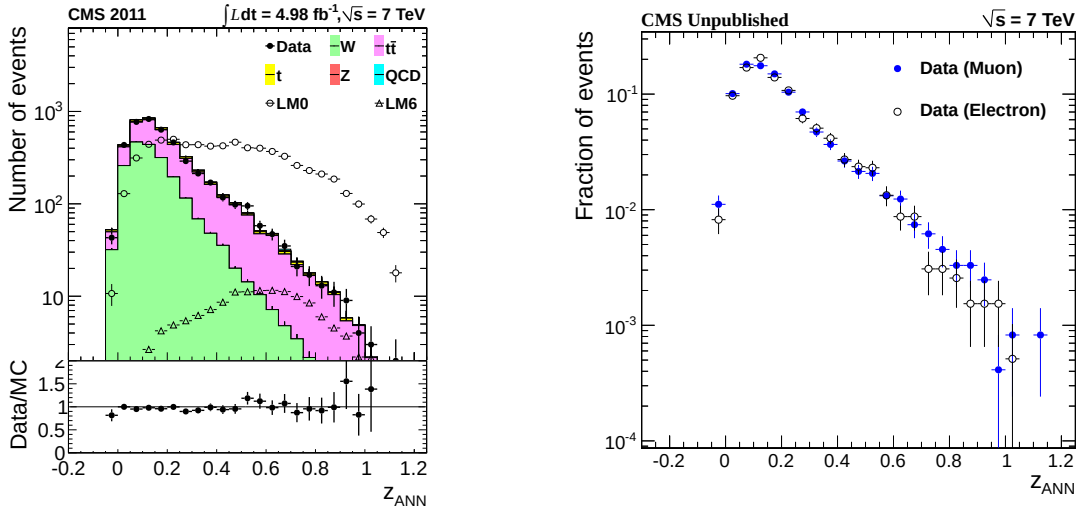

(a) (b)

Figure 6.2: (a): The z_{ANN} distribution of the data (solid circles) and simulated SM (stacked shaded histograms), LM0 (open circles) and LM6 (open triangles) events, after preselection. The small plot beneath shows the ratio of data to simulated SM yields. (b): Comparison of z_{ANN} for electron (black open circles) and muon (blue dots) channels in data. Histograms are normalized to unit area.

As shown in Fig. 6.3, placing the z_{ANN} cut at 0.4 minimizes the probability that the SM background will fluctuate up to the signal (LM6), taking in to account statistical uncertainty and assuming 30% systematic uncertainty in the background prediction. When the impact of signal contamination on the background is taken into account, there is a broad minimum, and we select $z_{\mathrm{ANN}} > 0.4$, which is near the low end of the minimum and a round value. The closure of the background prediction method (described in Sec. 6.3.1) is insensitive to this choice.

We observe 10 events in the low-$\not\!\!E_{\mathrm{T}}$ signal region and 1 event in the high-$\not\!\!E_{\mathrm{T}}$ signal region. For comparison, the predicted LM6 yields are 32.1 ± 0.4 (stat.) events and 21.0 ± 0.3 (stat.) events in the low-$\not\!\!E_{\mathrm{T}}$ and high-$\not\!\!E_{\mathrm{T}}$ regions, respectively.

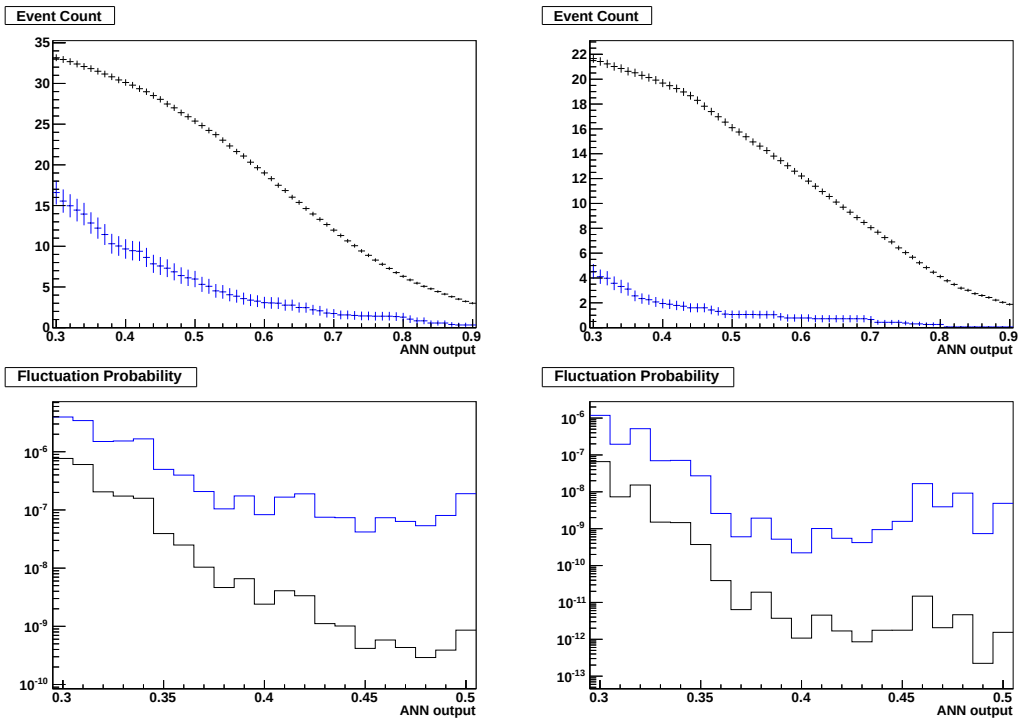

Figure 6.3: Optimization of the ANN cut. The top plots show the LM6 (black) and SM (blue) yields in the low-$\not\!\!E_{\mathrm{T}}$ signal region (left) and high-$\not\!\!E_{\mathrm{T}}$ signal region (right) as a function of the ANN cut. The bottom plots show the probability that the SM yield will fluctuate up to the LM6 yield, taking into account the statistical uncertainty and 30% systematic uncertainty in the background prediction for the low-$\not\!\!E_{\mathrm{T}}$ signal region (left) and high-$\not\!\!E_{\mathrm{T}}$ signal region (right). The blue lines include signal contamination bias, and the black lines do not.

6.3 Background subtraction method

The background is estimated using a sideband subtraction method in the two dimensional plane of $\not\!\!E_{\mathrm{T}}$ and z_{ANN}. The regions are shown in Fig. 6.4 and are denoted A, B, C, D for the low-$\not\!\!E_{\mathrm{T}}$ signal region and A, B', C and D' for the high-$\not\!\!E_{\mathrm{T}}$ signal region. The choice of boundaries for the sideband regions balances the competing needs of statistics and insensitivity to signal contamination against preserving similar event compositions in the signal and sideband regions. This was optimized using a procedure similar to the one described above for the signal region.

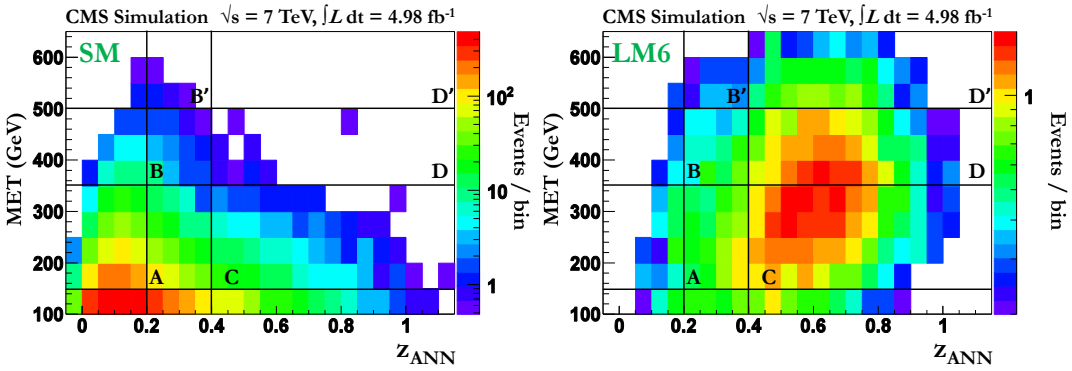

Figure 6.4: The yields of simulated SM (left) and LM6 (right) events in the $\not\!\!E_T$ versus z_{ANN} plane. The regions D and D' are the low-$\not\!\!E_T$ and high-$\not\!\!E_T$ signal regions. The sideband regions are also indicated.

The predicted yield in region D is given by

$$D_{pred} = \frac{B \times C}{A}, \tag{6.1}$$

and similarly for region D'. This is equivalent to using the $\not\!\!E_T$ distribution of the low z_{ANN} sideband regions (A, B, and B') as a template for the $\not\!\!E_T$ distribution of events with high z_{ANN} (C, D and D'), normalized using the yield in A and C. We test the correctness of this estimation procedure using SM simulation: Fig. 6.5(a) demonstrates that the $\not\!\!E_T$ distributions for low and high z_{ANN} regions agree well in shape.

If a signal is present, it enters primarily the signal regions D and D', but there are also significant contributions relative to the SM in regions B and B', increasing the predicted backgrounds in D and D'. Figure 6.5(b) shows that this signal contamination would nonetheless not mask an LM6 signal (the red points remain well above black).

Table 6.1 summarizes the event yields in the sideband subtraction regions for the various components of the SM background. W+jets and $t\bar{t}$ dominate in all the regions, though their relative proportion varies. The W+jets events are most important at low z_{ANN} since M_T tends to peak near the W boson mass, but because the W bosons (and hence their daughters) can be highly boosted, they extend to very high values of $\not\!\!E_T$.

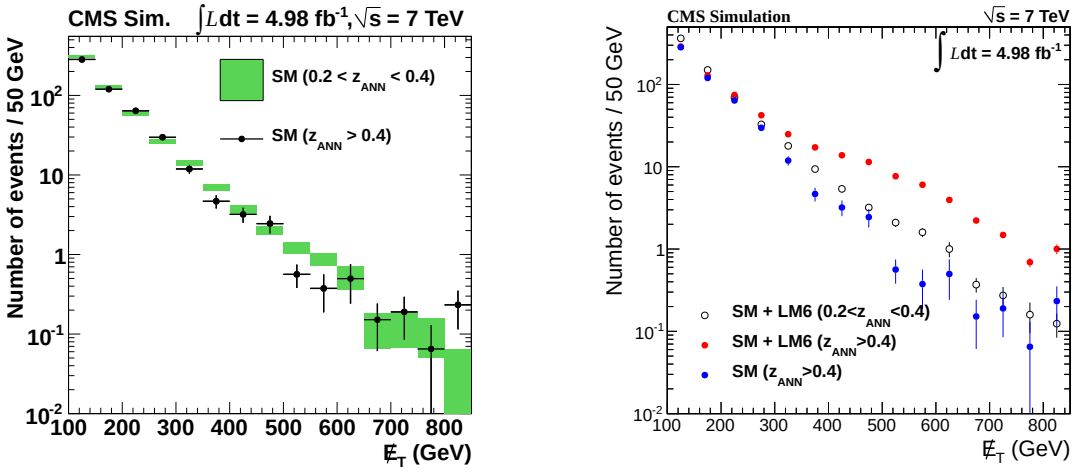

(a) (b)

Figure 6.5: (a): The $\not\!\!E_{\mathrm{T}}$ distributions of simulated SM events in the z_{ANN} signal region (solid circles) and sideband (green bars). (b): The $\not\!\!E_{\mathrm{T}}$ distribution of low z_{ANN} events in the presence of LM6 (black open circles), the distribution of high z_{ANN} events in the presence of LM6 (red dots), and the distribution of high z_{ANN} events with SM only (blue dots). The distributions are normalized in the $\not\!\!E_{\mathrm{T}}$ sideband, 150 GeV $< \not\!\!E_{\mathrm{T}} <$ 350 GeV (regions A and C for the two distributions respectively). The last histogram bin includes overflow.

As seen in Fig. 6.2(a), $t\bar{t}$ is more likely to have high values of z_{ANN} than W+jets; this is because of the presence of dilepton $t\bar{t}$ events, in which both W bosons (from the top quark pair) decay leptonically, but only one lepton is identified (dilepton (ℓ)). There is also a small contribution from events in which the lepton comes from the decay of a τ produced from top quark decay, with the other top quark decaying either leptonically (dilepton ($\tau \rightarrow \ell$)) or hadronically (single τ). The remaining small backgrounds come from single top quark, QCD multijet and Z+jets events.

The simulated samples for QCD multijet and Z+jets lack adequate statistics to populate the high $\not\!\!E_{\mathrm{T}}$ regions (B, B', D and D'). For the numbers quoted in Table 6.1 for QCD multijet and Z+jets events, we employ an extrapolation technique based on loosening the z_{ANN} and $\not\!\!E_{\mathrm{T}}$ requirements. We fit an exponential function to the $\not\!\!E_{\mathrm{T}}$ distribution of QCD and Z+jets events above 100 GeV (Fig. 6.6), and then take the integral over 150 $< \not\!\!E_{\mathrm{T}} <$

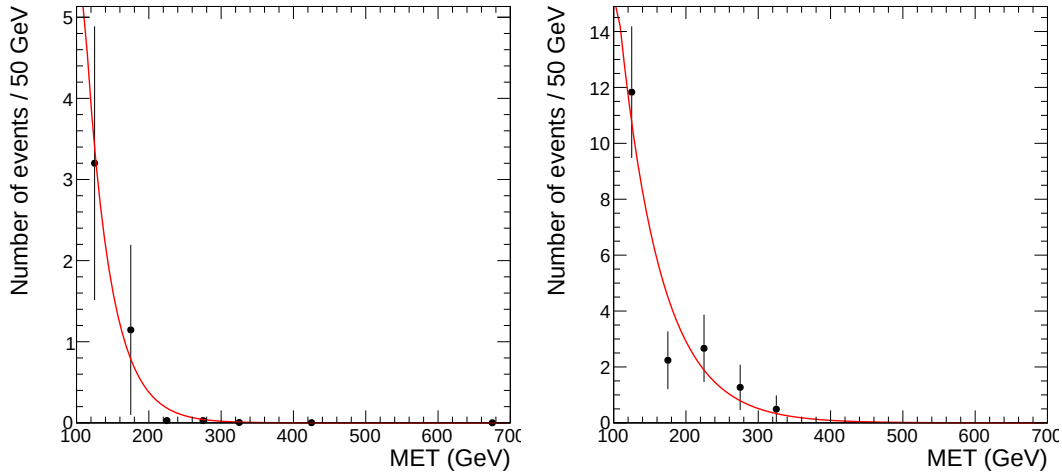

Figure 6.6: QCD (left) and Z+jets (right) $\not\!\!E_T$ distributions, fit with an exponential to estimate contributions from these samples in the signal and sideband regions.

350 GeV (for regions A and C), and over $350 < \not\!\!E_T < 1000$ GeV (for regions B, B', D and D'). We then use Fig. 6.2(a) to estimate the fraction of SM events with $0.2 < z_{ANN} < 0.4$ (25%) and $z_{ANN} > 0.4$ (10%). For regions A, B, and B', we multiply the corresponding integrals by 0.25, and for regions C, D and D', we multiply the corresponding integrals by 0.1. The extrapolated numbers for all the regions are consistent with the numbers obtained from the simulated samples. Based on the simulated yields in the sideband and signal regions, QCD multijet and Z+jets events are considered negligible.

The total SM simulation yields agree well with data in all regions.

Figure 6.7 compares the $\not\!\!E_T$ distributions of data and SM simulation in the z_{ANN} signal and sideband regions, as well as the z_{ANN} distributions of data and SM simulation in different $\not\!\!E_T$ regions. Agreement is good. LM6 is included in the plots for comparison purposes.

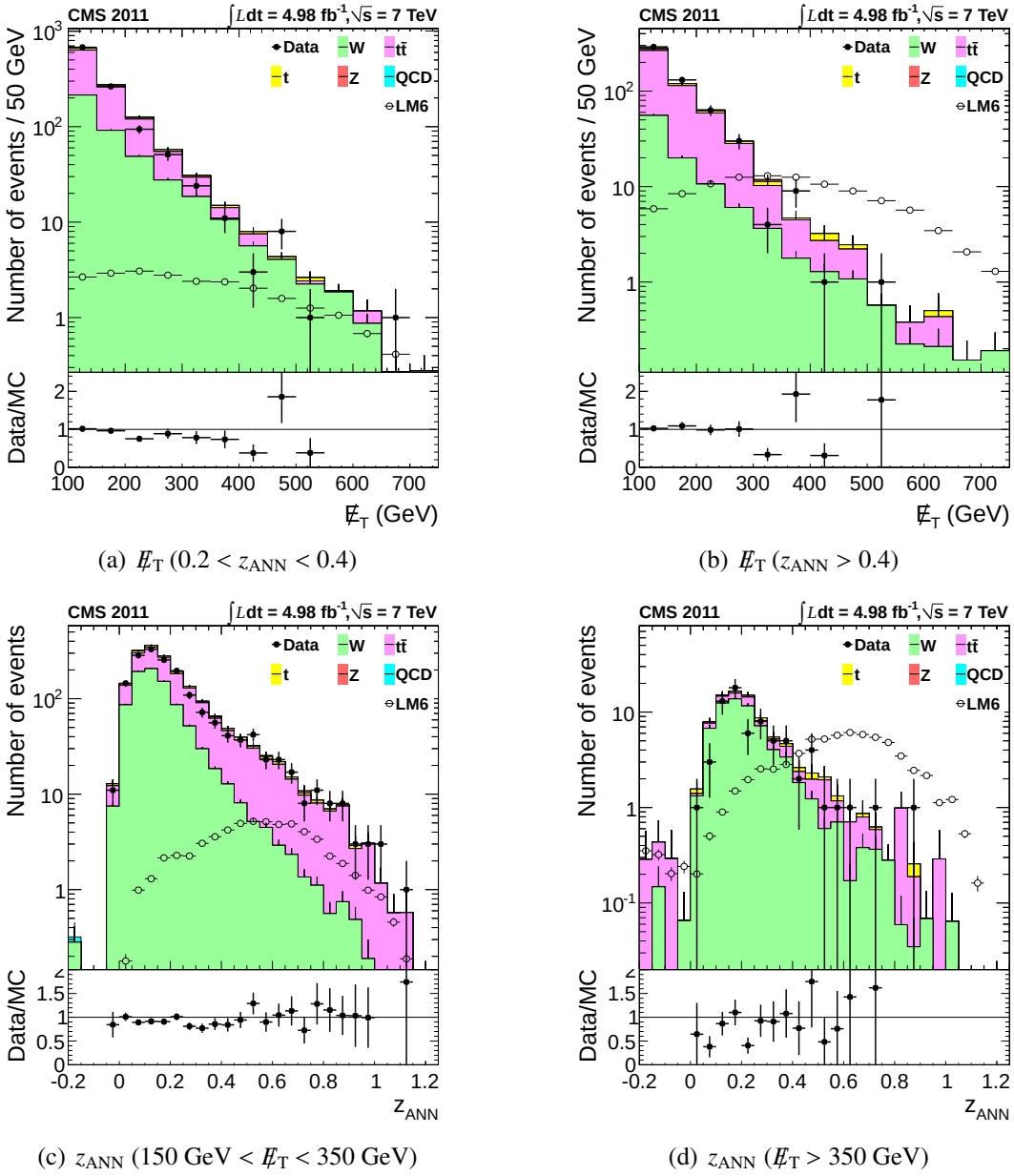

(a) $\not\!\!E_T$ ($0.2 < z_{ANN} < 0.4$)

(b) $\not\!\!E_T$ ($z_{ANN} > 0.4$)

(c) z_{ANN} (150 GeV $< \not\!\!E_T <$ 350 GeV)

(d) z_{ANN} ($\not\!\!E_T >$ 350 GeV)

Figure 6.7: Distributions of $\not\!\!E_T$ in slices of z_{ANN} (top) and z_{ANN} in slices of $\not\!\!E_T$ (bottom) for data (solid circles), simulated SM (stacked shaded histograms), and simulated LM6 events (open circles). The small plot beneath each distribution shows the ratio of data to simulated SM yields.

Table 6.1: Event counts for various regions defined by the background subtraction method.

Sample Type	A	B	B'	C	D	D'
	Low z_{ANN} $\not\!\!E_{\mathrm{T}}$ sb	Low z_{ANN} Low $\not\!\!E_{\mathrm{T}}$	Low z_{ANN} High $\not\!\!E_{\mathrm{T}}$	High z_{ANN} $\not\!\!E_{\mathrm{T}}$ sb	High z_{ANN} Low $\not\!\!E_{\mathrm{T}}$	High z_{ANN} High $\not\!\!E_{\mathrm{T}}$
$t\bar{t}$: single lepton	210 ± 8	4.8 ± 1.1	0.2 ± 0.2	55 ± 4	1.7 ± 0.7	$0.0^{+0.2}_{-0.0}$
$t\bar{t}$: dilepton (ℓ)	56 ± 4	0.3 ± 0.3	0.01 ± 0.01	109 ± 5	3.6 ± 1.0	0.2 ± 0.2
$t\bar{t}$: dilepton ($\tau \to \ell$)	3.9 ± 1.1	0.01 ± 0.01	0.3 ± 0.3	4.3 ± 1.0	$0.0^{+0.2}_{-0.0}$	0.2 ± 0.2
$t\bar{t}$: single τ	9.4 ± 1.7	0.3 ± 0.3	$0.0^{+0.2}_{-0.0}$	2.6 ± 0.8	$0.0^{+0.2}_{-0.0}$	$0.0^{+0.2}_{-0.0}$
$t\bar{t}$	279 ± 9	5.4 ± 1.2	0.5 ± 0.3	171 ± 7	5.3 ± 1.2	0.4 ± 0.3
W+jets	186 ± 3	20.4 ± 1.1	5.8 ± 0.6	40 ± 2	4.1 ± 0.5	1.6 ± 0.3
Single top quark	20 ± 1	1.5 ± 0.3	0.2 ± 0.1	11 ± 1	0.9 ± 0.2	0.1 ± 0.1
Z+jets	2.1 ± 0.3	$0.07^{+0.12}_{-0.07}$	$0.07^{+0.12}_{-0.07}$	0.8 ± 0.1	$0.03^{+0.05}_{-0.03}$	$0.03^{+0.05}_{-0.03}$
QCD multijet	$0.3^{+0.4}_{-0.3}$	$0.00^{+0.04}_{-0.00}$	$0.00^{+0.04}_{-0.00}$	0.1 ± 0.1	$0.00^{+0.02}_{-0.00}$	$0.00^{+0.02}_{-0.00}$
Total SM	487 ± 9	27.3 ± 1.8	6.6 ± 0.7	224 ± 7	10.3 ± 1.3	2.1 ± 0.4
Data	433	22	2	228	10	1
LM6	11.2 ± 0.3	6.0 ± 0.2	3.9 ± 0.1	44.6 ± 0.5	32.1 ± 0.4	21.0 ± 0.3

6.3.1 Closure of the background estimation method in SM simulation

The results of applying the background subtraction method to the SM simulation are summarized in Table 6.2 and are shown in Figs. 6.8 (W+jets and $t\bar{t}$) and 6.5(a) (all SM). As shown in the table, each major component of the SM sample closes within statistics. For the full SM, the method predicts a modest excess of events, which arises because the low z_{ANN} sample has a harder $\not\!\!E_{\mathrm{T}}$ distribution spectrum than the high z_{ANN} sample due to the larger proportion of W+jets. We quantify this excess using $\kappa \equiv \frac{AD}{BC} = D/D_{pred}$ and using the SM simulation, find $\kappa = 0.82 \pm 0.12$ in the low-$\not\!\!E_{\mathrm{T}}$ signal region and 0.69 ± 0.16 in the high-$\not\!\!E_{\mathrm{T}}$ signal region.

In the next chapter, we apply this background estimation technique to data, and present our search results.

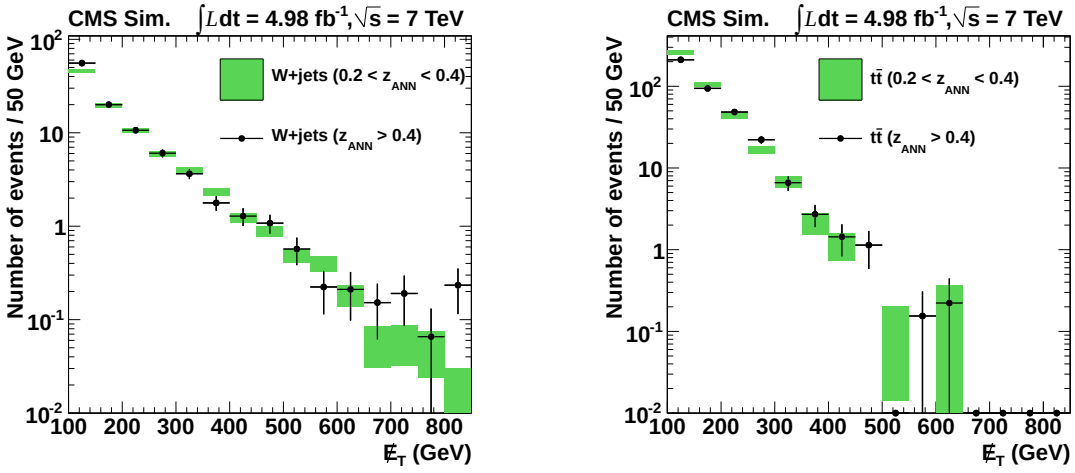

(a) W+jets (b) $t\bar{t}$

Figure 6.8: The $\not\!\!E_{\mathrm{T}}$ distributions of simulated W+jets (a) and $t\bar{t}$ (b) events in the z_{ANN} signal region (solid circles) and sideband (green bars). The normalization region is 150 GeV < $\not\!\!E_{\mathrm{T}}$ < 350 GeV. The last histogram bin includes overflow.

Table 6.2: Closure test of the background estimation method using SM simulation. Regions D and D' are the low-$\not\!\!E_{\mathrm{T}}$ and high-$\not\!\!E_{\mathrm{T}}$ signal regions. For D_{pred} ($\mathrm{D'}_{pred}$), the values for the SM components are based on their respective yields in regions A, B and C (A, B' and C). For total SM, the value of D_{pred} ($\mathrm{D'}_{pred}$) is based on the total SM yields in regions A, B and C (A, B' and C). Hence, the values of D_{pred} and $\mathrm{D'}_{pred}$ for total SM cannot be obtained by adding the corresponding values for the SM components.

Sample Type	D	D_{pred}	D'	$\mathrm{D'}_{pred}$
$t\bar{t}$	5.3 ± 1.2	3.3 ± 0.8	0.4 ± 0.3	0.3 ± 0.2
W+jets	4.1 ± 0.5	4.4 ± 0.3	1.6 ± 0.3	1.3 ± 0.1
Single top quark	0.9 ± 0.2	0.8 ± 0.2	0.1 ± 0.1	0.1 ± 0.1
Total SM	10.3 ± 1.3	12.6 ± 0.9	2.1 ± 0.4	3.0 ± 0.3

CHAPTER 7

RESULTS OF THE SEARCH FOR SUPERSYMMETRY

In the previous chapter, we looked at how SM backgrounds are suppressed by the use of an ANN. We delineated a technique to estimate the remaining background, and using SM MC, checked to see that the method performed as expected. In this chapter, we apply this background estimation process to data (Sec. 7.1). Since we do not see an excess of events in data compared to the expected SM background, exclusion limits in SUSY parameter spaces need to be set. Before this can be done, the systematic uncertainties associated with the background estimation method and the signal efficiency need to be quantified: this is done in Sec. 7.2 and Sec. 7.3, respectively. Finally, we set limits in the context of the CMSSM and the T3w simplified model (Sec. 7.4).

7.1 Background prediction in data

Figure 7.1 shows the $\not\!\!E_{\mathrm{T}}$ distributions of the data in the high and low z_{ANN} regions, after normalizing in the region 150 GeV $< \not\!\!E_{\mathrm{T}} <$ 350 GeV (A and C). To arrive at the final background estimate, we correct the background prediction of the data by the deviation of $\kappa = D/D_{pred}$ from unity seen in the SM simulation. Recall that κ arises from differences in the $\not\!\!E_{\mathrm{T}}$ spectra of W+jets and $t\bar{t}$ events. The original and corrected predictions are shown in Table 7.1. In the section on systematic uncertainties, we will quantify the uncertainty on this correction. In the low-$\not\!\!E_{\mathrm{T}}$ signal region, we expect 9.5 ± 2.2 (stat.) events and in the high-$\not\!\!E_{\mathrm{T}}$ signal region we expect 0.7 ± 0.5 (stat.) events. The observed yields are 10 and 1 events respectively; no excess is observed.

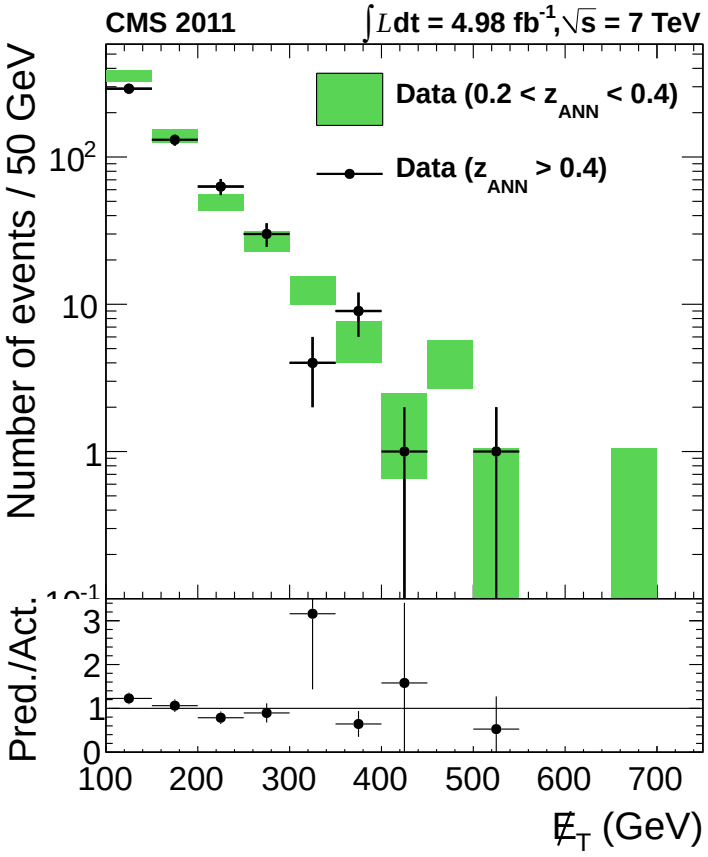

Figure 7.1: The $\not\!\!E_T$ distributions in data for the z_{ANN} signal region (solid circles) and sideband (green bars). The normalization region is $150 < \not\!\!E_T < 350$ GeV. The small plot beneath shows the ratio of normalized sideband to signal yields.

Table 7.1: The background prediction for data. The corrected prediction ignores the statistical uncertainty on the correction factor, since it is treated as a systematic uncertainty.

Signal region	Actual	Predicted (no correction)	Predicted (w/ correction)
Low-$\not\!\!E_T$	10	11.6 ± 2.6	9.5 ± 2.2
High-$\not\!\!E_T$	1	1.1 ± 0.7	0.7 ± 0.5

7.1.1 Background checks

The background subtraction method and closure test depend on the shape of the $\not\!\!E_T$ distribution. In the data, for low z_{ANN}, the ratio of events in the $\not\!\!E_T$ signal to sideband regions is 0.055 ± 0.012 (regions (B+B')/A). For SM simulation, the same ratio is 0.069 ± 0.004. Consistency between these values shows that the SM simulation predicts the ratio of $\not\!\!E_T$ signal to $\not\!\!E_T$ sideband yields (at low z_{ANN}) accurately within a factor of 1.25 ± 0.28. For region C (high z_{ANN}, $\not\!\!E_T$ sideband), the ratio of SM simulation yield to data yield is 0.98 ± 0.07, again consistent with unity.

Examination of the $\not\!\!E_T$ spectra in the data also provides a loose cross-check. If the low and high z_{ANN} regions have the same $\not\!\!E_T$ distributions, as is assumed, the ratio of their $\not\!\!E_T$ distributions should be a constant. A linear fit to the ratio of low to high z_{ANN} events as a function of $\not\!\!E_T$ (Fig. 7.1) in the region $150 < \not\!\!E_T < 300$ GeV, where signal contamination is small, gives a slope consistent with 0. This is also true if we correct data yields by subtracting out predicted LM6 yields.

7.2 Systematic uncertainties in the background determination

Details of the simulation can affect SM simulation closure, which quantifies bias in the background estimate. In this section, we quantify the impact on closure of plausible variations in the SM simulation parameters, efficiencies and resolutions. For each SM simulation feature that might affect closure, we shift the SM simulation, find the change in the yields in the sideband and signal regions, and then recompute $\kappa = D/D_{pred}$. The deviation of κ from its original value is an estimate of the systematic uncertainty from that source. Table 7.2 lists the results of these studies, and Table 7.3 summarizes the

systematic uncertainty on the background prediction.

7.2.1 Baseline MC closure

For both the low-$\not\!\!E_T$ and high-$\not\!\!E_T$ signal regions, the central value of κ deviates from unity, and we correct the data for this effect. Accordingly, we assign systematic uncertainties equal to the statistical uncertainties in the correction factor. These are 15% and 23% in the low-$\not\!\!E_T$ and high-$\not\!\!E_T$ signal regions, respectively.

7.2.2 Jet, $\not\!\!E_T$ and lepton energy scale

The jet energy scale (JES) uncertainty [18] and the associated $\not\!\!E_T$ scale uncertainty is estimated as follows: all jets above 10 GeV are varied by p_T and η dependent uncertainties, and all PF jets below 10 GeV (which are considered to represent unclustered energy) are varied by 10%. The results of these variations are then propagated to $\not\!\!E_T$. This leads to an uncertainty in κ of 3% in the low-$\not\!\!E_T$ signal region, and 4% in the high-$\not\!\!E_T$ signal region. For the lepton energy scale (LES), in the muon channel, the muon p_T is varied by ± 1%, and in the electron channel, the electron p_T is varied by ± 1% or ± 2.5% (depending on whether the electron is in the ECAL barrel or endcap, respectively). This leads to an uncertainty in κ of 3% in the low-$\not\!\!E_T$ signal region, and 5% in the high-$\not\!\!E_T$ signal region.

7.2.3 Standard model cross sections

The bulk of the SM event yield in the sideband and signal regions comes from W+jets and $t\bar{t}$ events. We vary the cross section of W+jets by ± 30%, and of $t\bar{t}$ by ± 20%. Even though CMS has measured overall W boson and $t\bar{t}$ cross sections to better precision than this, the variations used by us are consistent with studies [39] done after applying preselection requirements similar to what we use in this analysis. The variation of each of these cross sections is done in steps of 1%, and simultaneously. This means we get a distribution of κ values (there are 60×40 = 2400 such values). The RMS of this distribution is then taken as the uncertainty on κ due to W+jets and $t\bar{t}$ cross section uncertainty. The uncertainties are 3% and 2% in the low-$\not\!\!E_{\mathrm{T}}$ and high-$\not\!\!E_{\mathrm{T}}$ signal regions, respectively. Besides W+jets and $t\bar{t}$ events, the SM simulation also includes single top quark, Z+jets and QCD multijet events. The combined cross section of these is varied by ± 50%. This leads to 1% uncertainty on κ in both the low-$\not\!\!E_{\mathrm{T}}$ and high-$\not\!\!E_{\mathrm{T}}$ signal regions.

7.2.4 Dilepton feed-down in $t\bar{t}$

Dilepton $t\bar{t}$ events in which one lepton is lost is a source of background. Its magnitude depends on the geometric acceptance for our analysis, and the probability that a lepton will fail loose identification and isolation requirements used to veto events that have a second lepton. Isolation and identification efficiencies are obtained using the tag-and-probe method [40]. For loose requirements consistent with our lepton veto, the product of electron identification and isolation efficiencies is 0.85 ± 0.03, implying an inefficiency of 0.15 ± 0.03. For muons, the identification efficiency is 0.91 ± 0.03, implying an inefficiency of 0.09 ± 0.03. Since the fractional uncertainties in the identification

inefficiency are 20% and 30% for electrons and muons respectively, we vary the contribution of dilepton $t\bar{t}$ events by 25%. We expect that this variation is conservative, since the geometric acceptance is understood at a level better than 25%. This leads to uncertainties of 1% and 7% in the low-$\not\!\!E_{\mathrm{T}}$ and high-$\not\!\!E_{\mathrm{T}}$ signal regions, respectively.

7.2.5 Pile-up

In this analysis, the SM simulation is re-weighted so that the vertex multiplicity (nVertex) distribution in SM simulation matches the distribution seen in data. There is a statistical uncertainty associated with these re-weighting factors, and since the exact values of the re-weighting factors can slightly alter certain distributions (like M_{T}), it is necessary to check what systematic effect this statistical uncertainty can have. The mean number of vertices in data is about 7. In one iteration, all events with greater than 7 vertices have their weights scaled up by a factor equal to the fractional statistical uncertainty of the re-weighting factor for that nVertex bin, and all events with fewer than 7 vertices have their weights scaled down similarly. This way, the total yield stays roughly the same, but the relative proportions in the various regions can change. In another iteration, the opposite scaling is done, and the average deviation gives us a conservative estimate of this systematic uncertainty. This means an uncertainty of 0.5% and 0.3% in the low-$\not\!\!E_{\mathrm{T}}$ and high-$\not\!\!E_{\mathrm{T}}$ signal regions, respectively.

7.2.6 W boson p_{T} spectrum

The $\not\!\!E_{\mathrm{T}}$ distribution of W+jets events is determined largely by the p_{T} spectrum of the W bosons. A comparison of the p_{T} spectrum of the Z boson between data and simula-

tion [41] is a useful way to quantify how well the W boson p_{T} spectrum is modeled in simulated events. We vary the weights of W+jets events using this factor: $1 \pm (\mathrm{W}p_{\mathrm{T}} - 100$ GeV$) \times 0.00075$. The exact functional form is chosen so as to conservatively cover the data-simulation discrepancy and its uncertainty observed in the Z boson study. This gives an uncertainty of 10% and 2% in the low-$\not\!\!E_{\mathrm{T}}$ and high-$\not\!\!E_{\mathrm{T}}$ signal regions, respectively.

7.2.7 W boson polarization

For a given W boson momentum spectrum, the $\not\!\!E_{\mathrm{T}}$ distribution is affected by the W boson polarization. We evaluate this uncertainty based on a method explained in detail elsewhere [39]. The W+jets cross section can be written as a function of $\cos\theta^*$, the cosine of polar angle of the charged lepton in the W rest frame, as:

$$dN(W^{+-})/d\cos\theta^* \sim f_L(1 \mp \cos\theta^*)^2 + f_R(1 \pm \cos\theta^*)^2 + 2f_0 \sin^2\theta^*$$

The fractions f_L, f_R and f_0 are obtained from fits to the generator-level distributions of $\cos\theta^*$ in different bins of W boson p_{T} and rapidity. The W+jets MC is reweighted in three ways: (i) $f_L - f_R$ is varied by 10% for both W^+ and W^-, (ii) $f_L - f_R$ is varied by 5% for either W^+ or W^-, and (iii) f_0 is varied by 10% for both W^+ and W^-. For all three variations, we take the largest change in κ, and add these three changes in quadrature to get the final estimate of the systematic uncertainty. This is summarized in Table 7.4.

7.2.8 Lepton trigger efficiency

The dependence of the trigger efficiency on the p_{T} of the lepton differs for data and SM simulation by 10% at 20 GeV, and this difference reduces (roughly linearly) to 0% at

about 40 GeV. To quantify the impact, we vary the weights of the events by this amount. This leads to an uncertainty in κ of 0.3% and 0.4% in the low-$\not\!\!E_{\mathrm{T}}$ and high-$\not\!\!E_{\mathrm{T}}$ signal regions, respectively. Additionally, the muon trigger efficiency in the endcap differs by about 5% between data and SM simulation, so we vary the weight of the events accordingly. This causes a 0.1% uncertainty on κ in both the low-$\not\!\!E_{\mathrm{T}}$ and high-$\not\!\!E_{\mathrm{T}}$ signal regions.

7.2.9 Summary of systematic uncertainties in the backgrounds

Adding the systematic uncertainties in Table 7.3 gives a total of 19% in the low-$\not\!\!E_{\mathrm{T}}$ signal region and 26% in the high-$\not\!\!E_{\mathrm{T}}$ signal region. We will use these to extract bounds on SUSY.

7.3 Signal efficiency uncertainty

We estimate the signal efficiency for each point in the CMSSM scan ($\tan\beta = 10, A_0 = 0, \mu > 0$) using simulation. However, as discussed in the previous section, simulation yields are likely to be affected by certain sources of systematic uncertainty. In the context of signal efficiency, the relevant sources of experimental uncertainty are: integrated luminosity, JES, LES and $\not\!\!E_{\mathrm{T}}$ scale, and lepton trigger efficiency. The uncertainty on the integrated luminosity is 2.2% [42], and is accounted for separately in the limit-setting code. The uncertainty due to lepton trigger efficiency is taken to be 3% across the entire plane. The remaining sources are calculated point-by point. In the low-$\not\!\!E_{\mathrm{T}}$ region, the total experimental uncertainty is about 3.5% for moderate values of m_0 and $m_{1/2}$; above a line $900\,\mathrm{GeV} - 0.2 \times m_0$, this uncertainty rises to 5%. It is also about 5% in a small region

Table 7.2: Effect of systematic uncertainty sources on the background estimation method. CS stands for the cross section of the single top, QCD and Z+jets samples. DL stands for dilepton feed-down. PU stands for pile-up. LPTE stands for lepton p_{T} efficiency, and MEE stands for muon η efficiency. The MC yields in this table assume an integrated luminosity of 4.67 fb^{-1} instead of 4.98 fb^{-1}, and should be scaled up accordingly.

Variation	A	B	B'	C	D	D'	$\kappa = D/D_{pred}$	$\kappa' = D'/D'_{pred}$
Data	433	22	2	228	10	1		
Original MC	457	25.4	6.1	212	9.7	1.9	0.82	0.69
JES up	494	27.0	6.5	232	10.1	2.2	0.80	0.72
JES down	424	23.8	5.8	195	9.2	1.8	0.85	0.67
LES up	463	25.4	6.0	215	9.8	2.0	0.83	0.72
LES down	453	25.8	6.1	208	9.4	2.2	0.79	0.80
CS up	468	26.1	6.2	218	10.1	2.0	0.83	0.68
CS down	446	24.8	6.0	205	9.2	1.9	0.81	0.69
DL up	474	25.5	6.2	243	10.7	2.1	0.81	0.65
DL down	440	25.3	6.0	180	8.7	1.8	0.84	0.75
PU up	457	25.4	6.1	212	9.6	1.9	0.82	0.69
PU down	457	25.4	6.1	212	9.7	2.0	0.83	0.69
W p_{T} up	483	31.2	8.6	217	10.8	2.7	0.77	0.70
W p_{T} down	430	19.6	3.6	206	8.5	1.2	0.90	0.68
LPTE up	463	25.7	6.2	214	9.7	2.0	0.82	0.69
LPTE down	451	25.2	6.1	210	9.6	1.9	0.82	0.69
MEE up	458	25.5	6.1	212	9.7	1.9	0.82	0.69
MEE down	455	25.4	6.1	211	9.6	1.9	0.82	0.69

Table 7.3: Summary of the systematic uncertainties in the background determination.

Source	Low-$\not\!\!E_{\mathrm{T}}$ signal reg.	High-$\not\!\!E_{\mathrm{T}}$ signal reg.
MC statistics	15%	23%
Jet and $\not\!\!E_{\mathrm{T}}$ energy scales	3%	4%
Lepton and $\not\!\!E_{\mathrm{T}}$ energy scales	3%	5%
W boson and $t\bar{t}$ cross sections	3%	2%
Other cross sections	1%	1%
Dilepton feed-down	1%	7%
Pile-up	0.5%	0.3%
W boson p_{T} spectrum	10%	2%
W boson polarization	1%	3%
Lepton trigger efficiency	0.3%	0.4%
Total	19%	26%

Table 7.4: Change in κ due to various W boson polarization variations.

Source	Low-$\not\!\!E_T$ signal reg.	High-$\not\!\!E_T$ signal reg.
Variation 1	0.0104	0.0166
Variation 2	0.0039	0.0060
Variation 3	0.0004	0.0002
Total	1%	3%

$m_{1/2} < 200$ GeV and $m_0 < 600$ GeV. For the high-$\not\!\!E_T$ signal region, the total experimental uncertainty is fairly flat, about 4-5%. The relevant sources of theoretical uncertainty are PDFs and theoretical scale, both of which are calculated point-by-point [43].

7.4 Bounds on SUSY

In the low-$\not\!\!E_T$ signal region, we observe 10 events with a predicted background of 9.5 $\pm$ 2.2 (stat.) $\pm$ 1.8 (syst.). There is no sign of an excess of events beyond background. Likewise, in the high-$\not\!\!E_T$ signal region, we observe 1 event with a predicted background of 0.7 $\pm$ 0.5 (stat.) $\pm$ 0.2 (syst.) events, and again see no excess. We extract bounds on SUSY parameters by combining the results in the low-$\not\!\!E_T$ and high-$\not\!\!E_T$ signal regions. The limits are computed using the frequentist CL_s method [44] with a one-sided profile-likelihood test statistic, uncertainties are modeled as log-normal, and signal contamination of the sideband subtraction regions is taken into account. Points on the CMSSM plane that have CL_s values under 0.05 are excluded at the 95% confidence level, resulting in the exclusion curves shown in Fig. 7.2. All points that lie below the curves are excluded. The advantage of combining the two signal regions during limit-setting can be seen in Fig. 7.3, which shows the limits obtained by using the low-$\not\!\!E_T$ and high-$\not\!\!E_T$ signal regions by themselves.

We account for signal contamination during limit setting by subtracting from our signal

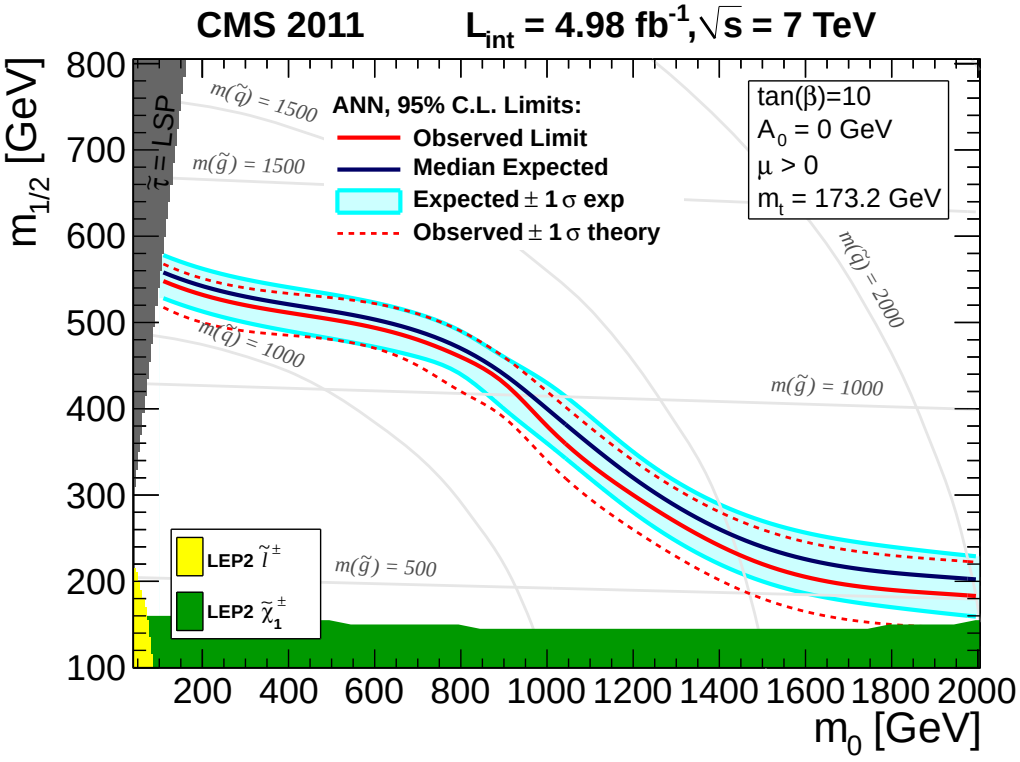

Figure 7.2: CMSSM limit by combining the low-$\not\!\!E_T$ and high-$\not\!\!E_T$ signal regions.

yield the expected increase to the background prediction. Suppose S is the original signal yield in the signal region, B is the background prediction obtained from the data yields in the control regions, and B' is the background prediction when signal is added to the control regions. The consequence of signal contamination is to make $B' > B$. The corrected signal yield S' is then defined as $S' = S - (B' - B)$. Since $S' < S$, the limits obtained by accounting for signal contamination will always be worse than limits obtained by ignoring it.

7.4.1 Limits using Simplified Models

In addition to the CMSSM limits already shown, we also derive limits using the T3w simplified model, introduced in Chapter 2 (Fig. 2.11). The limits are derived by com-

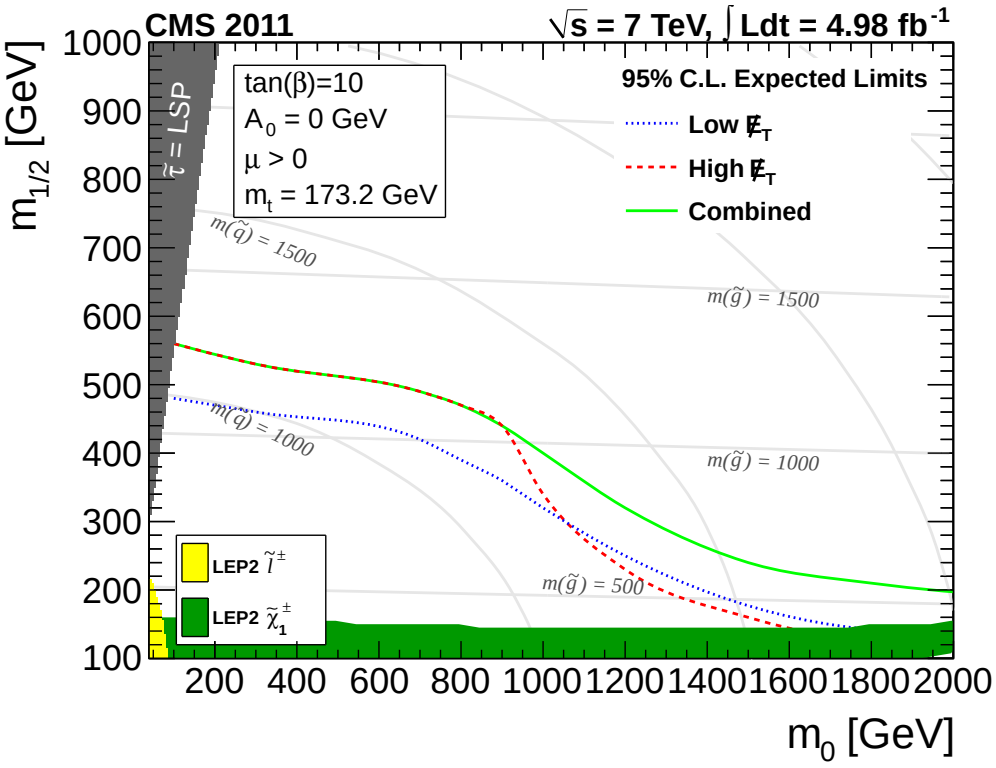

Figure 7.3: Expected CMSSM limits using the low-$\not\!\!E_T$ and high-$\not\!\!E_T$ signal regions by themselves, compared to the expected limit from shape analysis.

bining our low-$\not\!\!E_T$ and high-$\not\!\!E_T$ signal regions. The signal efficiencies for the two signal regions in the T3w planes corresponding to x = 0.25, 0.5, and 0.75 can be seen in Fig. 7.4.

The experimental uncertainty on the signal efficiency is calculated point-by-point for each plane using the same methods used for the CMSSM plane. We also account for the effect of finite statistics involved in the signal efficiency calculation, since unlike the CMSSM plane where we only care about exclusion contours, for the simplified model we are also interested in the observed cross section limit for each point on the plane. We also account for the effect of signal contamination on our limits. This is done in a three-step process:

- We calculate the observed limit without assuming signal contamination.

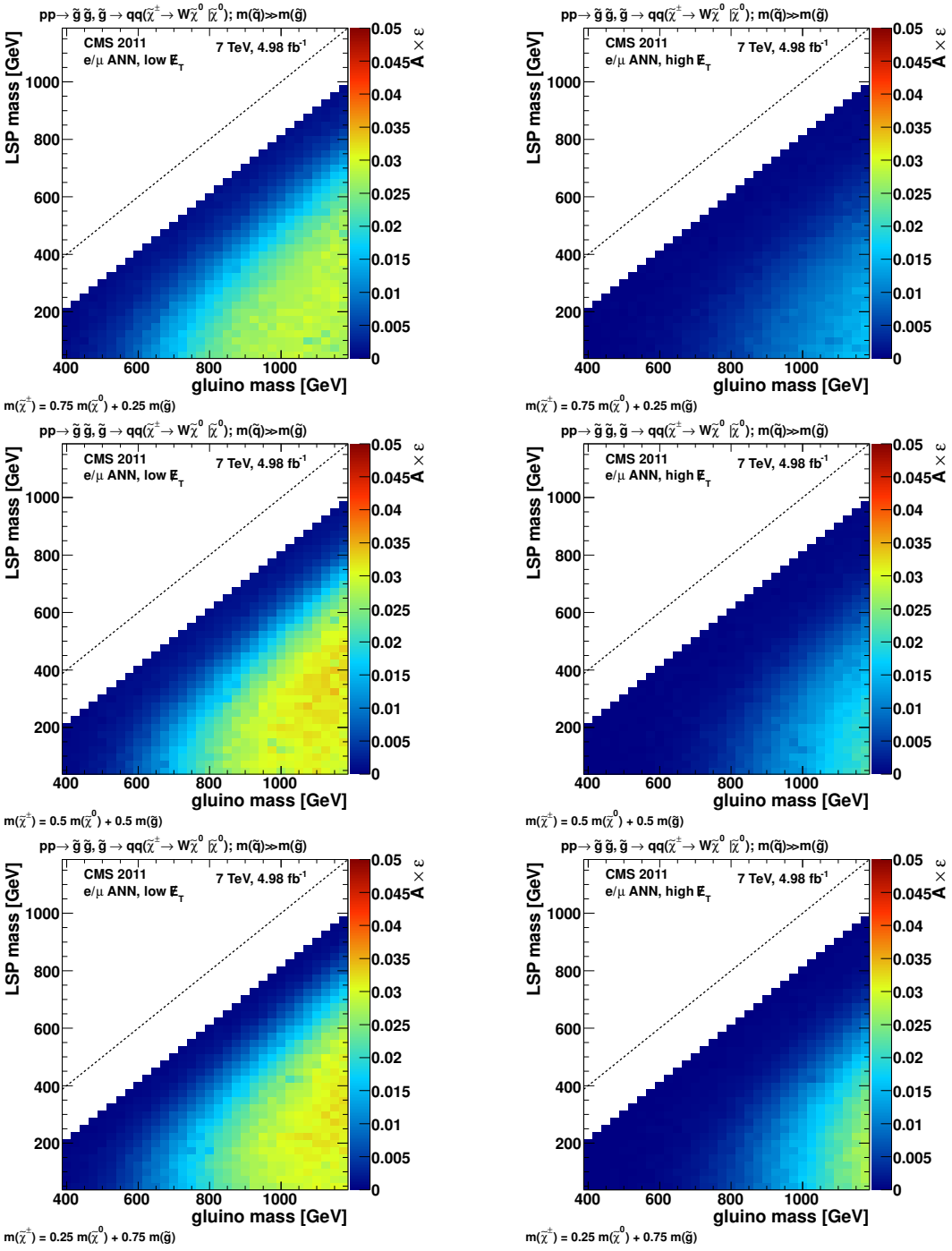

Figure 7.4: Signal efficiencies for the T3w simplified model, for the low-$\not\!\!E_{\mathrm{T}}$ (left) and high-$\not\!\!E_{\mathrm{T}}$ (right) signal regions.

- Using this observed limit as the cross section, we provide the limit-setting code with the signal yield after correcting it for signal contamination using the same method as used for the CMSSM plane.
- The limit-setting code returns the excluded signal strength parameter i.e. a scale factor with which we multiply the initial observed limit to get the final observed limit.

The effect of signal contamination is to slightly worsen the limit, but for almost the entire plane, the impact on the observed limit is under a factor of two. The limit plots, with signal contamination included, can be seen in Fig 7.5.

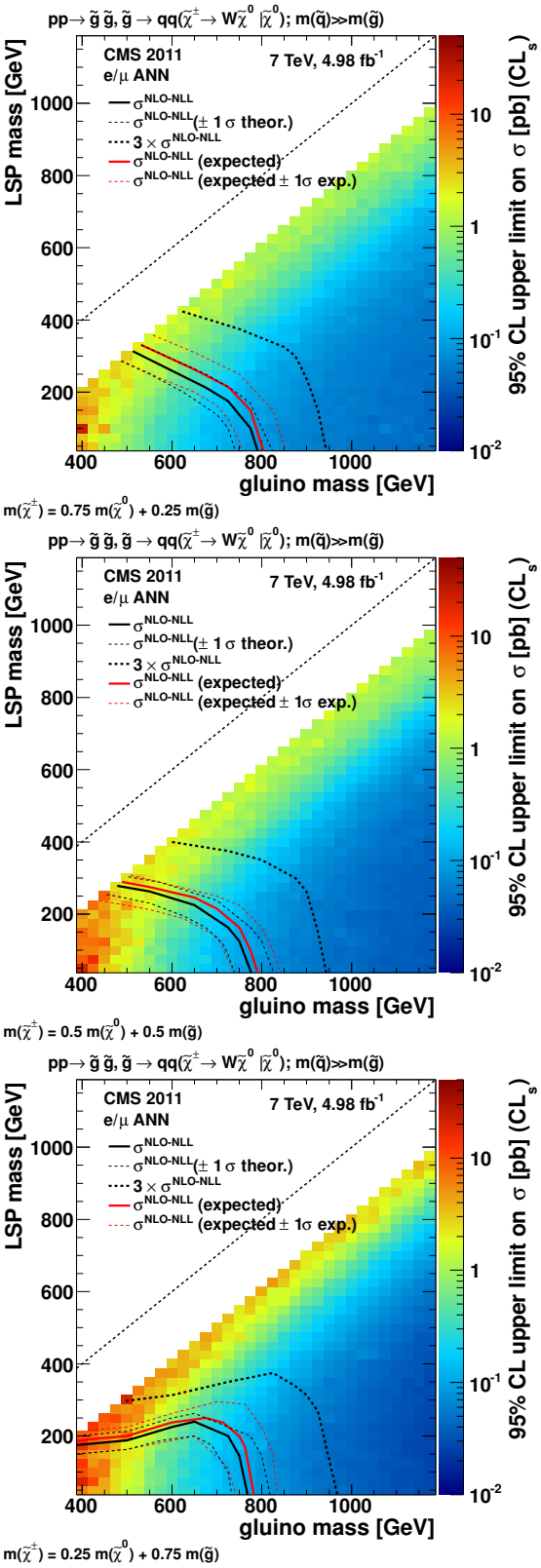

Figure 7.5: Observed limit (with signal contamination included) for the T3w simplified model, as made by the SMS group.

CHAPTER 8

CONCLUSION

The nature and origin of the universe is a topic that has always fascinated mankind. While the 20th century has seen major advances in particle physics that have gone a long way to illuminate us in this regard, there are many questions that remain unanswered. The chief reason for this has been technological limitations: to probe conditions that are similar to the early universe, particles need to be accelerated to very high energies. The LHC has been designed to address this shortcoming, and help us understand the nature of new physics beyond the SM. The CMS detector is a great achievement in detector technology, and enables us to study the products of these high energy collisions occuring in very high luminosity environments with great accuracy and precision. We have seen why the SM, despite being an extremely rigorous theoretical framework that withstands the scrutiny experimental particle physics has subjected it to, is unable to be a complete description of the observable universe. We have explored why SUSY is an intellectually promising theory that might provide answers to some of the questions that are currently unresolved.

Using 4.98 fb^{-1} of proton-proton collision data at $\sqrt{s} = 7$ TeV, we have searched for SUSY events with the experimental signature of a single lepton, at least three jets, and large $\not{E}_{\text{T}}$. The overall shapes of kinematic variables agree between data and simulation, indicating that our sample consists primarily of $t\bar{t}$ and W+jets events. We combine four kinematic variables (viz. n_{jets}, H_{T}, $\Delta\phi(\text{j}_1,\text{j}_2)$ and M_{T}) using an artificial neural network trained on simulated SM and SUSY events, which allows us to strongly suppress SM backgrounds. Our signal regions are defined by large values of z_{ANN} and $\not{E}_{\text{T}}$. The remaining background in these signal regions is estimated using a data-driven technique based on the lack of correlation between z_{ANN} and $\not{E}_{\text{T}}$. We predict the $\not{E}_{\text{T}}$

spectrum of events with high z_{ANN} using the $\not\!\!E_{\mathrm{T}}$ spectrum of events with low z_{ANN}, which is largely unaffected by the presence of possible SUSY signal. Finding no excess of events above the predicted background in data, we interpret our results in the framework of the CMSSM, reporting exclusion regions as a function of $m_{1/2}$ and m_0, for $\tan\beta = 10$. We also interpret our results using the T3w simplified model, and present cross section upper limits in the gluino-neutralino mass plane, after fixing the mass of the chargino. The results are similar in sensitivity to other CMS analyses looking at the same final state signature.

CHAPTER 9

BIBLIOGRAPHY

[1] D. Griffiths, "Introduction to Elementary Particles, 2nd Ed.". Wiley, 2008.

[2] ATLAS Collaboration, "Observation of a new particle in the search for the Standard Model Higgs boson with the ATLAS detector at the LHC", (2012). arXiv:1207.7214v1.

[3] CMS Collaboration, "Observation of a new boson at a mass of 125 GeV with the CMS experiment at the LHC", (2012). arXiv:1207.7235v1.

[4] M. Peskin and D. Schroeder, "An Introduction To Quantum Field Theory". Westview Press, 1995.

[5] F. Halzen and A. Martin, "Quarks and Leptons: An Introductory Course in Modern Particle Physics". Wiley, 1984.

[6] http://en.wikipedia.org/wiki/File:Standard_Model_of_Elementary_Particles.svg.

[7] http://en.wikipedia.org/wiki/File:Elementary_particle_interactions.svg.

[8] http://lepewwg.web.cern.ch/LEPEWWG/plots/winter2012/.

[9] J. Martin, "A Supersymmetry Primer", (1997). arXiv:9709356.

[10] CMS Collaboration, "CMS technical design report, volume II: Physics performance", *J. Phys.G* **34** (2007) 995, doi:10.1088/0954-3899/34/6/S01.

[11] CMS Collaboration, "Interpretation of Searches for Supersymmetry with Simplified Models", *CMS Physics Analysis Summary* **CMS-PAS-SUS-11-016** (2011).

[12] CMS Collaboration, "The CMS experiment at the CERN LHC", *JINST* **0803** (2008) S08004, doi:10.1088/1748-0221/3/08/S08004.

[13] L. Rossi, "Superconductivity: its role, its success and its setbacks in the Large Hadron Collider of CERN", *Supercond. Sci. Technol.* **23** (2010) 034001, doi:10.1088/0953-2048/23/3/034001.

[14] CMS Collaboration, "Electron Reconstruction and Identification at $\sqrt{s} = 7$ TeV", *CMS Physics Analysis Summary* **CMS-PAS-EGM-10-004** (2010).

[15] E. Meschi et al., "Electron Reconstruction in the CMS Electromagnetic Calorimeter", *CMS Analysis Note* **2001/034** (2001).

[16] CMS Collaboration, "Performance of muon identification in pp collisions at $\sqrt{s} = 7$ TeV", *CMS Physics Analysis Summary* **CMS-PAS-MUO-10-002** (2010).

[17] CMS Collaboration, "Jet Performance in pp collisions at $\sqrt{s} = 7$ TeV", *CMS Physics Analysis Summary* **CMS-PAS-JME-10-003** (2010).

[18] CMS Collaboration, "Jet Energy Corrections determination at $\sqrt{s} = 7$ TeV", *CMS Physics Analysis Summary* **CMS-PAS-JME-10-010** (2010).

[19] CMS Collaboration, "Particle-Flow Event Reconstruction in CMS and Performance for Jets, Taus, and ETmiss", *CMS Physics Analysis Summary* **CMS-PAS-PFT-09-001** (2009).

[20] CMS Collaboration, "Commissioning of the Particle-Flow Reconstruction in Minimum-Bias and Jet Events from pp Collisions at 7 TeV", *CMS Physics Analysis Summary* **CMS-PAS-PFT-10-002** (2010).

[21] CMS Collaboration, "Track reconstruction in the CMS Tracker", *CMS Physics Analysis Summary* **CMS-PAS-TRK-09-001** (2009).

[22] M. Cacciari, G. Salam, and G. Soyez, "The anti-k_T jet clustering algorithm", *JHEP* **0804** (2008) 063, doi:10.1088/1126-6708/2008/04/063.

[23] M. Cacciari and G. Salam, "Pileup subtraction using jet areas", *Phys. Lett. B* **659** (2008) 119, doi:10.1016/j.physletb.2007.09.077.

[24] http://www.hep.phy.cam.ac.uk/~wjs/plots/crosssections2012_v5.pdf.

[25] CMS Collaboration, "Charged particle multiplicities in pp interactions at $\sqrt{s}$ = 0.9, 2.36, and 7.0 TeV", *CMS Physics Analysis Summary* **CMS-PAS-QCD-10-004** (2010).

[26] CMS Collaboration, "Measurement of the Inclusive Jet Cross Section in pp Collisions at 7 TeV", *CMS Physics Analysis Summary* **CMS-PAS-QCD-10-011** (2010).

[27] CMS Collaboration, "Measurement of the 3-jet to 2-jet Cross Section Ratio in pp Collisions at $\sqrt{s}$ = 7 TeV", *CMS Physics Analysis Summary* **CMS-PAS-QCD-10-012** (2010).

[28] CMS Collaboration, "Rates of Jets Produced in Association with W and Z Bosons in pp Collisions at $\sqrt{s}$ = 7 TeV", *CMS Physics Analysis Summary* **CMS-PAS-EWK-10-012** (2010).

[29] CDF, D0 Collaborations, "Combination of the top-quark mass measurements from the Tevatron collider", (2012). arXiv:1207.1069v2.

[30] GEANT4 Collaboration, "GEANT4: A simulation toolkit", *Nucl. Instrum. Meth.* **506** (2003) 250, doi:10.1016/S0168-9002(03)01368-8.

[31] T. Sjöstrand, S. Mrenna, and P. Skands, "PYTHIA 6.4 Physics and Manual;v6.420,tune D6T", *JHEP* **05** (2006) 026, doi:10.1088/1126-6708/2006/05/026.

[32] J. Alwall et al., "MadGraph/MadEvent v4: The New Web Generation", *JHEP* **09** (2007) 028, doi:10.1088/1126-6708/2007/09/028.

[33] S. Frixione, P. Nason, and C. Oleari, "Matching NLO QCD computations with parton shower simulations: the POWHEG method", *JHEP* **11** (2007) 070, doi:10.1088/1126-6708/2007/11/070.

[34] J. Feltesse, "Introduction to Parton Distribution Functions", *Scholarpedia* **5** (2010) 10160, doi:10.4249/scholarpedia.10160.

[35] P. Nadolsky et al., "Implications of CTEQ global analysis for collider observables", *Phys. Rev. D* **78** (2008) 013004, doi:10.1103/PhysRevD.78.013004.

[36] A. Martin et al., "Parton distributions for the LHC", *Eur. Phys. J. C* **63** (2009) 189, doi:10.1140/epjc/s10052-009-1072-5.

[37] CMS Collaboration, "Search for supersymmetry in pp collisions at $\sqrt{s}$ = 7 TeV in events with a single lepton, jets, and missing transverse momentum", *CMS Physics Analysis Summary* **CMS-PAS-SUS-12-010** (2012).

[38] A. Hoecker et al., "TMVA 4 Toolkit for Multivariate Data Analysis with ROOT", (2009). arXiv:physics/0703039.

[39] T. Danielson et al., "Search for supersymmetry in proton-proton collisions at $\sqrt{s}$ = 7 TeV in events with a single lepton,jets, and missing transverse momentum", *CMS Analysis Note* **2011/410** (2011).

[40] CMS Collaboration, "Measurements of Inclusive W and Z Cross Sections in pp Collisions at $\sqrt{s}$ = 7 TeV", *JHEP* **1101** (2011) 080, doi:10.1007/JHEP01(2011)080.

[41] G. Dissertori et al., "Angular properties of Z + Jets events", *CMS Analysis Note* **2012/080** (2012).

[42] CMS Collaboration, "Absolute Calibration of the Luminosity Measurement at CMS: Winter2012 Update", *CMS Physics Analysis Summary* **CMS-PAS-SMP-12-008** (2012).

[43] M. Krämer et al., "Supersymmetry production cross sections in pp collisions at $\sqrt{s}$ = 7 TeV", (2012). arXiv:1206.2892v1.

[44] A. Read, "Presentation of search results: the CL_s technique", *J. Phys. G: Nucl. Part. Phys.* **28** (2002) 2693, doi:10.1088/0954-3899/28/10/313.

APPENDIX A

APPENDIX

A.1 Performance of ANN on other LM points

Fig. A.1 shows the z_{ANN} distribution for LM points other than LM0 and LM6 (which have already been shown previously). As we can see, even though the ANN has been trained on LM0 as signal, it is able to separate other LM points from SM quite well. This is a consequence of us choosing input variables that are not overly model-dependent.

Additionally, we also do a study to check if training the ANN using other LM points, specifically LM6 and LM9, can result in better signal yields than when training using LM0. In all training cases, we use the same neural net architecture (one hidden layer with 10N nodes, and tanh activation function), and the same four input variables (n_{jets}, H_{T}, $\Delta\phi(\mathrm{j}_1,\mathrm{j}_2)$ and M_{T}). To compare signal yields, we make a $\not\!\!E_{\mathrm{T}}$ cut of 350 GeV, and then scan z_{ANN} (in steps of 0.01) to select the loosest cut value that results in a SM background of 10 or fewer events. For the ANN trained with LM0, the remaining background is 9.3 events, and for LM6 and LM9, the corresponding numbers are 10.0 and 9.6 events, respectively. Fig. A.2 shows the signal yields for the three ANNs trained with LM0, LM6 and LM9 as the signal sample. All LM points have a better signal yield for the same background if the analysis uses an ANN trained with LM0 rather than LM6 or LM9. The sole exception is LM7, which has 5% higher yield when an ANN trained on LM9 is used. As we can see, LM0 gives the best performance across the board. We have also done this study with a $\not\!\!E_{\mathrm{T}}$ cut of 500 GeV, and picking the loosest ANN cut that retains less than 2 events of SM MC background. Even with the elevated $\not\!\!E_{\mathrm{T}}$ cut, there is no benefit to training with LM6 or LM9 instead of LM0.

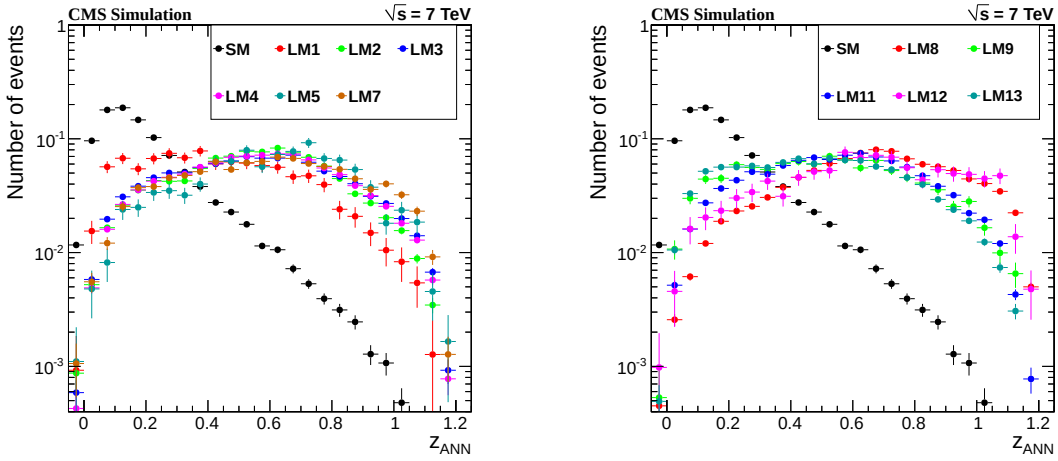

Figure A.1: Comparison of z_{ANN} for SM and various LM points. All histograms are normalized to unit area.

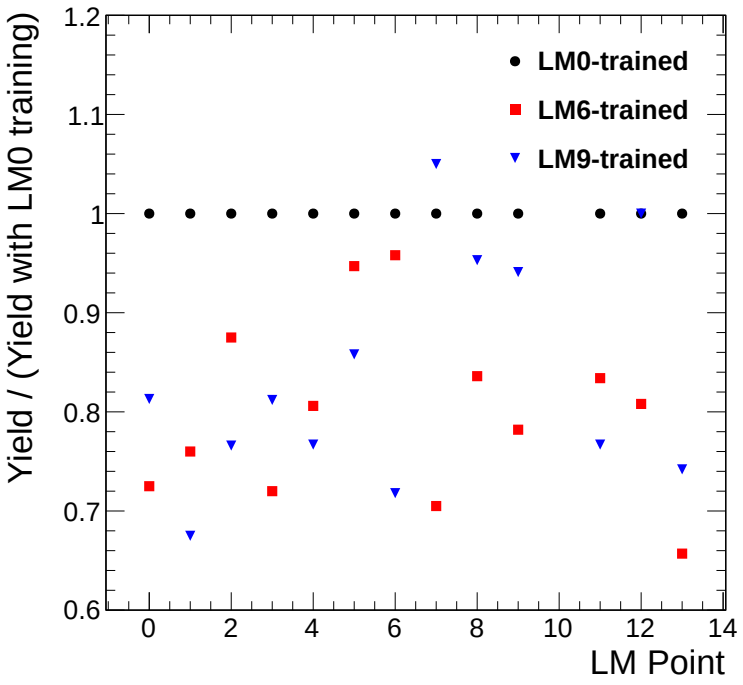

Figure A.2: Signal yield as a function of LM point for neural networks trained with LM0 (circles), LM6 (squares) and LM9 (triangles). The signal yields are normalized to that obtained for the same sample using the LM0-trained ANN.

A.2 List of variables considered for use in the ANN

- Number of jets (n_{jets})
- p_{T} of three leading jets
- η of two leading jets
- $H_{\text{T}} \equiv$ scalar sum of p_{T} of all jets passing cuts
- HT2: same as H_{T}, with leading jet removed
- Lepton p_{T}
- $M_{\text{eff}} \equiv H_{\text{T}} + \not{E}_{\text{T}}$ + Lepton p_{T}
- Lepton p_{T}/ H_{T}
- Lepton p_{T}/ HT2
- Lepton p_{T}/ M_{eff}
- M_{T}: transverse mass using lepton p_{T} and $\not{E}_{\text{T}}$
- $\not{E}_{\text{T}}$/ $\sqrt{H_{\text{T}}}$
- $\not{E}_{\text{T}}$/ M_{eff}
- Minimum ΔR between lepton and all jets passing cuts
- Invariant mass of lepton and nearest jet
- $\Delta\phi$ between two leading jets ($\Delta\phi(j_1,j_2)$)
- $\Delta\phi$ between two jets with highest value of the TCHE b-tagging discriminator
- Minimum $\Delta\phi$ between $\not{E}_{\text{T}}$ and all jets passing cuts
- $\Delta\phi$ between lepton and $\not{E}_{\text{T}}$

Table A.1: Effect of adding additional variables to the ANN on SUSY yields.

Added variable	SM bkgd	LM6 yield	LM0 yield
Original	9.3	45.6	172
Leading jet p_{T}	10.0	41.0	173
2nd Leading jet p_{T}	9.9	43.5	188
3rd Leading jet p_{T}	9.7	46.0	178
Leading jet η	9.3	46.0	183
2nd Leading jet η	10.0	47.6	190
Minimum ΔR between lepton and jets	9.9	49.7	202
Invariant mass of lepton and nearest jet	9.1	46.7	194

We do a study to check if adding any variable to the list of input variables actually used in the ANN can significantly improve the signal efficiency. We add one variable at a time to the four variable list, train the ANN, and check to see what the new signal yield for LM6 is. In all training cases, we use the same neural net architecture (one hidden layer with 10N nodes, and tanh activation function). To compare signal yields, we make a $\not\!\!E_{\mathrm{T}}$ cut of 350 GeV, and then scan z_{ANN} (in steps of 0.01) to select the loosest cut value that results in a SM background of 10 or fewer events. For this study, we leave out variables that are likely to introduce a correlation between z_{ANN} and $\not\!\!E_{\mathrm{T}}$. This rules out lepton p_{T}, and all ratios that involve lepton p_{T} or $\not\!\!E_{\mathrm{T}}$. For expediency, we also leave out the other $\Delta\phi$ variables, since TMVA ranks them as having less separation power than $\Delta\phi(\mathrm{j}_1,\mathrm{j}_2)$, which is itself a weak variable. This leaves us with seven candidate variables, and Table A.1 shows the SM background and the LM6 yield when each of these variables is allowed to be in the ANN. The table also shows LM0 yields for completeness. As we can see, the biggest change for LM6 is about 10%, seen when adding minimum ΔR between lepton and jets. This modest increase in signal yield does not justify the added complexity.

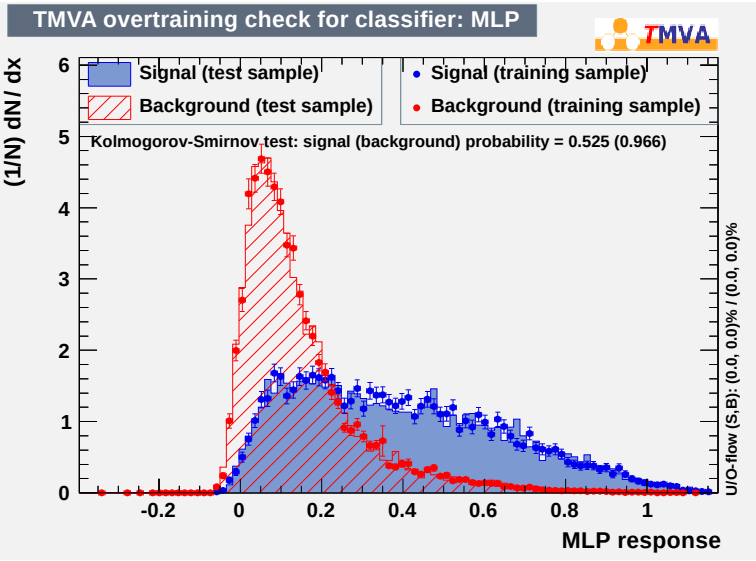

Figure A.3: Comparison of z_{ANN} using training and testing MC samples.

A.3 Over-training check for ANN

To train our ANN, we use 600 epochs, the number recommended by TMVA. Nonetheless, we need make sure that the ANN is not over-trained i.e. the ANN has learned only to recognize actual event features, rather than statistical fluctuations present in the finite-sized training sample. TMVA provides us with a simple tool to perform this check. We need to compare z_{ANN} for the training background sample with the testing background sample, and ensure that the distributions match closely with each other. The same test needs to also be done for the signal sample. This is shown in Fig. A.3. As we can see, the training and testing samples have very similar z_{ANN} distributions, and over-training is therefore not a concern.

We also want to make sure that the training process has converged i.e. the cost function for the training sample is not changing significantly as a function of the epoch. This can be seen in Fig. A.4 (left), where we see that convergence is reached after about 400 epochs. Finally, we check to see what conditions need to be imposed to see over-

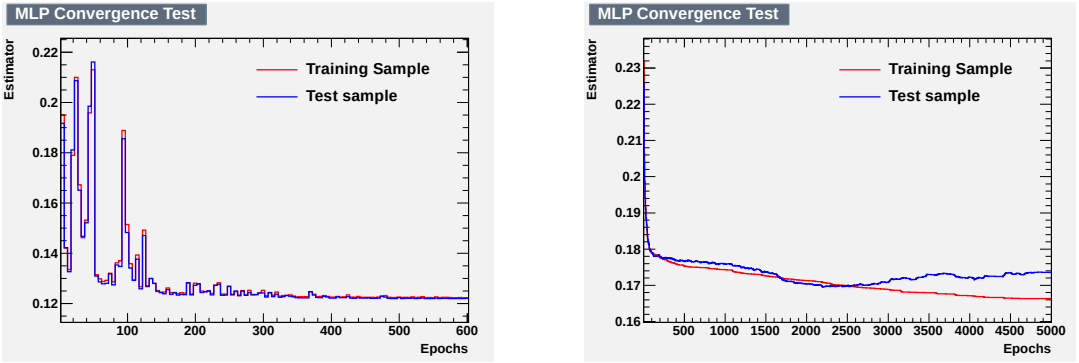

Figure A.4: Left: Convergence test for ANN. Right: Forcing over-training by using training trees with reduced statistics.

training. For this test, we use a training tree with only 10 k events (5 k background and 5 k signal). As a comparison, the actual number of events used for training and testing are about 75 k (background) and 20 k (signal). We also use the BFGS training algorithm for this test, as opposed to the BP training algorithm which is used in the analysis. This is done because the BFGS algorithm has smoother variations of the cost function. In Fig. A.4 (right), we see that with these special conditions imposed, over-training can be seen after about 2500 epochs (the cost functions of the training and testing samples begin to diverge).